

Article

A Stochastic Modelling Framework for Single Cell Migration: Coupling Contractility and Focal Adhesions

Aydar Uatay [†] 

Felix-Klein-Zentrum für Mathematik, Technische Universität Kaiserslautern, Paul-Ehrlich-Str. 31, 67663 Kaiserslautern, Germany; a.uatay@sheffield.ac.uk

[†] Current address: Department of Biomedical Sciences, The University of Sheffield, Western Bank, Sheffield S10 2TN, UK

Received: 15 June 2020; Accepted: 9 August 2020; Published: 12 August 2020



Abstract: The interaction of the actin cytoskeleton with cell–substrate adhesions is necessary for cell migration. While the trajectories of motile cells have a stochastic character, investigations of cell motility mechanisms rarely elaborate on the origins of the observed randomness. Here, guided by a few fundamental attributes of cell motility, I construct a minimal stochastic cell migration model from ground-up. The resulting model couples a deterministic actomyosin contractility mechanism with stochastic cell–substrate adhesion kinetics, and yields a well-defined piecewise deterministic process. Numerical simulations reproduce several experimentally observed results, including anomalous diffusion, tactic migration and contact guidance. This work provides a basis for the development of cell–cell collision and population migration models.

Keywords: cell motility; focal adhesions; piecewise deterministic process; superdiffusion; tactic migration; cell contractility

1. Introduction

Cell migration is essential for embryogenesis, wound healing, immune surveillance and progression of diseases, such as cancer metastasis. During embryogenesis, coordinated collective migration to particular sites is essential to the development of an organism. Tissue repair and immune response rely on directed movement of cells following external cues, which are produced after the tissue layer is damaged and infected with pathogens. Likewise, cancer cells migrate away from the tumour into surrounding tissue and distant organs to form metastases, which is the leading cause of death among cancer patients.

Cell motility is a cyclical process, involving morphological changes of the cell body and adhesive contacts with the underlying substrate [1]. The cycle can be divided into three steps: protrusion of the leading edge, assembly of adhesions to the substrate at the front and disassembly in the rear and contraction of the cell body, thereby producing locomotion [2]. This type of crawling movement requires transmission of contractile forces, generated within the cell cytoskeleton, through substrate adhesions. Such mechanical interactions between various cellular structures is attained by integrating numerous signalling molecules, the most prominent of which are Rho GTPases [3,4]. While there are other modes of motility relying on, for example, flagellar activity (e.g., spermatozoa or *E. coli*) or rolling in the bloodstream (e.g., leukocytes), here the focus is on the crawling type of movement.

Due to cell motility being a highly complex and not fully elucidated process, mathematical modelling of the corresponding phenomena is a challenging task. Numerous approaches have

been developed, each being able to capture a certain aspect of the process (see [5,6] for extensive reviews on whole cell motility models and [7] for a review on modelling of its critical components). For example, free boundary and phase-field models of steadily migrating cells in [8,9] (and its extension in [10]), [11–13] are able to reproduce cell morphology as a result of mechanical and biochemical interactions. Models of cell migration in [14,15] explored emergence of various motility modes due to mechanical coupling of intracellular components and the substrate. In their hybrid motility model, Marée et al. [16,17] explored the mechanochemical interaction in detail by considering the Rho GTPase signaling circuit. A common feature of these continuum models is that they are not able to reproduce experimentally observed random paths of migrating cells. Stochastic motility models of eukaryotic cells have been proposed, for example, in [18–22]. Their stochasticity is driven by a Gaussian process, although there is evidence that the paths of the migrating cells follow a non-Gaussian process [23–25]. Another way to include randomness is based on velocity jump process, as proposed by [26] in the context of cell motility. Extending the model and including cell–substrate interactions, population migration models have been proposed in [27,28]. Here, however, our focus is solely on single cell migration.

In this paper and the follow-up works, I strike a middle ground. By proposing a minimal cell representation including a few cellular structures essential for cell motility, I aim at reproducing stochastic migratory paths in various experimental settings. In our model, stochasticity arises as a result of mechanochemical coupling between the cell cytoskeleton and the substrate through adhesive contacts. Specifically, the random events under consideration are the (de)adhesion events of the cell migration cycle, whereas deterministic locomotion and contraction occur between arrival of the events. Here, I do not make any prior assumptions about the distributions that the events and their arrival times follow. Rather, I consider, in detail, the major determinants of adhesion dynamics and derive the complete stochastic description. This is in contrast to most mathematically well-posed models on stochastic cell migration, where it is assumed that the motion follows a Gaussian process. Thereby, the construction of our cell motility model will result in a piecewise deterministic Markov process (PDMP) [29,30]. Our simulations reproduce experimental observations, such as superdiffusive scaling of the squared displacement [23,24,31], biased migration in the presence of an external cue, contact guidance [32] and directed movement due to asymmetric contractility (and in the absence of guidance cues) [33,34]. Thus, our approach illustrates how detailed treatment of adhesion cluster dynamics can translate into stochastic cell motility description in a mathematically consistent manner.

Due to the minimal character of the model and our bottom-up approach, this work serves as a basis for modelling cell–cell collisions in [35] and population migration (Chapter 7 in [36]). In particular, the latter, mesoscopic scale model can be derived from our microscopic model presented here (Chapter 7 in [36]). The derived model describes population migration via a (probability) density function, and captures the aforementioned intracellular activity. Therefore, the work presented here falls, in part, into a broader framework called Kinetic Theory of Active Particles (KTAP) [37]. Several multiscale approaches utilized this framework to model chemo-, haptotaxis and movement along fibre tracts [27,28,38]. Although in these works subcell dynamics has been considered via a description of receptor binding, interaction of subcellular structures, essential for generation of cell migration, has been neglected. Here, I describe such interactions in detail and show that it can be wrapped into PDMP theory, which can then be used to derive kinetic description more rigorously. As the derivation is out of scope, I leave its demonstration for the forthcoming work.

This article is organized as follows. In Section 2, I briefly describe the cell motility cycle and the relevant agents. I then introduce the minimal cell representation and describe the deterministic cell motion between the cycle steps. In Section 3, I construct a stochastic model of adhesion events, which signify transitions of cycle stages. In Section 4 I combine the deterministic and stochastic components of the migration cycle to obtain a well-defined piecewise deterministic Markov process. At the end of this section, I briefly remark how on relation of the process to the KTAP. In Section 5, I specify the

kinetics of adhesion events. Numerical simulations are performed in Section 6. A discussion of the results and future outlook are presented in Section 7.

2. The Cell Motility Model

The cell migration cycle begins with protrusion of the leading edge as a result of actin polymerization (Figure 1a). The polymerization process in lamellipodia is mediated by the Arp2/3 complex, which acts downstream of signalling pathways responsible for cell polarization [4]. Next, the protrusions are stabilized due to formation of focal adhesions (FAs) in the lamellae (regions behind the lamellipodia), which link the actin cytoskeleton to the extracellular matrix (ECM). An FA is a multiprotein integrin-based adhesion cluster, which matures in a Rho GTPase dependent manner [3]. Furthermore, FA maturation depends on the applied tension and occurs concomitantly with actomyosin bundle formation [39]. These bundles, called stress fibres (SFs), generate contractile forces due to non-muscle myosin II motors. Due to increased tension at cell rear, FAs rupture. Finally, deadhesion leads to cell body translocation due to cytoskeletal contraction.

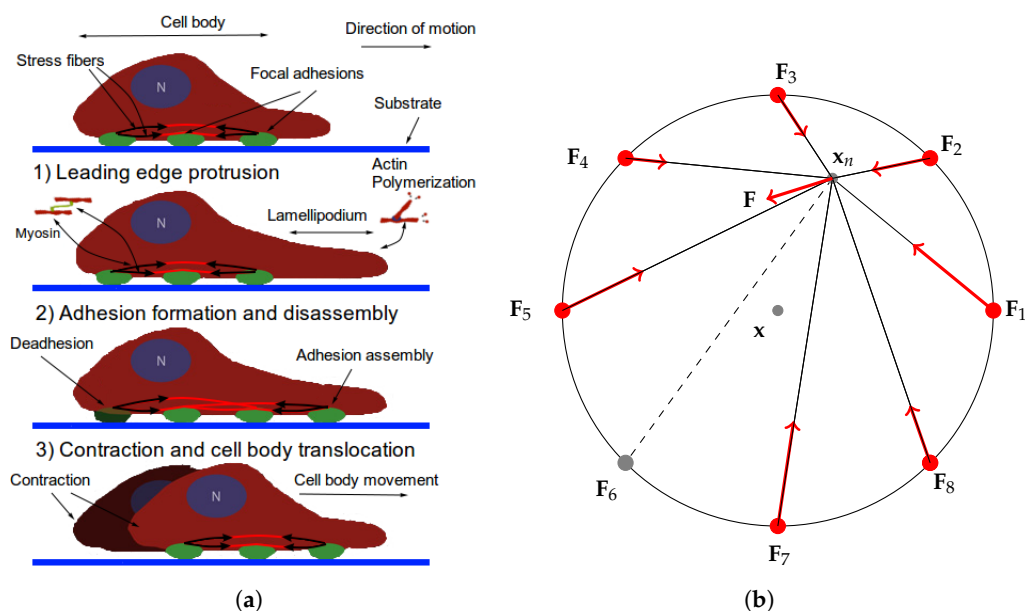


Figure 1. (a) Schematic diagram of the cell migration cycle and the implicated cellular structures. Actin polymerization at the front pushes the membrane allowing protrusions to form. Then, adhesions assemble at the front and disassemble at the rear. Finally, deadhesion and cell contraction produce locomotion, pulling the body forward. The black arrows overlaying the stress fibres show the inwardly directed contractile forces. (b) Schematic representation of a cell with $M = 8$ focal adhesions. Solid black lines represent stress fibres while red bullets represent focal adhesions. Red arrows indicate the direction and magnitude of applied traction force F_i , $i = 1, \dots, 8$. The dashed line and the corresponding grey circle represent an absent stress fibre and unbound focal adhesion, respectively. The central red arrow indicates the net force F on x_n and x is the cell centroid.

In order to construct the mathematical model, I make the following assumptions. First, FA unbinding leads to reconfiguration of SFs and the cell movement, whereas assembly of new FAs leads to only to the former. Second, FA events need not occur in the order described above. Several adhesions might be assembled (disassembled) before deadhesion (adhesion) occurs. Note also that while the contractile machinery is important, the dynamic instability of adhesions is what drives the migratory process, for stable FAs prevent retraction. Thus, I consider only interactions of SFs and FAs. Moreover, I do not consider the actin polymerization process and simplify the migration cycle to two steps: after FA assembly occurs, a cell does not move, but reconfigures SFs; after disassembly, a cell

does both. Neglecting the polymerization process and the reduction to binding/unbinding events can be justified by the fact that one of the major consequences of the leading edge protrusions is promotion of FA assembly. As a result that the repolarization of migrating cells occurs frequently as an outcome of intricate biochemical activity, then, in order to keep the model tractable, I do not explicitly model cell polarity. Instead, (de)adhesion frequency is indicative of (rear)front. By neglecting the polymerization process, dynamic alterations to actin cytoskeleton (i.e., cytoskeletal remodelling) is simplified to SF reconfiguration.

2.1. The Cell Representation

Consider the situation in Figure 1b. The disk represents a cell. Let the radius be R_{cell} and let the position of the centre at time t be $\mathbf{x}(t) \in \mathbb{R}^2$. Suppose there are M equally spaced adhesion sites $\mathbf{x}_i(t) \in R_{cell}\mathbb{S}^1$, $i = 1, \dots, M$ on a cell circumference with constant relative distance (see Remark 1 in Section 2.3). Let $\mathbf{Y}(t) \in \{0, 1\}^M$ be a vector of focal adhesion states at time t , i.e., $Y_i(t) = 0, 1$ correspond to unbound and bound FA at node i , respectively.

Since the traction stresses are oriented inward, transmitted to ECM by FAs and generated by contractile SFs, then the FAs on the circumference must be one of the ends of SFs. Suppose the other end of all SFs at time t is at the position $\mathbf{x}_n(t) \in \Omega_{cell} := \{(x, y) \in \mathbb{R}^2 \mid x^2 + y^2 \leq R_{cell}^2\}$ (in a cell's reference frame with origin at \mathbf{x}), i.e., all SFs are connected at \mathbf{x}_n . Since stress fibres behave like Hookean springs on extension, but readily buckle under compression (see Figure 2b for illustration) [40], then, inspired by Guthardt Torres et al. [41], the force \mathbf{F}_i at focal adhesion i is given by:

$$\mathbf{F}_i = \begin{cases} \left(T_i + EA \frac{L_i - L_0}{L_0}\right) \mathbf{e}_i, & L_0 < L_i \\ T_i \mathbf{e}_i, & L_c \leq L_i \leq L_0 \\ \frac{L_i - L_c + \delta}{\delta} T_i \mathbf{e}_i, & L_c - \delta \leq L_i < L_c \\ 0 & L_i < L_c - \delta, \end{cases} \quad (1)$$

where T_i is the magnitude of the contractile force due to myosin motors, EA is the one-dimensional Young's modulus, L_0 and L_c are, respectively, rest and critical lengths, $L_i = \|\mathbf{x}_n - \mathbf{x}_i\|$, $\mathbf{e}_i = \frac{\mathbf{x}_n - \mathbf{x}_i}{L_i}$ is the unit vector along the i^{th} SF and δ is a small positive constant. The first case in Equation (1) is due to the Hookean behaviour of SFs upon extension and myosin tension generation. Furthermore, stress fibre laser ablation experiments [42–44] revealed that the initial instantaneous response (elastic behaviour due to the SF length dependence in the first case) is followed by slower contraction due to myosin activity (force dependence on T_i) in the remaining portion of the fibre. Combined with stress fibre buckling, the second case in Equation (1) is obtained. Deguchi et al. [45] also found that SF contraction ceased after reaching a certain critical length. This implies that $F_i := \mathbf{F}_i \cdot \mathbf{e}_i$, the magnitude of \mathbf{F}_i along \mathbf{e}_i , is zero when $L_i < L_c - \delta$. For technical reasons, I assume F_i is piecewise continuous (see Figure 2a for profile of F_i)—hence the last cases in Equation (1). For simplicity, it is also assumed that myosin generated force T_i may vary between SFs, but is otherwise constant.

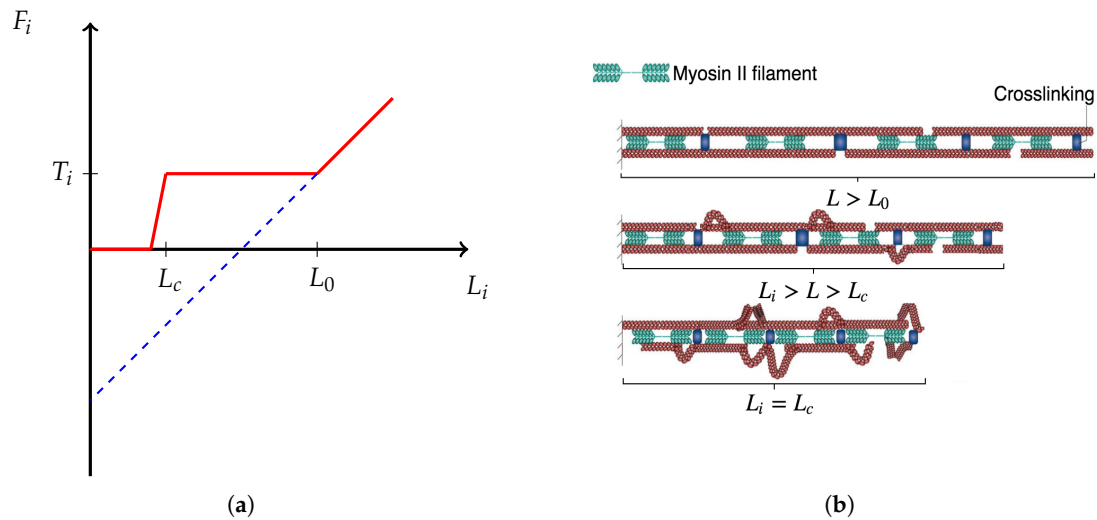


Figure 2. (a) Profile of F_i , the magnitude of \mathbf{F}_i along \mathbf{e}_i , in red. The blue dashed line corresponds to the profile of F_i if we were to treat the fibre as a Hookean spring with constant EA/L_0 . (b) Schematic representation of stress fibre contraction. As the fibre contracts below the rest length L_0 , buckling occurs. As myosin mediated contraction causes the fibre to contract below the rest length L_0 , buckling occurs due to lack of resistance to compression. Below the critical length L_c , the fibre ceases to contract due to vanishing interfilament distance. Modified from [40].

Note that since $\mathbf{x}_i(t) \in R_{cell}\mathbb{S}^1$ and FA sites are equally spaced, then in polar coordinates we have:

$$\mathbf{x}_i(t) = R_{cell}(\cos(\theta_i), \sin(\theta_i))^T, \quad \theta_i(t) := \theta_1(t) + (i-1)\frac{2\pi}{M},$$

and so $\mathbf{F}_i = \mathbf{F}_i(\mathbf{x}_n, \theta_1)$.

Since the force at \mathbf{x}_n due to i^{th} SF is $-\mathbf{F}_i$, then the net force at \mathbf{x}_n is

$$\mathbf{F}(\mathbf{x}_n, \theta_1, \mathbf{Y}) := - \sum_{i=1}^M Y_i \mathbf{F}_i(\mathbf{x}_n, \theta_1), \quad (2)$$

then, assuming negligible inertial effects (due to the viscous nature of cytoplasm) and constant \mathbf{Y} :

$$\beta_{cell} \dot{\mathbf{x}}_n = \mathbf{F}(\mathbf{x}_n, \theta_1, \mathbf{Y}), \quad (3)$$

where β_{cell} is the drag coefficient in the cytoplasm (see Appendix B for details).

The representation of a cell in such a way is justified for the following reasons:

- The traction stresses are largely applied on the cell periphery and their magnitude decays rapidly towards the centre [46,47]. Thus, the cell body SF ends are at or near mechanical equilibrium. Since contractile forces are generated by SFs, then a cell body SF end must be balanced by all other SFs (due to the equilibrium). Hence, it is reasonable to have a single connecting node of radial SFs which is either at mechanical equilibrium (for stationary cells) or tends to it.
- Paul et al. [48] demonstrated that application of force, originating from nuclear region, on FAs by star-like SF arrangement, results in cells acquiring morphologies typical for motile cells. Since the forces applied on FAs by SFs determine which one ruptures, then it also influences the motion of a cell (due to retraction). Since I am primarily interested in cell migration, it is justified to assume that this architecture represents a realistic situation. Furthermore, Oakes et al. [49] found that modelling SFs embedded in contractile networks, where only SFs actively contract, yields a behaviour mimicking their experimental results—the cytoskeletal flow was directed along the

stress fibres. In the same study, the authors concluded that it is appropriate to treat an SF as a 1D viscoelastic contractile element, which also justifies neglecting inertia in Equation (2).

- Since motile cells assume a wide variety of cell shapes and continuously remodel their actin cytoskeleton, one can view this representation as a cell shape normalization (it is implicitly assumed that a cell volume remains constant). That is, Figure 1b depicts a cell normalized to a circle. Möhl et al. [46] applied the shape normalization technique to a timelapse series data of migrating keratinocytes and demonstrated that this allows consistent analysis of FA dynamics, actin flow and traction forces. In view of their results, a particular cell traction force map and FA configuration normalized to a circle can be effectively captured by our representation.

Without loss of generality, I assume that our system starts to evolve at $t = 0$ and $\mathbf{x}_n(0) \in \Omega_{cell}$. Note that if $\mathbf{x}_n(0) \in \Omega_{cell}$, then $\mathbf{x}_n(t) \in \Omega_{cell}$ for $t > 0$, proved below. This result shows that our representation of the cell does not yield unphysical outcome, where stress fibres move outside of the cell. That is, provided initial conditions at $t = 0$ are physically well-defined (stress fibres are contained in the cell, i.e., $\mathbf{x}_n(0) \in \Omega_{cell}$), then they will remain so.

Proposition 1. Let $\mathbf{x}_n \in \partial\Omega_{cell}$, $\theta_1 \in [0, 2\pi)$, and $\mathbf{Y} \in \{0, 1\}^M$ be arbitrary. Let \mathbf{n} be outward unit normal at \mathbf{x}_n . Then $\mathbf{F}(\mathbf{x}_n, \theta_1, \mathbf{Y}) \cdot \mathbf{n} \leq 0$ with equality sign if and only if $\mathbf{F}(\mathbf{x}_n, \theta_1, \mathbf{Y}) = 0$.

Proof. The proposition above is obviously true, and it follows from the fact that

$$Y_i(-\mathbf{F}_i(\mathbf{x}_n, \theta_1)) \cdot \mathbf{n} = Y_i \|\mathbf{F}_i(\mathbf{x}_n, \theta_1)\| (-\mathbf{e}_i \cdot \mathbf{n}) = \frac{Y_i \|\mathbf{F}_i(\mathbf{x}_n, \theta_1)\|}{L_i} (\mathbf{x}_i - \mathbf{x}_n) \cdot \mathbf{n} \leq 0,$$

since $\mathbf{x}_i \cdot \mathbf{n} < 0$ and $\mathbf{x}_n \cdot \mathbf{n} > 0$. \square

Corollary 1. Let $\mathbf{x}_n(0) \in \Omega_{cell}$ be arbitrary and let $\theta_1(t)$ be given. Suppose $\mathbf{x}_n \in C^1([0, \infty))$ is a solution of Equation (3). Then, $\mathbf{x}_n(t) \in \Omega_{cell} \forall t > 0$ and $\forall \mathbf{Y}(t) \in \{0, 1\}^M$.

Proof. Due to Equation (3), it suffices to show that $\forall \mathbf{x}_n \in \partial\Omega_{cell}$ we have $\mathbf{F}(\mathbf{x}_n, \theta_1, \mathbf{Y}) \cdot \mathbf{n} \leq 0$, which follows from Proposition 1. \square

2.2. The Cell Migration Cycle

Recall that during the migration cycle, deadhesion leads to cell body translocation, while adhesion binding does not. In both cases actomyosin contractility leads to reconfiguration of the cytoskeleton. Here, I show how our cell representation can describe the reconfiguration and cell body motion following binding and unbinding events.

Without loss of generality assume that an event occurred at $t = 0$. Let $\tau > 0$ be the time of the next adhesion event, be it binding or unbinding. Let $\mathbf{Y}(0) \in \{0, 1\}^M$, $\mathbf{x}(0) \in \mathbb{R}^2$, and $\mathbf{x}_n(0) \in \Omega_{cell}$ be arbitrary. Then, $\mathbf{Y}(t) = \text{const.}$ for $t \in [0, \tau)$.

I assume $\theta_1(t = 0) = 0$. Since the FA sites are equally spaced, it is sufficient to consider $\theta_1(t)$ only.

2.2.1. Focal Adhesion Binding

Following an FA binding, I suppose that a cell becomes stationary (i.e., the cell centroid remains constant). However, a newly formed FA and the associated SF lead to cytoskeletal reshaping. Thus, we have the following system of ODEs for $t \in [0, \tau)$:

$$\begin{aligned} \dot{\mathbf{x}} &= 0 \\ \dot{\mathbf{x}}_n &= \beta_{cell}^{-1} \mathbf{F}(\mathbf{x}_n, \theta_1, \mathbf{Y}) \\ \dot{\theta}_1 &= 0. \end{aligned} \tag{4}$$

2.2.2. Focal Adhesion Unbinding

Following an unbinding event, cytoskeletal contraction leads to cell body movement. Due to the circular geometry, the contractile forces induce both rotational and translational motion.

Note that the bound focal adhesions are able to slide for short distances [46]. Oakes et al. [49] found that the cytoskeleton behaves like an elastic solid on timescales up to one hour. Provided the time τ between adhesion events is small enough, the following is justified.

The force \mathbf{F} along the radial vector $\hat{\mathbf{r}}(\mathbf{x}_n)$ is acting on the cell centre, thereby inducing translational motion (see Figure 3). On the other hand, the rotational motion is produced due to \mathbf{F} acting along the tangential vector $\hat{\boldsymbol{\phi}}(\mathbf{x}_n)$. The radial and tangential components of the force \mathbf{F} are given by:

$$\begin{aligned} F_r &:= \mathbf{F}(\mathbf{x}_n, \theta_1, \mathbf{Y}) \cdot \hat{\mathbf{r}}(\mathbf{x}_n) \\ F_\phi &:= \mathbf{F}(\mathbf{x}_n, \theta_1, \mathbf{Y}) \cdot \hat{\boldsymbol{\phi}}(\mathbf{x}_n), \end{aligned}$$

where $\mathbf{x}_n = (x_{n,1}, x_{n,2})$ and

$$\hat{\mathbf{r}}(\mathbf{x}_n) = \frac{\mathbf{x}_n}{\|\mathbf{x}_n\|}, \quad \hat{\boldsymbol{\phi}}(\mathbf{x}_n) = \left(-\frac{x_{n,2}}{\|\mathbf{x}_n\|}, \frac{x_{n,1}}{\|\mathbf{x}_n\|} \right)^T.$$

Note that the characteristic Reynolds number Re is given by

$$Re = \frac{\rho \cdot s \cdot L}{\nu} \sim 10^{-6} - 10^{-4},$$

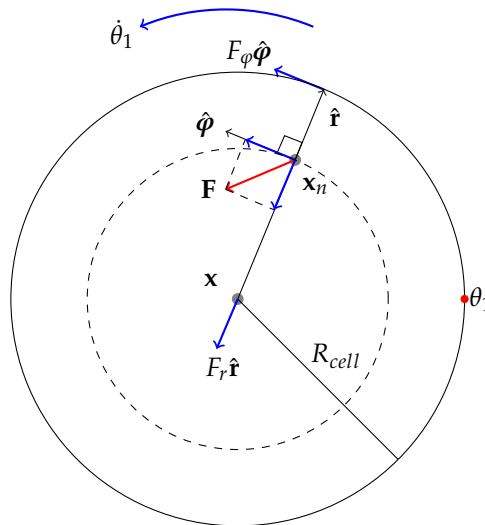


Figure 3. Force diagram showing transmission of internally generated contractile forces into translational and rotational motion. $\hat{\mathbf{r}}$ and $\hat{\boldsymbol{\phi}}$ are radial and angular unit vectors, respectively. $\dot{\theta}_1$ is the angular velocity, \mathbf{F} is a net contractile force, F_r and F_ϕ are radial and tangential components of \mathbf{F} , \mathbf{x} and R_{cell} are cell centre and radius, respectively.

Where I assumed the surrounding fluid is water (with corresponding values for density ρ and viscosity ν , and that characteristic cell speed s and size L are $0.1\text{--}1 \mu\text{m/s}$, $L = 10\text{--}50 \mu\text{m}$, respectively. Thus, neglecting inertia, we have:

$$\begin{aligned} \dot{\mathbf{x}} &= \beta_{ECM}^{-1} \mathbf{F}(\mathbf{x}_n, \theta_1, \mathbf{Y}) \cdot \hat{\mathbf{r}}(\mathbf{x}_n) \hat{\mathbf{r}}(\mathbf{x}_n) \\ \dot{\mathbf{x}}_n &= \beta_{cell}^{-1} \mathbf{F}(\mathbf{x}_n, \theta_1, \mathbf{Y}) \\ \dot{\theta}_1 &= \beta_{rot}^{-1} \|\mathbf{x}_n\| \mathbf{F}(\mathbf{x}_n, \theta_1, \mathbf{Y}) \cdot \hat{\boldsymbol{\phi}}(\mathbf{x}_n), \end{aligned} \quad (5)$$

where β_{ECM} and β_{rot} are, respectively, translational and rotational drag coefficients in the ECM (see Appendix A for derivations). Note that drag depends on the body shape, which changes frequently in migrating cells. However, for simplicity, the coefficients are assumed to be constant.

2.3. Specification of Kinematics

It is convenient to transform the system above into nondimensional form. In order to do so, I define the following scales, characterized by their respective constants:

- The spatial and cell length scales are defined by cell radii R_{cell} .
- The time scale is set by FA disassociation rate k_{off}^0 , since FA unbinding of leads to locomotion.
- The force scale is defined by the characteristic force F_b usually observed at an FA.

The values of these constants are given in Appendix B. Whence the new variables are defined:

$$\tilde{\mathbf{x}} := \frac{\mathbf{x}}{R_{cell}}, \quad \tilde{\mathbf{x}}_n := \frac{\mathbf{x}_n}{R_{cell}}, \quad \tilde{t} := k_{off}^0 t$$

and transform \mathbf{F}_i from Equation (1):

$$\tilde{\mathbf{F}}_i := \frac{\mathbf{F}_i}{F_b} = \begin{cases} \left(\tilde{T}_i + \widetilde{EA} \frac{\tilde{L}_i - \tilde{L}_0}{\tilde{L}_0} \right) \tilde{\mathbf{e}}_i, & \tilde{L}_0 < \tilde{L}_i \\ \tilde{T}_i \tilde{\mathbf{e}}_i, & \tilde{L}_c \leq \tilde{L}_i \leq \tilde{L}_0 \\ \frac{\tilde{L}_i - \tilde{L}_c + \tilde{\delta}}{\tilde{\delta}} \tilde{T}_i \tilde{\mathbf{e}}_i, & \tilde{L}_c - \tilde{\delta} \leq \tilde{L}_i < \tilde{L}_c \\ 0 & \tilde{L}_i < \tilde{L}_c - \tilde{\delta}, \end{cases} \quad (6)$$

where

$$\begin{aligned} \tilde{L}_i &= \frac{L_i}{R_{cell}}, & \tilde{L}_0 &= \frac{L_0}{R_{cell}}, & \tilde{L}_c &= \frac{L_0}{R_{cell}}, & \tilde{\delta} &= \frac{\delta}{R_{cell}}, \\ \tilde{T}_i &= \frac{T_i}{F_b}, & \widetilde{EA} &= \frac{EA}{F_b}, & \tilde{\mathbf{e}}_i &= \frac{\tilde{\mathbf{x}}_n - \tilde{\mathbf{x}}_i}{\tilde{L}_i}, & \tilde{\mathbf{x}}_i &= \frac{\mathbf{x}_i}{R_{cell}}. \end{aligned}$$

Note that we have $\tilde{\mathbf{x}}_n \in \tilde{\Omega}_{cell} := \{(x, y) \in \mathbb{R}^2 \mid x^2 + y^2 \leq 1\}$ and $\tilde{\mathbf{x}}_i \in \mathbb{S}^1$.

Let

$$\tilde{\mathbf{F}} := \mathbf{F}/F_b, \quad \tilde{\beta}_{cell} := \frac{k_{off}^0 R_{cell}}{F_b} \beta_{cell}, \quad \tilde{\beta}_{ECM} := \frac{k_{off}^0 R_{cell}}{F_b} \beta_{ECM}, \quad \tilde{\beta}_{rot} := \frac{k_{off}^0}{R_{cell} F_b} \beta_{rot}.$$

To complete the specification of cell kinematics between adhesion events, another discrete variable is introduced $\mu(t) \in \{0, 1\}$:

$$\mu = \begin{cases} 1, & \text{if the last event was unbinding} \\ 0, & \text{if the last event was binding.} \end{cases}$$

Then, plugging in Equations (4) and (5) the rescaled quantities and dropping tildes, it follows that the system evolves according to the following ODE system between the FA events:

$$\begin{aligned} \dot{\mathbf{x}} &= \mu \beta_{ECM}^{-1} \mathbf{F}(\mathbf{x}_n, \theta_1, \mathbf{Y}) \cdot \hat{\mathbf{r}}(\mathbf{x}_n) \hat{\mathbf{r}}(\mathbf{x}_n) \\ \dot{\mathbf{x}}_n &= \beta_{cell}^{-1} \mathbf{F}(\mathbf{x}_n, \theta_1, \mathbf{Y}) \\ \dot{\theta}_1 &= \mu \beta_{rot}^{-1} \|\mathbf{x}_n\| \mathbf{F}(\mathbf{x}_n, \theta_1, \mathbf{Y}) \cdot \hat{\boldsymbol{\phi}}(\mathbf{x}_n) \end{aligned} \quad (7)$$

Remark 1. Our assumption on constant relative distance between FA sites stems from two slightly weaker assumptions: (1) total number of adhesion sites (occupied and unoccupied) is constant; (2) there is a neighbourhood around each adhesion site, in which no other site is present, and the size of this neighbourhood is

the same (and constant) for each site. Figure 4 how it reflects on their peripheral motion. This assumption implies that in each line segment of size $2\pi/M$ (with $M = 8$) there is only one FA site present, which may correspond to bound (in red) or unbound FA (in gray). See also Appendix B on our discussion on the number of FA sites.

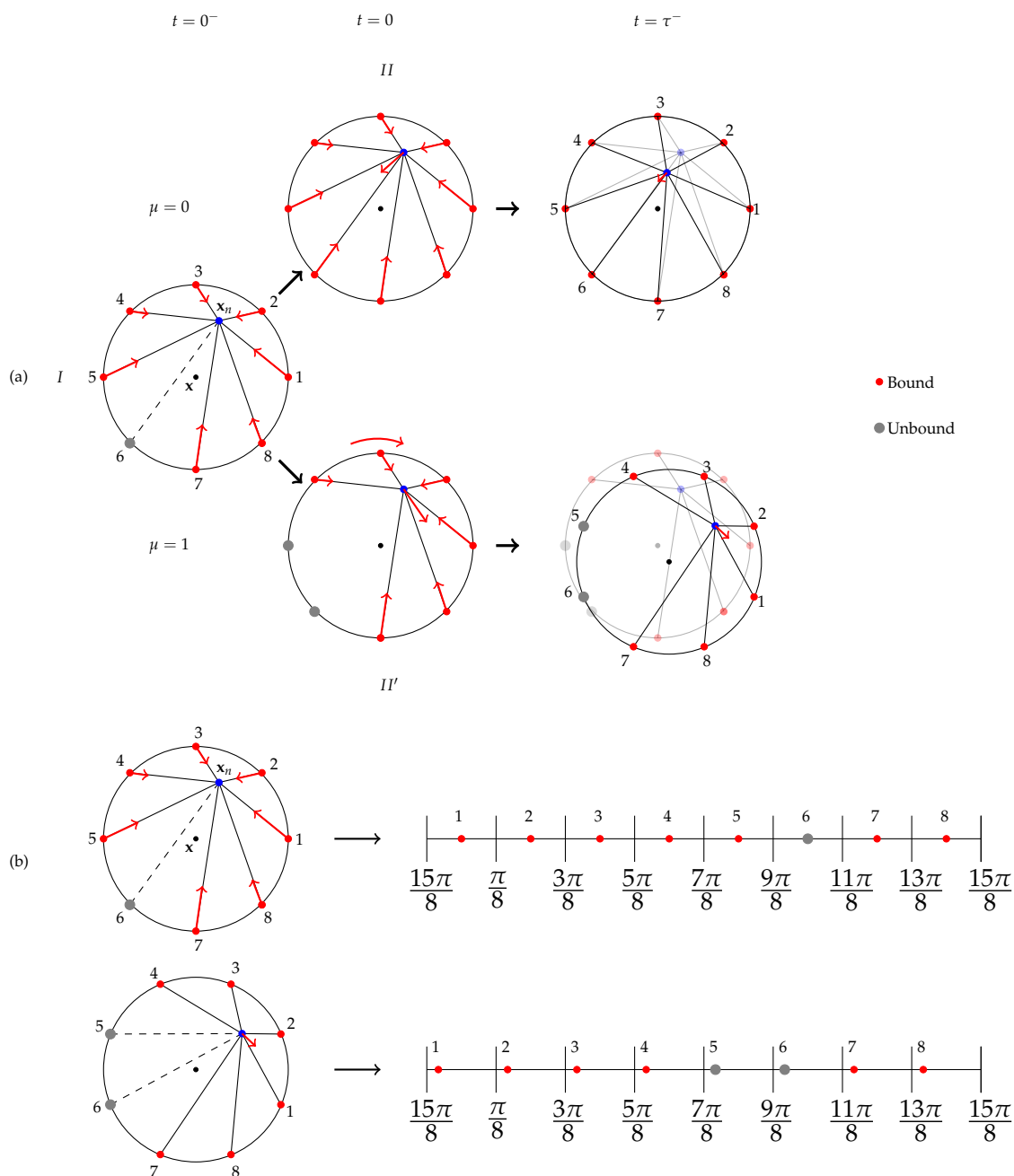


Figure 4. (a) Schematic representation of the migration cycle between adhesion events. Suppose that just before an event occurs at time $t = 0$, the cell is in state I . If at time $t = 0$ (de)adhesion occurs, the cell jumps into state the $(II')II$ and the system evolves according to Equation (7) until the next event occurs at time $t = \tau$, after which the cycle begins anew. The scenarios can be characterized as “run” and “tumble” phases in the bottom and top panels, respectively. (b) Schematic representation of the FA positions projected on cell's circumference at $t = 0^-$ and $t = \tau^-$ in the top and bottom panels, respectively.

3. FA Event Model

In the previous section a model of cell motion between FA events has been constructed. Following [50], here I construct a stochastic model describing the random adhesion/deadhesion events and their arrival times. The discussion here differs from the standard approach of the Gillespie algorithm in [50], as I do not assume that the propensity functions vary inappreciably between the reactions. Moreover, it provides a connection to the theory of PDMPs, as the forms of the objects, necessary to define a piecewise deterministic process (see the next section), follow from the derivations here.

3.1. Focal Adhesion Events

Since there are M FAs and since each FA can participate in only two reactions (binding and unbinding), then there are $2M$ total possible reactions. The following convention for enumerating reactions is adopted: reaction j corresponds to a *binding* reaction of the FA site $i = (j + 1)/2$ if j is odd; otherwise reaction j corresponds to an *unbinding* reaction of the FA site $i = j/2$. Let $\mathbf{Y}(t)$ be defined as before.

Let $a_j(\mathbf{y}, t)dt$ be the probability, given $\mathbf{Y}(t) = \mathbf{y} \in \{0, 1\}^M$, $\mu(t)$, $(\mathbf{x}(t), \mathbf{x}_n(t), \theta_1(t))$ and time t , that reaction j will occur in the time interval $[t, t + dt)$. For clarity, the dependence of the rate $a_j(\mathbf{y}, \cdot)$ on $(\mathbf{x}(\cdot), \mathbf{x}_n(\cdot), \theta_1(\cdot))$ and $\mu(\cdot)$ is suppressed. I assume that the rate a_j satisfies the following:

$$a_j(\mathbf{y}, t) = \begin{cases} 0, & \text{if } j \text{ is odd and } y_{(j+1)/2} = 1 \\ 0, & \text{if } j \text{ is even and } y_{j/2} = 0 \\ \neq 0, & \text{else.} \end{cases} \quad (8)$$

That is, if the FA is (un)bound, the probability of the (un)binding reaction is zero; if the FA is (un)bound, the probability of (binding) unbinding is nonzero. This implies that $a_j(\mathbf{y}, t) \neq 0$ for at least one $j \in \{1, \dots, 2M\}$ (for each FA site $i \in \{1, \dots, M\}$, either a_{2i-1} or a_{2i} is nonzero). For consistency of mathematical theory, we must consider the entirety of state space, including the case of FA (un)binding when it is already (un)bound. However, due to Equation (8), we effectively rule out such scenario.

Lemma 1. Let $\mathbf{Y}(t) = \mathbf{y}$. Then the probability that no FA event occurs in the time interval $[t, t + dt)$ is $1 - \sum_{j=1}^{2M} a_j(\mathbf{y}, t)dt + o(dt)$.

Proof. Using the definition of a_j , the probability that reaction j does not happen is $1 - a_j(\mathbf{y}, t)dt$. Then,

$$\prod_{j=1}^{2M} (1 - a_j(\mathbf{y}, t)dt) = 1 - \sum_{j=1}^{2M} a_j(\mathbf{y}, t)dt + o(dt),$$

is the probability that no FA reaction occurs is. \square

Let $K(\tau, j|t, \mathbf{y})d\tau$ be the probability, given $\mathbf{Y}(t) = \mathbf{y}$ and $(\mathbf{x}(t), \mathbf{x}_n(t), \theta_1(t))$ at time t , that the next reaction will occur in the time interval $[t + \tau, t + \tau + d\tau)$ and will be reaction j . Here, again, the dependence on $\mathbf{x}, \mathbf{x}_n, \theta_1$ is suppressed for clarity.

Proposition 2. Let $\tau > 0$ and $\mathbf{Y}(t) = \mathbf{y}$. Then,

$$K(\tau, j|t, \mathbf{y}) = a_j(\mathbf{y}, t + \tau) \exp \left(- \int_t^{t+\tau} \sum_{j'=1}^{2M} a_{j'}(\mathbf{y}, \tau') d\tau' \right).$$

Proof. Let $P(\tau|t, \mathbf{y})$ denote the probability that no reaction occurs in the time interval $[t, t + \tau)$, given \mathbf{y} (and $\mathbf{x}, \mathbf{x}_n, \theta_1$) at time t . Then, by Lemma 1:

$$P(\tau + d\tau|t, \mathbf{y}) = P(\tau|t, \mathbf{y}) \left(1 - \sum_{j=1}^{2M} a_j(\mathbf{y}, t + \tau) d\tau + o(d\tau) \right) \Rightarrow$$

$$\frac{P(\tau + d\tau|t, \mathbf{y}) - P(\tau|t, \mathbf{y})}{d\tau} = -P(\tau|t, \mathbf{y}) \sum_{j=1}^{2M} a_j(\mathbf{y}, t + \tau) + P(\tau|t, \mathbf{y}) \frac{o(d\tau)}{d\tau}.$$

Letting $d\tau \rightarrow 0$ we obtain the following ODE:

$$\frac{d}{d\tau} P(\tau|t, \mathbf{y}) = -P(\tau|t, \mathbf{y}) \sum_{j=1}^{2M} a_j(\mathbf{y}, t + \tau).$$

Since $P(0|t, \mathbf{y}) = 1$, the solution $P(\tau|t, \mathbf{y})$ is given by:

$$P(\tau|t, \mathbf{y}) = \exp \left(- \int_t^{t+\tau} \sum_{j=1}^{2M} a_j(\mathbf{y}, \tau') d\tau' \right).$$

We have then:

$$K(\tau, j|t, \mathbf{y}) = P(\tau|t, \mathbf{y}) a_j(\mathbf{y}, t + \tau) = a_j(\mathbf{y}, t + \tau) \exp \left(- \int_t^{t+\tau} \sum_{j'=1}^{2M} a_{j'}(\mathbf{y}, \tau') d\tau' \right). \quad (9)$$

□

Let $K_{time}(\tau|t, \mathbf{y}) d\tau$ be the probability that the next reaction will occur in the time interval $[t + \tau, t + \tau + d\tau)$, given $\mathbf{Y}(t) = \mathbf{y}$ and $(\mathbf{x}(t), \mathbf{x}_n(t), \theta_1(t))$ at time t .

Let $K_{index}(j|\tau, t, \mathbf{y})$ be the probability that the index of the next reaction is j given $\mathbf{Y}(t) = \mathbf{y}$, $(\mathbf{x}(t), \mathbf{x}_n(t), \theta_1(t))$ at time t and given that the reaction will occur at time $t + \tau$.

By elementary probability theory (using the definition of conditional probability), we know that

$$K(\tau, j|t, \mathbf{y}) d\tau = K_{index}(j|\tau, t, \mathbf{y}) K_{time}(\tau|t, \mathbf{y}) d\tau.$$

Due to Equation (9), we see that:

$$K_{index}(j|\tau, t, \mathbf{y}) = \frac{a_j(\mathbf{y}, t + \tau)}{a_0(\mathbf{y}, t + \tau)}$$

$$K_{time}(\tau|t, \mathbf{y}) = a_0(\mathbf{y}, t + \tau) \exp \left(- \int_t^{t+\tau} a_0(\mathbf{y}, \tau') d\tau' \right), \quad (10)$$

where

$$a_0(\mathbf{y}, t) = \sum_{j=1}^{2M} a_j(\mathbf{y}, t),$$

and $a_0 \neq 0$ due to Equation (8).

Obviously,

$$\sum_{j=1}^{2M} K_{index}(j|\tau, t, \mathbf{y}) = 1$$

$$\int_0^\infty K_{time}(\tau|t, \mathbf{y}) d\tau = 1.$$

Thus, if T is (random) time until the next reaction, then its probability density function given by K_{time} , its survival function $S(s)$ is given by (without loss of generality, suppose that $t = 0$):

$$\mathbb{P}(T > s) = S(s) = \exp\left(-\int_0^s a_0(\mathbf{y}, \tau') d\tau'\right), \quad (11)$$

and its (cumulative) distribution function is given by $1 - S(s)$ (one can check this by differentiating the distribution function, given by $1 - S(s)$, with respect to s). Note that the distribution of a random variable is uniquely determined by its distribution function.

Using the proof of Proposition 2 one has the following:

Proposition 3. Let $\tau > 0$ and let $\hat{K}(\tau|t, \mathbf{y})$ be the probability of more than one FA event occurring in the time interval $[t + \tau, t + \tau + d\tau)$, given the state of the system at time t . Then $\hat{K}(\tau|t, \mathbf{y}) = o(d\tau)$ as $d\tau \rightarrow 0$.

Proof. By the proof of Proposition 2:

$$\hat{K}(\tau|t, \mathbf{y}) = P(\tau|t, \mathbf{y})o(d\tau),$$

since, following the definition of a_j , the probability of more than one reaction occurring in time interval $[t, t + d\tau)$ is $o(d\tau)$. \square

Proposition 3 implies that we can neglect the case when more than one FA event occurs at the event time. Thus, an FA event (binding or unbinding) unambiguously corresponds to a switch in motility state. If this were not the case and the probability of two FA events at the same time were not negligible, then binding and unbinding of distinct FAs could occur simultaneously. Since the cell becomes motile after unbinding only [51,52], simultaneous events could lead to ambiguity in determining the motile state of the cell.

3.2. Combining the Cell Motility and the FA Event Model

With the results of the previous section I can now formally state the cyclical mesenchymal cell motility model as a stochastic process (see Figure 4).

Let $t = 0$, $\mathbf{x}(0)$, $\mathbf{x}_n(0)$, $\theta_1(0)$, $\mu(0)$ be given and $\mathbf{Y}(0) = \mathbf{y}^0$.

- The time T_1 of the FA event is chosen such that $\mathbb{P}(T_1 > s) = S(s)$.
- The system evolves according to Equation (7) for $t \in [0, T_1)$.
- At time $t = \tau$, the index j of the FA event is chosen with probability $K_{index}(j|T_1, 0, \mathbf{y}^0)$ \mathbf{Y} and μ jump to new values:

$$\mathbf{Y}(t = \tau) = \begin{cases} \mathbf{y}^0 + \hat{\mathbf{e}}_i, & i = (j+1)/2, \text{ if } j \text{ is odd} \\ \mathbf{y}^0 - \hat{\mathbf{e}}_i, & i = j/2, \text{ else} \end{cases},$$

$$\mu(t = \tau) = \begin{cases} 0, & \text{if } j \text{ is odd} \\ 1, & \text{else} \end{cases},$$

where $\hat{\mathbf{e}}_i \in \mathbb{R}^M$ is the standard basis vector. Note that due to Equation (8), we always have $\mathbf{Y}(t = \tau) \in \{0, 1\}^M$, since the probability of (un)binding of (un)bound FA is zero.

- The cycle starts anew with initial time $t = T_1$ and initial values of other variables at this time: starting at $t = T_1$ the time T_2 of the FA event is chosen such that

$$\mathbb{P}(T_2 > s | T_1) = \exp \left(- \int_{T_1}^{T_1+s} a_0(\mathbf{y}, \tau') d\tau' \right).$$

- The system evolves according to Equation (7) for $t \in [T_1, T_1 + T_2)$ and so on.

One sees that the cyclical process described above is a Markov process, since the evolution of the system depends only on the current state. This completes the formal specification of the model. In the following it will be shown that this process is well-defined.

4. Piecewise Deterministic Process

In this section, I briefly overview a class of piecewise deterministic processes, first introduced by Davis [29]. I then show how the deterministic Equations, describing motion between stochastic focal adhesion events, can be combined to yield a well-defined piecewise deterministic Markov process (PDMP).

4.1. PDMP Overview

Let A be countable and let $\Gamma \subset \mathbb{R}^d$ be open. Let $\mathbf{X}_t \in \Gamma$ and let $\mathbf{H}_\nu : \Gamma \rightarrow \mathbb{R}^d$ for $\nu \in A$.

Let $(\Omega, \mathcal{F}, (\mathcal{F}_t)_{t \geq 0}, \mathbb{P})$ be a filtered probability space, where Ω is a sample space, \mathcal{F} is a σ -algebra on Ω , $(\mathcal{F}_t)_{t \geq 0}$ is a (natural) filtration and \mathbb{P} is a probability measure. Let $E := \{(\nu, \xi) : \nu \in A, \xi \in \Gamma\}$ and let (E, \mathcal{E}) be a Borel space. For details, see Chapter 2 in [30].

I can define the piecewise deterministic process on the state space (E, \mathcal{E}) (for a more detailed general treatment see Davis [30]) by the following objects (here, I first provide a constructive definition. The verification of the conditions and their explicit representation corresponding to our case of cell motility is postponed for the sake of clearer exposition):

- I Vector fields $(\mathbf{H}_\nu, \nu \in A)$ such that for all $\nu \in A$ there exists a unique global solution $\mathbf{X}_t \in \Gamma$ to the following equation:

$$\begin{aligned} \frac{d}{dt} \mathbf{X}_t &= \mathbf{H}_\nu(\mathbf{X}_t) \\ \mathbf{X}_0 &\in \Gamma. \end{aligned} \tag{12}$$

Let $\phi_\nu : [0, \infty) \times \Gamma \rightarrow \Gamma$ denote the flow corresponding to Equation (12), i.e.

$$\phi_\nu(t, \mathbf{X}_0) = \mathbf{X}_t.$$

- II A measurable function $a_0 : E \rightarrow \mathbb{R}_+$ such that the function $s \mapsto a_0(\nu, \phi_\nu(s, \mathbf{X}_0))$ is integrable.
- III A transition measure $Q : \mathcal{E} \times E \rightarrow [0, 1]$, such that for fixed $C \in \mathcal{E}$, $(\nu, \xi) \mapsto Q(C; (\nu, \xi))$ is measurable for $(\nu, \xi) \in E$ and $Q(\cdot; (\nu, \xi))$ is a probability measure for all (ν, ξ) on (E, \mathcal{E}) .

Let $(\nu^0, \mathbf{X}^0) \in E$ at time $t = 0$ be given. Let a survival function S be defined similarly as in Equation (11):

$$S(t, (\nu, \mathbf{X})) := \exp \left(- \int_0^t a_0(\nu, \phi_\nu(s, \mathbf{X})) ds \right). \tag{13}$$

Let T_1 be the first jump time such that

$$\mathbb{P}(T_1 > t \mid (\nu^0, \mathbf{X}^0)) = S(t, (\nu^0, \mathbf{X}^0)),$$

and let (v^1, \mathbf{X}^1) be distributed according to the probability law $Q(\cdot, \phi_{v^0}(T_1, \mathbf{X}^0))$. Then, the motion of (v_t, \mathbf{X}_t) for $t \leq T_1$ is given by:

$$(v_t, \mathbf{X}_t) = \begin{cases} (v^0, \phi_{v^0}(t, \mathbf{X}^0)), & t < T_1, \\ (v^1, \mathbf{X}^1), & t = T_1. \end{cases}$$

At time $t = T_1$ the next jump time T_2 is distributed such that

$$\mathbb{P}(T_2 - T_1 > s \mid (v_{T_1}, \mathbf{X}_{T_1})) = S(s, (v_{T_1}, \mathbf{X}_{T_1})).$$

The value of the process at the jump time T_2 is determined by the measure $Q(\cdot, \phi_{v_{T_1}}(T_2, \mathbf{X}_{T_1}))$ and the process continues in a similar way. Thus, we have a well-defined piecewise deterministic process [29].

Theorem 1. [29] *The process $(v_t, \mathbf{X}_t)_{t \geq 0}$ is a homogeneous Markov process.*

4.2. Cell Motility and PDMP

In this section I show that the cyclical cell motility model described in Section 3.2 is a well-defined PDMP.

One can show that $\mathbf{F}_i(\mathbf{x}_n, \theta_1)$ satisfies the Lipschitz condition for $(\mathbf{x}_n, \theta_1) \in \Omega_{cell} \cup [0, 2\pi) := D_{cell}$ (the restriction to the interval $[0, 2\pi]$ is due to the periodic dependence on θ_1 in the definition of \mathbf{x}_i . See Section 2). Furthermore, one can show that $\beta_{cell}^{-1} \mathbf{F}(\mathbf{x}_n, \theta_1, \mathbf{Y})$ and $\mu \beta_{rot}^{-1} \|\mathbf{x}_n\| \mathbf{F}(\mathbf{x}_n, \theta_1, \mathbf{Y}) \cdot \hat{\boldsymbol{\phi}}(\mathbf{x}_n)$, given by

$$\begin{aligned} \beta_{cell}^{-1} \mathbf{F}(\mathbf{x}_n, \theta_1, \mathbf{Y}) &= -\beta_{cell}^{-1} \sum_{i=1}^M Y_i \mathbf{F}_i(\mathbf{x}_n, \theta_1) \\ \mu \beta_{rot}^{-1} \|\mathbf{x}_n\| \mathbf{F}(\mathbf{x}_n, \theta_1, \mathbf{Y}) \cdot \hat{\boldsymbol{\phi}}(\mathbf{x}_n) &= -\mu \beta_{rot}^{-1} \|\mathbf{x}_n\| \sum_{i=1}^M Y_i \mathbf{F}_i(\mathbf{x}_n, \theta_1) \cdot \hat{\boldsymbol{\phi}}(\mathbf{x}_n) \end{aligned}$$

also satisfy the Lipschitz condition for $(\mathbf{x}_n, \theta_1) \in D_{cell}$ and arbitrary $\mu \in \{0, 1\}$, $\mathbf{Y} \in \{0, 1\}^M$.

Proposition 4. *Let $\mathbf{x}(0) = \mathbf{x}_0$, $(\mathbf{x}_n(0), \theta_1(0)) \in D_{cell}$. Let $\mu \in \{0, 1\}$, $\mathbf{Y} \in \{0, 1\}^M$. Then there exists a unique solution of the system*

$$\begin{aligned} \dot{\mathbf{x}} &= \mu \beta_{ECM}^{-1} \mathbf{F}(\mathbf{x}_n, \theta_1, \mathbf{Y}) \cdot \hat{\mathbf{r}}(\mathbf{x}_n) \hat{\mathbf{r}}(\mathbf{x}_n) \\ \dot{\mathbf{x}}_n &= \beta_{cell}^{-1} \mathbf{F}(\mathbf{x}_n, \theta_1, \mathbf{Y}) \\ \dot{\theta}_1 &= \mu \beta_{rot}^{-1} \|\mathbf{x}_n\| \mathbf{F}(\mathbf{x}_n, \theta_1, \mathbf{Y}) \cdot \hat{\boldsymbol{\phi}}(\mathbf{x}_n), \end{aligned} \tag{14}$$

for $t > 0$.

Proof. Note that since the evolution of \mathbf{x} is decoupled from the other two equations, it is sufficient to prove the claim for the following subsystem:

$$\begin{aligned} \dot{\mathbf{x}}_n &= \beta_{cell}^{-1} \mathbf{F}(\mathbf{x}_n, \theta_1, \mathbf{Y}) \\ \dot{\theta}_1 &= \mu \beta_{rot}^{-1} \|\mathbf{x}_n\| \mathbf{F}(\mathbf{x}_n, \theta_1, \mathbf{Y}) \cdot \hat{\boldsymbol{\phi}}(\mathbf{x}_n) \end{aligned} \tag{15}$$

Since the right hand side of this system is Lipschitz on D_{cell} and $(\mathbf{x}_n(0), \theta_1(0)) \in D_{cell}$, then there exists a unique solution of the subsystem Equation (15) for time $t \leq t_{D_{cell}}$, where $t_{D_{cell}} = \inf \{t^* > 0 \mid \mathbf{x}_n(t^*) \notin \Omega_{cell}\}$ is the exit time from D_{cell} . By Corollary 1, we see that $t_{D_{cell}} = \infty$. \square

Let $A := \{1, 2, \dots, 2^{M+1}\}$ and let $\alpha : A \rightarrow \{0, 1\} \times \{0, 1\}^M$ be a bijection. This is simply a mapping such that $\alpha(\nu) = (\mu, \mathbf{Y}) \in \{0, 1\} \times \{0, 1\}^M$ corresponds to a particular cell motion and FA states (recall that the former can either be moving or stationary).

Let $(\mathbf{x}(0), \mathbf{x}_n(0), \theta_1(0)) \in \Gamma := \mathbb{R}^2 \times \Omega_{cell} \times [0, 2\pi)$ and denote $\mathbf{X}_t = (\mathbf{x}(t), \mathbf{x}_n(t), \theta_1(t))$. Moreover, let $\mathbf{H}_\nu : \Gamma \rightarrow \mathbb{R}^5$ be such that

$$\mathbf{H}_\nu(\mathbf{X}) := \begin{pmatrix} \alpha_1(\nu) \beta_{ECM}^{-1} \mathbf{F}(\mathbf{x}_n, \alpha_2(\nu), \theta_1) \cdot \hat{\mathbf{r}}(\mathbf{x}_n) \hat{\mathbf{r}}(\mathbf{x}_n) \\ \beta_{cell}^{-1} \mathbf{F}(\mathbf{x}_n, \alpha_2(\nu), \theta_1) \\ \alpha_1(\nu) \beta_{rot}^{-1} \|\mathbf{x}_n\| \mathbf{F}(\mathbf{x}_n, \alpha_2(\nu), \theta_1) \cdot \hat{\boldsymbol{\phi}}(\mathbf{x}_n) \end{pmatrix}, \quad (16)$$

where α_1 and α_2 are, respectively, the first and the second components of α . In this work, the subscript index in α_2 always denotes the second component of α .

Let the probability $(\Omega, \mathcal{F}, (\mathcal{F}_t)_{t \geq 0}, \mathbb{P})$ and state space (E, \mathcal{E}) be defined as in the previous section. The objects (I, II, III) described in Section 4.1 can now be specified.

- I By Proposition 4 we see that for all $\nu \in A$, there exists a unique global solution to (12).
- II Note that in our case the rate function a_0 is given by (recalling Section 3.1):

$$a_0(\nu, \mathbf{X}_t) = a_0(\alpha_2(\nu), \mathbf{X}_t) = \sum_{j=1}^{2M} a_j(\alpha_2(\nu), \mathbf{X}_t).$$

Here, I abuse the notation introduced in Section 3.1: $a_j(\alpha_2(\nu), t) = a_j(\alpha_2(\nu), \mathbf{X}_t) = a_j(\nu, \mathbf{X}_t)$ for $j = 0, \dots, 2M$. Thus, for the integrability condition to be satisfied, I assume that each probability rate function a_j is integrable along the solution of Equation (12). An exact form of the rates a_j satisfying this condition will be given in the subsequent section. Note that a_0 is nonzero, which follows from Equation (8).

- III In our case, the measure $Q(\cdot; (\nu, \xi))$ is given by (recalling Section 3):

$$\begin{aligned} Q(\{\eta\} \times d\xi'; (\nu, \xi)) &= \delta_\xi(d\xi') \sum_{j=1}^M \delta_{\alpha_1(\eta), 0} \frac{a_j^+(\alpha_2(\nu), \xi)}{a_0(\alpha_2(\nu), \xi)} \delta_{\alpha_2(\eta), 1} \prod_{i \neq j}^M \delta_{\alpha_2(\eta)_i, \alpha_2(\nu)_i} \\ &\quad + \delta_{\alpha_1(\eta), 1} \frac{a_j^-(\alpha_2(\nu), \xi)}{a_0(\alpha_2(\nu), \xi)} \delta_{\alpha_2(\eta), 0} \prod_{i \neq j}^M \delta_{\alpha_2(\eta)_i, \alpha_2(\nu)_i}, \end{aligned} \quad (17)$$

where δ is the Kronecker delta function, $\delta_\xi(\cdot)$ is the Dirac measure at ξ , $a_j^+ = a_{2j-1}$ and $a_j^- = a_{2j}$ correspond to, respectively, the binding and unbinding probability rates at FA site j , and $\alpha_2(\cdot)_i$ is the i^{th} component of the vector $\alpha_2(\cdot)$.

The justification for choosing the functions above stems from our deductions in Section 3.1. In particular, the rate function a_0 in (II) is due to (10): the probability density function of the jump time T_{k+1} , given that $T_k \leq t < T_{k+1}$, is given by:

$$\begin{aligned} K_{time}(\cdot | t, \alpha_2(\nu_t)) &= a_0(\alpha_2(\nu_t), \mathbf{X}_t) \exp \left(- \int_0^\cdot a_0(\nu_t, \phi_{\nu_t}(s, \mathbf{X}_t)) ds \right) \\ &= a_0(\alpha_2(\nu_{T_k}), \mathbf{X}_t) \exp \left(- \int_0^\cdot a_0(\nu_{T_k}, \phi_{\nu_{T_k}}(s, \mathbf{X}_t)) ds \right), \end{aligned}$$

which corresponds to the survival function given by Equation (13).

I now turn our attention to the measure Q in Equation (17). The components of \mathbf{X}_t do not jump, and vary continuously in time, i.e., if T_k is the jump time, then $\mathbf{X}_{T_k^-} = \mathbf{X}_{T_k}$ (see Section 3.2), hence the Dirac measure $\delta_\xi(\cdot)$ at ξ in Equation (17). Clearly, such transition of the continuous component \mathbf{X}_t of

the PDMP at a jump time is probabilistically independent of the transition of the discrete component ν . Hence we have the product of the Dirac measure with the sum, which is a discrete measure for the transition of the discrete component.

By Proposition 3, there is only one FA event at a jump time. Hence, for the probability of transition $\nu \rightarrow \eta$ to be nonzero, the vectors of FA states $\alpha_2(\nu)$ and $\alpha_2(\eta)$ must differ only by one component. Consider the following example to illustrate the jump mechanism.

Example. Let $M = 4$, $T_k \leq t < T_{k+1}$ and suppose T_{k+1} , \mathbf{X}_t are given. Let $\nu, \eta \in A$ be such that $\alpha(\nu) = (\mu_\nu, \mathbf{Y}_\nu)$ and $\alpha(\eta) = (\mu_\eta, \mathbf{Y}_\eta)$, where

$$\mathbf{Y}_\nu = \begin{bmatrix} 0 \\ 0 \\ 0 \\ 1 \end{bmatrix}, \mathbf{Y}_\eta = \begin{bmatrix} 0 \\ 1 \\ 0 \\ 1 \end{bmatrix}.$$

Then, by Equation (10), the probability of the transition $\nu \rightarrow \eta$ is given by:

$$\begin{aligned} \delta_{\mu_\eta, 0} K_{index}(3 | T_{k+1} - t, t, \mathbf{Y}_\nu) &= \delta_{\mu_\eta, 0} \frac{a_3(\alpha_2(\nu), \phi_\nu(T_{k+1} - t, \mathbf{X}_t))}{a_0(\alpha_2(\nu), \phi_\nu(T_{k+1} - t, \mathbf{X}_t))} \\ &= \delta_{\alpha_1(\eta), 0} \frac{a_3(\alpha_2(\nu), \mathbf{X}_{T_{k+1}})}{a_0(\alpha_2(\nu), \mathbf{X}_{T_{k+1}})} \\ &= \delta_{\alpha_1(\eta), 0} \frac{a_2^+(\alpha_2(\nu), \mathbf{X}_{T_{k+1}})}{a_0(\alpha_2(\nu), \mathbf{X}_{T_{k+1}})}. \end{aligned}$$

Clearly, the transition $\mathbf{Y}_\nu \rightarrow \mathbf{Y}_\eta$ corresponds to the binding event at FA site 2, explaining the Kronecker delta term (see Sections 2.3 and 3.2). Now, consider the sum in Equation (17) for this example. We see that

$$\prod_{i \neq j}^M \delta_{\alpha_2(\eta)_i, \alpha_2(\nu)_i} \neq 0, \text{ for } j = 2 \text{ only.}$$

We therefore obtain

$$Q(\{\eta\} \times d\boldsymbol{\xi}'; (\nu, \mathbf{X}_{T_{k+1}})) = \delta_{\mathbf{X}_{T_{k+1}}} (d\boldsymbol{\xi}') \delta_{\alpha_1(\eta), 0} \frac{a_2^+(\alpha_2(\nu), \mathbf{X}_{T_{k+1}})}{a_0(\alpha_2(\nu), \mathbf{X}_{T_{k+1}})} \delta_{\alpha_2(\eta)_2, 1}.$$

Note that if at time t the vector of FA states is given by \mathbf{Y}_ν , then there are M possible FA state vectors into which a transition can occur with nonzero probability:

$$\left\{ \begin{bmatrix} 0 \\ 0 \\ 0 \\ 0 \end{bmatrix}, \begin{bmatrix} 1 \\ 0 \\ 0 \\ 1 \end{bmatrix}, \begin{bmatrix} 0 \\ 1 \\ 0 \\ 1 \end{bmatrix}, \begin{bmatrix} 0 \\ 0 \\ 1 \\ 1 \end{bmatrix} \right\}.$$

Similarly as with the rate function a_0 , we can derive Equation (17) from the principles we established before.

Proposition 5. The transition probability measure $Q(\cdot, (\nu, \boldsymbol{\xi}))$ is given by Equation (17) for each $(\nu, \boldsymbol{\xi}) \in E$.

Proof. Let $(v, \xi) \in E$, $\{\eta\} \times d\xi' \in \mathcal{E}$. Let (N, Ξ) and (N_-, Ξ_-) be E -valued random variables before and after the jumps. Then,

$$\begin{aligned} Q(\{\eta\} \times d\xi'; (v, \xi)) &= \mathbb{P}((N, \Xi) \in \{\eta\} \times d\xi' | (N_-, \Xi_-) = (v, \xi)) \\ &= \mathbb{P}(\{\eta\} \times d\xi' | (v, \xi)), \end{aligned}$$

where the random variables were omitted for notational convenience. Then we have:

$$\mathbb{P}(\{\eta\} \times d\xi' | (v, \xi)) = \mathbb{P}(d\xi' | \{\eta\}, (v, \xi)) \mathbb{P}(\{\eta\} | (v, \xi)) = \delta_\xi(d\xi') \mathbb{P}(\eta | (v, \xi)),$$

since $\Xi = \Xi_-$ a.s., by construction of the process. Note that if (H, Z) is a random variable, then, due to α being a bijection:

$$\{H = \eta\} = \{\alpha^{-1}(H) = \alpha^{-1}(\eta)\} = \{\alpha(H) = \alpha(\eta)\}.$$

Since α is a bijection, we have

$$\begin{aligned} \mathbb{P}(\eta | (v, \xi)) &= \mathbb{P}((\alpha_1(\eta), \alpha_2(\eta)) | (\alpha_1(v), \alpha_2(v)), \xi) \\ &= \mathbb{P}(\alpha_1(\eta), \alpha_2(\eta) | \alpha_2(v), \xi), \end{aligned}$$

since, by construction of the cell motility process, the new FA state $\alpha_2(\eta)$ is determined independently of whether a cell was moving or not (represented by $\alpha_1(v) \in \{0, 1\}$) and the new motility state $\alpha_1(\eta)$ is determined only by which FA event took place (binding or unbinding), regardless of whether a cell was previously moving or not.

Note that when a jump occurs, then, by Proposition 3, only one of $j = 1, \dots, 2M$ possible (binding and unbinding) FA events occurs. Thus, for $j, j' \in \{1, \dots, 2M\}$ and $j \neq j'$ the events “reaction j occurs” and “reaction j' occurs” are mutually exclusive. We then have, by the definition of conditional probability:

$$\mathbb{P}(\alpha_1(\eta), \alpha_2(\eta) | \alpha_2(v), \xi) = \sum_{j=1}^{2M} \mathbb{P}(\alpha_1(\eta), \alpha_2(\eta) | j, \alpha_2(v), \xi) \mathbb{P}(j | \alpha_2(v), \xi),$$

where

- $\mathbb{P}(j | \alpha_2(v), \xi)$ is the probability that the FA event j occurs, given $\alpha_2(v)$ and ξ .
- $\mathbb{P}(\alpha_1(\eta), \alpha_2(\eta) | j, \alpha_2(v), \xi)$ is the probability of a jump into cell state $(\alpha_1(\eta), \alpha_2(\eta))$, given $\alpha_2(v)$ and ξ , and that the FA event j occurred.

Let $j \in \{1, \dots, M\}$ and $j^+ = 2j - 1$ and $j^- = 2j$. Due to Equation (10) we have:

$$\mathbb{P}(j^\pm | \alpha_2(v), \xi) = \frac{a_j^\pm(\alpha_2(v), \xi)}{a_0(\alpha_2(v), \xi)}. \quad (18)$$

Furthermore,

$$\begin{aligned} \mathbb{P}(\alpha_1(\eta), \alpha_2(\eta) | j^+, \alpha_2(v), \xi) &= \delta_{\alpha_1(\eta), 0} \delta_{\alpha_2(\eta), j, 1} \prod_{i \neq j}^M \delta_{\alpha_2(\eta), i, \alpha_2(v)_i} \\ \mathbb{P}(\alpha_1(\eta), \alpha_2(\eta) | j^-, \alpha_2(v), \xi) &= \delta_{\alpha_1(\eta), 1} \delta_{\alpha_2(\eta), j, 0} \prod_{i \neq j}^M \delta_{\alpha_2(\eta), i, \alpha_2(v)_i}. \end{aligned}$$

Therefore,

$$\begin{aligned}
 & \sum_{j=1}^{2M} \mathbb{P}(\alpha_1(\eta), \alpha_2(\eta) | j, \alpha_2(v), \xi) \mathbb{P}(j | \alpha_2(v), \xi) \\
 &= \sum_{j=1}^M \mathbb{P}(\alpha_1(\eta), \alpha_2(\eta) | j^+, \alpha_2(v), \xi) \mathbb{P}(j^+ | \alpha_2(v), \xi) \\
 & \quad + \mathbb{P}(\alpha_1(\eta), \alpha_2(\eta) | j^-, \alpha_2(v), \xi) \mathbb{P}(j^- | \alpha_2(v), \xi) \\
 &= \sum_{j=1}^M \delta_{\alpha_1(\eta), 0} \frac{a_j^+(\alpha_2(v), \xi)}{a_0(\alpha_2(v), \xi)} \delta_{\alpha_2(\eta), 1} \prod_{i \neq j}^M \delta_{\alpha_2(\eta)_i, \alpha_2(v)_i} \\
 & \quad + \delta_{\alpha_1(\eta), 1} \frac{a_j^-(\alpha_2(v), \xi)}{a_0(\alpha_2(v), \xi)} \delta_{\alpha_2(\eta), 0} \prod_{i \neq j}^M \delta_{\alpha_2(\eta)_i, \alpha_2(v)_i}.
 \end{aligned}$$

□

Remark 2. As mentioned in the introduction, one can derive the description of cell migration on the mesoscopic scale. If we let $f(t, v, \mathbf{X})$ to be the density of cells with FA state $\alpha_2(v)$ and positions \mathbf{X} at time t , then:

$$\begin{aligned}
 & \frac{\partial}{\partial t} f(t, v, \mathbf{X}) + \nabla_{\mathbf{X}} \cdot (\mathbf{H}_v(\mathbf{X}) f(t, v, \mathbf{X})) \\
 &= -a_0(v, \mathbf{X}) f(t, v, \mathbf{X}) + \sum_{\eta} a_0(\eta, \mathbf{X}) q(v; \eta, \mathbf{X}) f(t, \eta, \mathbf{X}),
 \end{aligned}$$

where $q(v; \eta, \mathbf{X})$ is the probability that FA state will jump from $\alpha_2(\eta)$ to $\alpha_2(v)$, given that the continuous component has value \mathbf{X} . Although it may seem daunting due to the dimensionality of variables, it is still amenable for simplifications and macroscopic scaling. For example, by assuming that subcellular (FA binding/unbinding) events occur at the fastest time scale, changes to cell position at an intermediate scale and appreciable changes to the density function at the slowest scale, one can obtain parabolic-like scaling. See Chapter 7 in [36] for details.

5. Adhesion Kinetics

While I introduced the probability rates of binding and unbinding events, I have not yet fully specified them. Here, I elaborate on how such quantities unambiguously correspond to the relevant subcell dynamics by providing the precise functional forms of the propensity functions.

5.1. Unbinding Rate

Consider the unbinding rate a_j^- of FA adhesion site $j \in \{1, \dots, M\}$ and let $\mathbf{y} \in \{0, 1\}^M$, $\xi = (\mathbf{x}, \mathbf{x}_n, \theta_1) \in \Gamma$. Following Bell [53], the bond disassociation rate under applied force is given by:

$$a_j^-(\mathbf{y}, \xi) = k_{off}^0 e^{\|\mathbf{F}_j(\mathbf{x}_n, \theta_1)\|/F_b} y_j, \quad (19)$$

where k_{off}^0 is the FA disassociation rate under no load, \mathbf{F}_i is the force applied at the FA, given by Equation (1), and F_b is a characteristic force scale. The last factor y_j simply indicates that only bound FAs can unbind (thus satisfying Equation (8)). Clearly, the function in Equation (19) is integrable. Here, I neglect the fact that the force may be applied at the FA (and consequently at the transmembrane receptors) at an angle and assume for tractability of the model that it is applied normally to the FA (hence consider only magnitude).

Remark 3. In the context of cell migration and within the framework of our model, I only consider FA disassembly on the cell periphery (including the lamellae). The primary cause of such FA unbinding has

mechanical, rather than biochemical nature due to the cell contractile mechanism applying load to the adhesions. Although it is known that the Rho family of GTPases (in particular its member RhoA) mediates disassembly of FAs, their effect is indirect: the activity of myosin motors, which generate contractile forces in SFs, is regulated by RhoA [54]. Hence the force dependence of the unbinding rate a_j^- . Recalling the definition of \mathbf{F}_i in Equation (1), such indirect biochemical mediation can be included by considering mediators of the force T_i . In order to keep the model tractable, I omit the interaction between RhoA and myosin motors.

5.2. Binding Dynamics

Consider the binding probability rate a_j^+ of the FA adhesion site $j \in \{1, \dots, M\}$ and let $\mathbf{y} \in \{0, 1\}^M$, $\xi = (\mathbf{x}, \mathbf{x}_n, \theta_1) \in \Gamma$. The probability rate a_j^+ is given by:

$$a_j^+(\mathbf{y}, \xi) = k_{on,j}(\xi)(1 - y_j),$$

where $k_{on,j} : \Gamma \rightarrow \mathbb{R}^+$ is the effective binding rate at FA site j . The last term $(1 - y_j)$ simply indicates that only unbound FAs can bind. Whereas unbinding can be viewed effectively as a bond rupturing under applied tension, a binding reaction, or focal adhesion assembly and maturation, is a highly regulated process. Due to the complexity of the FA assembly process, I focus on two major mediators of FA formation: Rac activity and contractile forces.

5.2.1. Rac Dependence

For simplicity, I assume that the probability of FA formation is directly proportional to local Rac concentration. Consider the case of chemotactic cell migration. Leading edge protrusions preferentially form in the direction of a chemoattractant. Since Rac is required for formation of lamellipodium and FA formation [54], then local Rac activity correlates with the concentration of the chemical cues. Conversely, local Rac activity negatively correlates with chemorepellent.

Let $Q_{cue} : \mathbb{R}^2 \rightarrow \mathbb{R}^+$ denote the concentration of a cue in the spatial domain and let $q : \mathbb{R}^+ \rightarrow \mathbb{R}^+$ denote the Q_{cue} dependent concentration of Rac. Clearly, q is an increasing function for the case of an attractant and a decreasing function for a repellent. Then,

$$k_{on,j}(\xi) \propto q(Q_{cue}(\mathbf{x} + \mathbf{x}_j)),$$

where I recall that \mathbf{x}_j is the position of the j^{th} FA site.

For example, one can take $Q_{cue}(\mathbf{x})$ to be the density of the ECM (or chemoattractant) at $\mathbf{x} \in \mathbb{R}^2$ and take $q(x) = x$. Then, the probability of binding is simply proportional to the ECM (or chemoattractant) density. This corresponds to a bi-molecular reaction rate, which depends on the *number* of one of the reactants (FA) and on the *concentration* (ECM or a chemoattractant) of the other. Although a more complex function q can be considered, such as those in [55–57], in order to keep the minimal character of the model, I opted for simple linear relation. Moreover, following Model 4 in [56] and assuming no feedback with phosphoinositides, then in a steady state we have:

$$\begin{aligned} R &= \bar{R} \frac{\alpha}{\delta_R} C + \bar{R}(\hat{I}_R + Q_{cue}) \\ \rho &= \frac{\bar{\rho}}{\delta_\rho} \frac{\hat{I}_\rho}{1 + \left(\frac{R}{a_2}\right)^n} \\ C &= \frac{\bar{C}}{\delta_C} \frac{\hat{I}_C}{1 + \left(\frac{R}{a_1}\right)^{n'}}, \end{aligned}$$

where R, ρ, C denote the concentrations of Rac, RhoA, Cdc42 and the rest are constant parameters (see [56] for details). That is, there is a linear dependence of Rac on an external cue.

5.2.2. Force Dependence

The enlargement of nascent (immature) adhesions is concurrent with their maturation into focal adhesions [39,58]. Thus, enlargement and maturation are synonymous. While the initial stage of adhesion growth is force-independent [58], maturation occurs in a force-dependent manner [39,59,60].

However, during such a force-dependent maturation, the positive correlation between the adhesion size and the applied tension exists only in the initial stages of maturation. As FAs increase in size, the effect of applied force diminishes [59].

That is, the study by Stricker et al. [59] showed that for mature FAs there is no correlation between applied force and FA size. One can consider an adhesion site as mature when its size reaches $\sim 1 \mu\text{m}^2$ (see e.g., [61,62]).

Choi et al. [58] showed that nascent adhesions assemble at a rate of $\sim 1.3 \text{ min}^{-1} = 0.021 \text{ s}^{-1}$ reaching a size of $\sim 0.2 \mu\text{m}^2$. Furthermore, it was shown that the formation of these adhesions is independent of the surrounding environment's mechanical properties (such as fibronectin density and stiffness) [58] and force generation within the cell (i.e., myosin II activity) [58,63,64].

Let k_{on}^0 be the force-independent FA maturation (binding) rate. Since FAs are larger in size than immature adhesions, which assemble at a rate of 0.021 s^{-1} , then their assembly is slower and hence I take $k_{on}^0 = 0.01 \text{ s}^{-1}$. It is now needed to find a function that could represent force dependence of FA maturation rate. Denote this function $k_{force} : \mathbb{R}^+ \rightarrow \mathbb{R}^+$.

It satisfies the following:

- $k_{force}(0) = k_{on}^0$, i.e., if there is no force applied, the rate is k_{on}^0 .
- If the applied force is below the characteristic force F_b , then k_{force} is greater than the unbinding rate, i.e., it is more likely that an FA increases in size than that it ruptures.
- If the characteristic force F_b is applied, the rate k_{force} should equal the unbinding rate, i.e., I assume that there is a dynamic equilibrium in some sense.
- If the applied force is larger than F_b , then the unbinding rate dominates the binding rate. Note that as FA increases in size, the force dependence diminishes [59]. Thus, k_{force} should plateau around F_b . I also assume that for large applied forces k_{force} plateaus at k_{on}^0 , since exceeding loads rupture integrin bonds frequently and impede stable maturation.

The following form of k_{force} satisfies the conditions above:

$$k_{force}(F) = \begin{cases} \frac{k_{off}^0 e + k_{on}^0}{1 + \exp(-\gamma_1(F - F_1^*)/F_b)} + k_{on}^0 - \epsilon, & F \leq F_b \\ \frac{k_{off}^0 e + k_{on}^0}{1 + \exp(\gamma_2(F - F_2^*)/F_b)} + k_{on}^0, & \text{else} \end{cases}, \quad (20)$$

where $F_1^* = F_b/4$ and $F_2^* = 5F_b/4$ are the midpoints of the sigmoid functions (see Figure 5). To find the values of γ_1 , γ_2 and ϵ , see Appendix B.

Remark 4. Chan and Odde [65] showed that adhesion site dynamics depends on substrate stiffness. In particular, they showed that for a stiff substrate the transmembrane bonds rupture more frequently, compared to the case with softer substrate under the same load, since the critical load is reached faster. This mechanism provides means for a cell to assess the surrounding rheology. Within the context of our model, this means that the force F_b is smaller for the stiffer substrate, thus increasing the disassociation rate for the same load (see Equation (19)). Consequently, the force dependent binding rate k_{force} also changes for the stiffer ECM. In this case, the curves in Figure 5 will shift to the left. Therefore, our model provides an opportunity to include mechanosensitivity of migrating cells by considering the relevant dynamics for individual FAs.

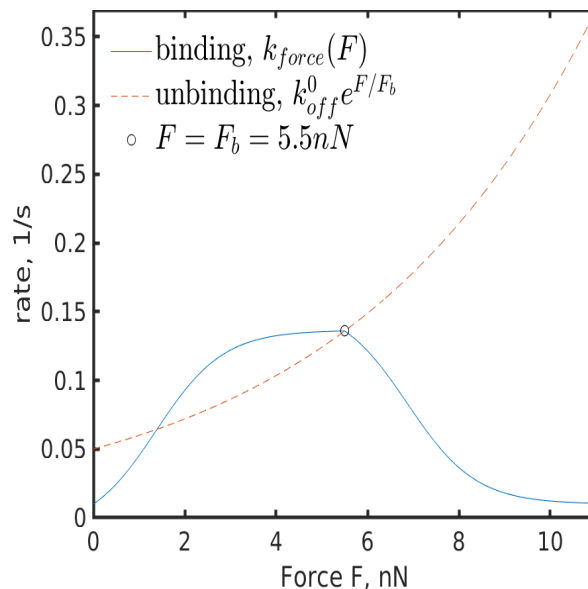


Figure 5. Force dependence of unbinding and binding rates.

Therefore, the binding propensity rate a_j^+ of an adhesion $j \in \{1, \dots, M\}$ is given by:

$$a_j^+(\mathbf{y}, \xi) = q(Q_{cue}(\mathbf{x} + \mathbf{x}_j))k_{force}(\|\mathbf{F}_j(\mathbf{x}_n, \theta_1)\|)(1 - y_j). \quad (21)$$

6. Numerical Simulations

Here, I show the results of simulating cell trajectories under different scenarios, which represent various experimental settings, namely:

1. Uniform environment with no cues.
2. Non-uniform environment with external cue gradient and uneven myosin motor activity within a cell.
3. Striped ECM architecture.

Note that the total number of adhesion sites M is a free parameter, which differs from cell to cell. Nevertheless, it is a crucial parameter, determining whether the motility type is amoeboid or mesenchymal. Amoeboid motility is characterized by a large number of weak adhesions, high turnover and more contractile cell body. On the other hand, mesenchymal migration relies on fewer, but stronger focal adhesions with slower turnover and lower overall contractility. The cells with the former motility type are faster and have more diffusive motion [31,66]. Note that if $a_j^\pm \sim O(1)$, then the rate function is $a_0 \sim O(M)$. Therefore, adhesion events occur more frequently for increasing M , implying higher adhesion turnover. Thus, by varying M , our model is capable of explaining this particular aspect of the difference between the two migration types.

For all scenarios the same initial conditions for all cells are employed. Namely, at $t = 0$ the conditions are:

- \mathbf{x} is at the origin, \mathbf{x}_n is uniformly distributed on a circle with radius R_{cell} , and $\theta = 0$.
- Each FA is in (un)bound state and each cell is in moving state with probability $1/2$.

I simulate trajectories of $n_{cell} := 56$ cells for time $t_{end} := 600$ min. The time interval is divided into $n_{time} := 5000$ intervals, at the end of which the cell centroid positions \mathbf{x} are recorded. For details on the parameters and numerical methods used for simulations, see Appendices B and D, respectively. For details on the data analysis, see Appendix C.

6.1. Uniform Environment

The results of the simulation with uniform spatial cue Q_{cue} are presented in Figure 6. Due to the absence of spatial variation of Q_{cue} , $q = 1$ in Equation (21).

The cell trajectories with varying number of adhesion sites, depicted in Figure 6a–c, show no clear trend and resemble those of a Brownian motion. Indeed, fitting the mean-squared displacement $msd(t)$ to the curve $\widehat{msd}(t) = \beta_0 t^{\tilde{\beta}}$ (see Appendix C for details), we see that the exponent is $\tilde{\beta} \approx 1$ for the three cases (see Figure 6d–f). This suggests that the cell motion has diffusive characteristics in this scenario. In Figure 6g–i, we see the simulated distribution of speeds. The average speeds s_{av} (and the interquartile range, s_{IQR} , see Appendix B for details) and the parameters β_0 , $\tilde{\beta}$ are shown in Table 1. We see that as M increases, the cell motion becomes progressively faster and more diffusive (since $\tilde{\beta} \sim 1$, the slope β_0 is a measure of diffusivity. See Appendix C), which is expected for a dominantly amoeboid type of motility. As a result of $\tilde{\beta} \sim 1$, I can estimate the diffusion coefficient $D = \beta_0/4$. The obtained values are lower, but within an order of magnitude estimated by Liu et al. [31], who found that $D \approx 2.7 \mu\text{m}^2/\text{min}$. Interestingly, the gamma distribution gives a very good fit to the simulated data for various values of M , suggesting that cell speeds are gamma distributed. Moreover, the computed values of the average speed s_{av} fall in the range reported by Liu et al. [31], who found the speeds to be in the range from $0.2 \mu\text{m}/\text{min}$ to $7 \mu\text{m}/\text{min}$. Although there are very high speeds observed in Figure 6i, which seem to be outliers, speeds as high as $25 \mu\text{m}/\text{min}$ have been observed [67]. As expected, rose plots of normalized velocities show no bias in any particular direction in Figure 6j–l. Along with time scaling of the squared displacement, persistence of motion can be measured by directionality ratio (distance between cell centroids divided by path length) and velocity autocorrelation [68]. Expectedly, Figure 7 illustrates that the cells strongly deviate from straight-path migration (Figure 7 (left); see also time average of the directionality ratio \bar{r} in Table 1) and the deviation directions are uncorrelated (Figure 7 (right)). The rapid decay in Figure 7 (right) also suggests that correlations in time become stationary very fast. The increased oscillations in Figure 7 (right) towards the end of the observation window are due to decreased number of observations (see Appendix C).

Although our results show in Figure 6d–f the mean-squared displacement scales diffusively (i.e., linearly) with time, this is not consistent with the reported results. For example, Dietrich et al. [23], Liang et al. [24] and Liu et al. [31] showed that the displacement scales superdiffusively. In these studies it was experimentally found that the time scaling went as $\sim t^{\tilde{\beta}}$, where $\tilde{\beta} \approx 1.2 - 1.5$. The primary reason why, in our case, we have diffusive behaviour is that, given a certain state of adhesion sites, there is a complete circular symmetry of the probability rates a_j^\pm with respect to \mathbf{x}_n variable. Due to this symmetry, then, the probability of moving in one direction is exactly the same as the probability of moving in the opposite direction if we rotate \mathbf{x}_n by π radians. Hence, somewhat reminiscent of a random walk, we have a diffusive time scaling of the squared displacement. Moreover, this symmetry of the probability rates is somewhat idealistic, since it implies that the signaling activity relevant for adhesion dynamics is homogeneous within a cell. One of the ways to break this symmetry, is to multiply each binding probability rate a_j^\pm by $1 + u$, where $u \sim U(-\delta, \delta)$ is uniformly distributed on the interval $(-\delta, \delta)$ with $\delta \in (0, 1)$. Then, on average, the rates are unmodified (the multiplication factor $1 + u$ for each $j = 1, \dots, M$ of every cell is computed at the beginning of simulations and is held fixed thereafter). This way, I not only simulate a non-homogeneous binding rate (and hence, for example, non-homogeneous Rac activity) within a cell, but also simulate otherwise completely identical copies of cells. Such a modification, where one does not explicitly apply a directed, predefined bias can be referred to as chemokinesis [69].

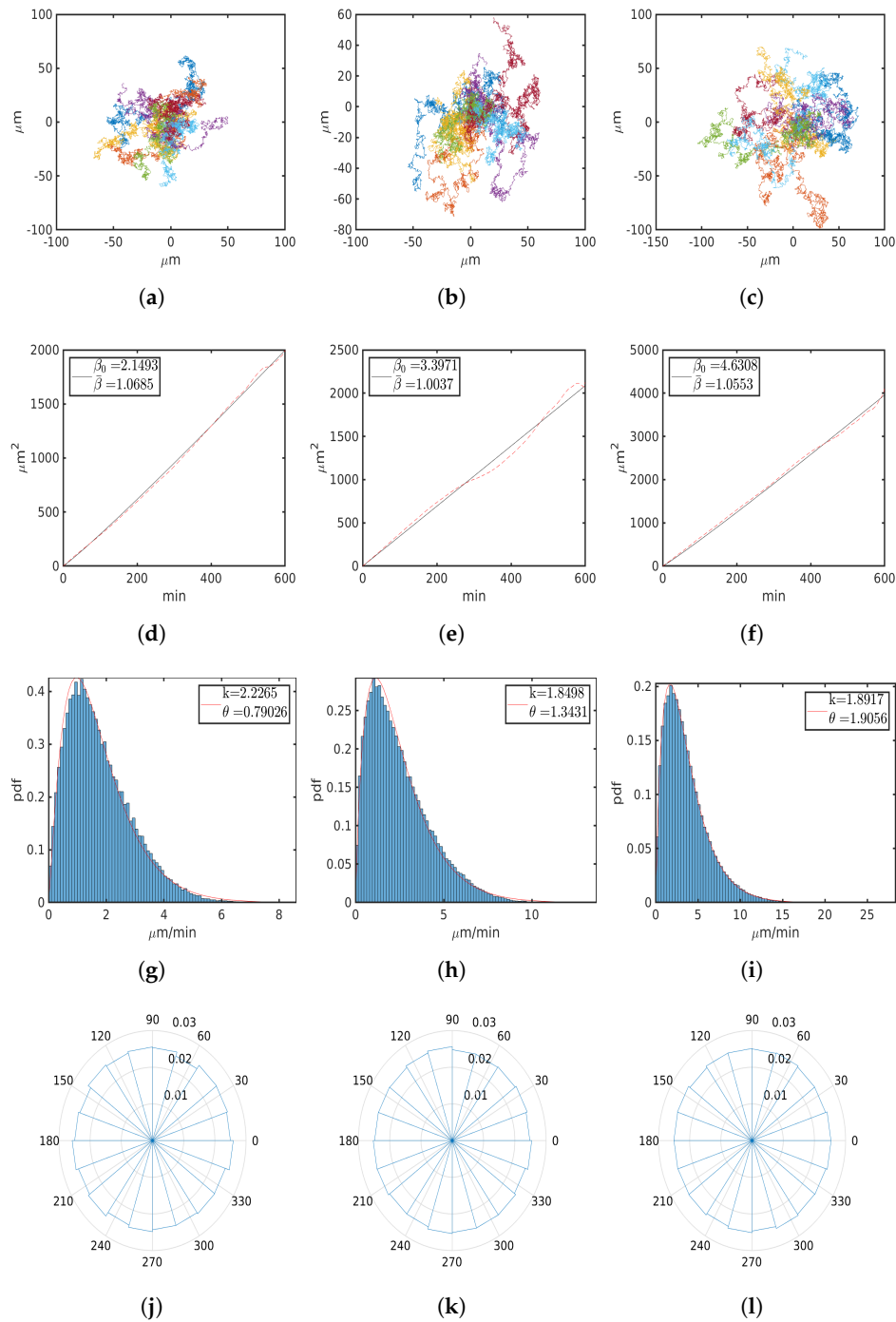


Figure 6. Simulation results with $M = 8, 16, 32$ adhesions in the first, second and third columns, respectively. (a–c) Trajectories of 13 cell centroids $\mathbf{x}(t)$. (d–f) Mean-squared displacements $msd(t)$ (red, dash) and fitted $msd(t)$ (black, solid) with parameters β_0 and $\tilde{\beta}$ (see text for details). The unit of β_0 is $\mu\text{m}^2/\text{min}^{\tilde{\beta}}$. (g–i) Histograms of speed probability density functions and fitted density function of gamma distribution (red) with parameters k and θ . (j–l) Relative frequency histogram of normalized velocities.

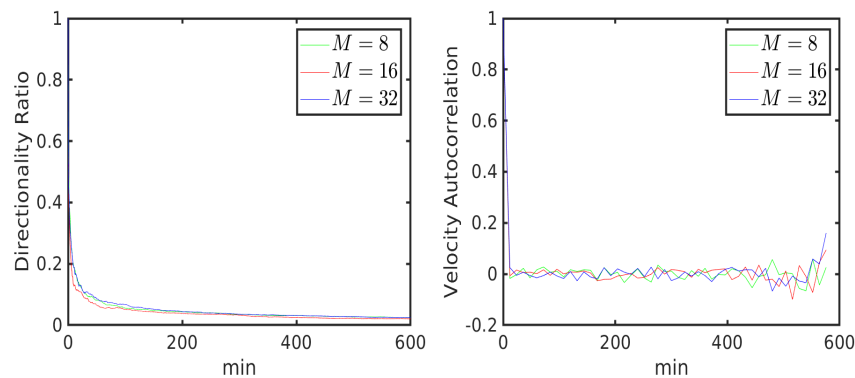


Figure 7. Directionality ratio (**left**) and velocity autocorrelation (**right**) for $M = 8$ (green), 16 (red), 32 (blue).

Table 1. Parameters computed from the simulations.

| M | 8 | 16 | 32 |
|---|----------|-----------|-----------|
| $s_{av}, \mu\text{m}/\text{min}$ | 1.7595 | 2.4845 | 3.6047 |
| $s_{IQR}, \mu\text{m}/\text{min}$ | 1.4557 | 2.217 | 3.1787 |
| $\bar{\beta}, 1$ | 1.0683 | 1.0035 | 1.0552 |
| $\beta_0, \mu\text{m}^2/\text{min}^{\bar{\beta}}$ | 2.1493 | 3.3971 | 4.6308 |
| $\bar{r}, 1$ | 0.0483 | 0.0408 | 0.0497 |

The effect of modifying the rates a_j^+ with $\delta = 0.05, 0.1, 0.15$ can be seen in Figure 8. The cell trajectories, depicted in Figure 8a–c, show that the motion consists of periods with relatively regular path intermingled with highly irregular and random movement. In Figure 8d–f, we see that the rate modification leads to a superdiffusive time scaling of the mean-squared displacement, as the exponent $\bar{\beta}$ becomes larger than one and falls within the experimentally observed range of values [23,24,31]. Moreover, we see that as δ increases, so does $\bar{\beta}$, and the increase of the latter is more pronounced for a larger number of adhesion sites M (see also Table 2). This is due to the fact that as each adhesion site is modified independently, the variance of the modified rates of a cell grows with the number of FAs, which corresponds to increased cell polarization, and hence more prominent persistent motion resulting in higher values of $\bar{\beta}$. However, the distribution of speeds for the corresponding values of M is virtually identical to the case with the unmodified probability rates (Figure 8g–i and Table 2). The uniform distribution of normalized velocities also remained unchanged (Figure 8j–l). These results suggest that in the absence of spatial cues, the distribution of speeds for a given adhesiveness (represented by the total number of adhesions M) remains invariant under symmetry breaking of adhesion binding, while the diffusion type (normal vs. anomalous) does not. Thus, the adhesion number and its turnover is a major determinant of the cell speed, which is consistent with [66].

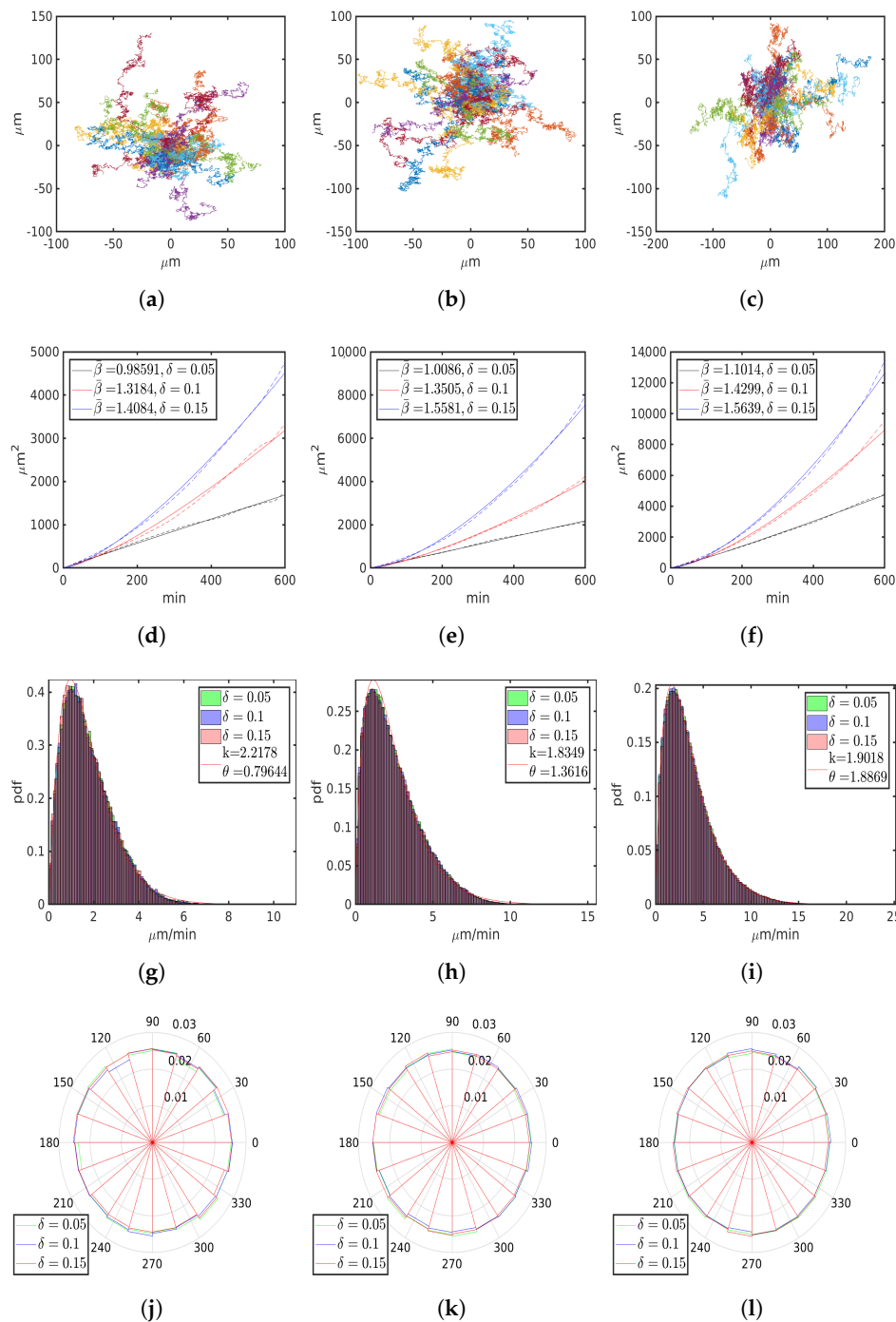


Figure 8. Simulation results with $M = 8, 16, 32$ adhesions in the first, second and third columns, respectively, and with various values of δ . **(a–c)** Trajectories of 27 cell centroids $\mathbf{x}(t)$ with $\delta = 0.1$. **(d–f)** Mean-squared displacements $msd(t)$ (solid) and fitted $\widehat{msd}(t)$ (dash) with $\delta = 0.05$ (black), 0.1 (red), 0.15 (blue). **(g–i)** Superimposed histograms of speed probability density functions and fitted density function of gamma distribution (solid red) with average parameters k and θ (see text for details). **(j–l)** Superimposed histogram of relative frequency of normalized velocities.

Table 2. Parameters computed from the simulations with varying δ .

| M | 8 | | | 16 | | | 32 | | |
|--|----------|--------|--------|-----------|--------|--------|-----------|--------|--------|
| δ | 0.05 | 0.1 | 0.15 | 0.05 | 0.1 | 0.15 | 0.05 | 0.1 | 0.15 |
| $\bar{\beta}, 1$ | 0.9859 | 1.3184 | 1.4084 | 1.0086 | 1.3505 | 1.5581 | 1.1014 | 1.4299 | 1.5639 |
| $s_{av},$ $\mu\text{m}/\text{min}$ | 1.7656 | 1.7768 | 1.7557 | 2.4918 | 2.5009 | 2.5021 | 3.5818 | 3.5735 | 3.6104 |
| $s_{IQR},$ $\mu\text{m}/\text{min}$ | 1.3964 | 1.4319 | 1.472 | 2.24 | 2.2322 | 2.2355 | 3.2136 | 3.1108 | 3.0269 |
| $\beta_0,$ $\mu\text{m}^2/\text{min}^\beta$ | 3.0846 | 0.6934 | 0.5534 | 3.4517 | 0.7103 | 0.3543 | 4.1257 | 0.9536 | 0.5716 |
| $\bar{r}, 1$ | 0.0452 | 0.0519 | 0.0597 | 0.0440 | 0.0513 | 0.0587 | 0.0522 | 0.05 | 0.0623 |

Note that the increased values of $\bar{\beta}$ indicate that the cells explore a larger surface area [68]. However, other indicators of motion persistence are not affected significantly (Figure 9), although migration paths become slightly straighter, as indicated by increased values of \bar{r} (Table 2). These results suggest that symmetry breaking of adhesion binding may allow cells to explore larger area without introducing velocity correlations (Figure 9d–f).

As cell polarization is required for migration even in the absence of external signals, it is not surprising that our results show that an imbalance of adhesion formation within a cell leads to experimentally observed superdiffusive scaling of the squared displacement [23,24,31]. Nevertheless, this highlights a potential mechanism of anomalous diffusion. In the following, I examine whether our model gives biologically consistent results in the case of externally induced polarization.

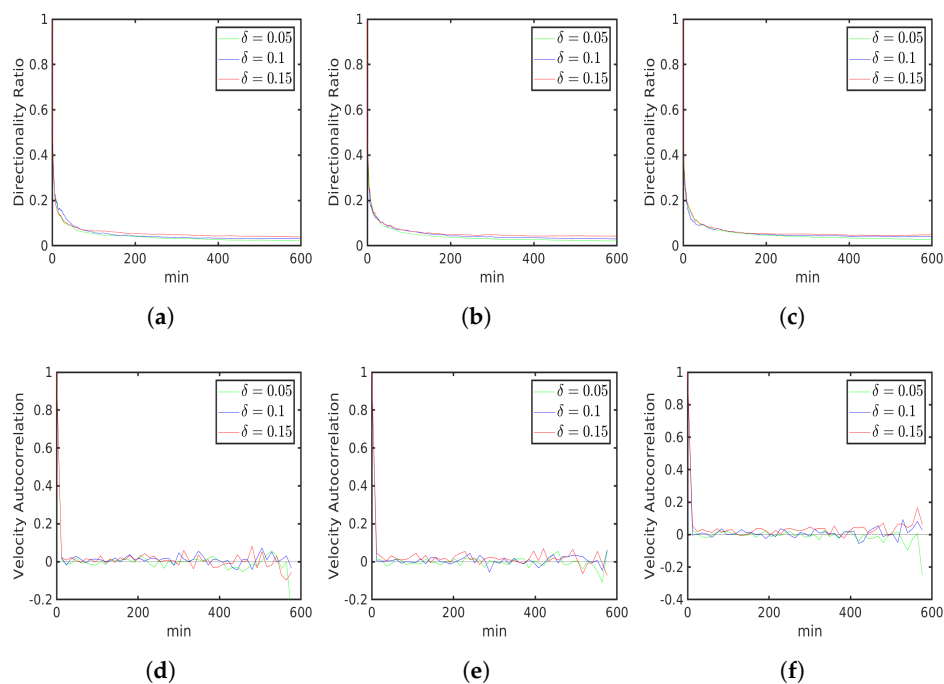


Figure 9. Persistence of motion for cells with $M = 8, 16, 32$ adhesions in the first, second and third columns, respectively, and with $\delta = 0.05$ (green), 0.1 (blue), 0.15 (red). (a–c) Directionality ratio. (d–f) Velocity autocorrelation.

6.2. External Cue Gradient

I first investigate how cell trajectories are varied in the presence of an external cue gradient. If a cue, for example, is a chemoattractant, then it is well known that adhesion formation in a cell is biased in the direction of the attractant. Thus, to simulate such biased migration, I let the functions Q_{cue} and q to have the following form (recall Equation (21)):

$$Q_{cue}(\mathbf{x}) = \begin{cases} 1 + \delta_E x_2, & \text{if } x_2 \geq 0 \\ 1, & \text{else} \end{cases}$$

$$q(Q_{cue}(\mathbf{x})) = Q_{cue}(\mathbf{x}),$$

where δ_E represents the gradient magnitude and x_2 is the second component of \mathbf{x} . Here, for simplicity I took the identity function for q and a linear cue gradient in the y coordinate. This cue can represent, for example, density of ECM or concentration of a chemoattractant. Thus, I simulate, respectively, hapto- or chemotactic migration.

In the presence of a cue gradient, we see that the cell trajectories, shown in Figure 10a–c, exhibit a clear trend in the direction of an increasing concentration. The corresponding plots of the mean-squared displacements show the superdiffusive time scaling in Figure 10d–f, with the exponent $\bar{\beta} > 1$ for all cases. Notice that as the number of adhesion sites M increases, so does $\bar{\beta}$ for the same δ_E (see Table 3). Together with the trajectory plots in Figure 10, our results suggest that in the presence of an external gradient, the taxis becomes more prominent and a cell more sensitive to a cue for increasing number of FAs. Moreover, comparing with the case of a uniform environment, we see that although the amoeboid motility is more diffusive in the absence of external cues, it is also more regular and directed when a cue gradient is present (see Tables 1 and 2 vs. Table 3 and Figures 6 and 8a–c vs. Figure 10a–c). In Figure 10g–i, we see that the evolution of time-averaged exponents $\beta_{av}(t)$ (see Appendix C) have three phases. Following the rapid increase in the first phase, there is a gradual decrease in the rate of change in the second phase, followed by stabilization of $\beta_{av}(t)$ at $\bar{\beta}$. Curiously, a similar behaviour has also been observed by Dieterich et al. [23].

The distribution of speeds again remained invariant and the average speeds are very close to the cases with no external cues (see Table 3). However, the frequency of normalized velocities (see Figure 11d–f show, as expected, that the cell velocities are aligned with the cue gradient. Accordingly, we see that persistent motion emerges: directionality ratio increases compared to unbiased migration (Table 3) and the velocities become correlated (Figure 12d–f). We also observe that an external signal has a stronger impact on motion persistence for higher number of adhesions due to relative increases of \bar{r} and the degree of velocity autocorrelation. Recall that in the presence of, for example, a chemotactic cue, a cell polarizes so that its adhesion dynamics is aligned with the gradient. In particular, adhesions are preferentially formed at the front (where the chemoattractant concentration is larger), and preferentially ruptured at the back. We can see in Figure 11g–i, that our simulation results reproduce such polarized dynamics: the ratio of binding to unbinding events is larger (smaller) than unity in the northern (southern) part of the cells, where the cue is stronger (weaker) relative to the cell centroid. In addition, for a smaller number of adhesion sites, the effects of increasing the cue gradient have a more noticeable effect on the ratios of events (see Figure 11g–i). This is simply due to the reduced density of adhesion sites, which leads to larger relative difference in the concentration of the cue between them. From Figure 13 we can assess the effect of an external cue Q_{cue} on the the binding rate a_i^+ (omitting the force dependence for clarity), since the rate is proportional to Q_{cue} .

Table 3. Parameters computed from the simulations with varying δ_E .

| M | 8 | | | 16 | | | 32 | | |
|--|----------|--------|--------|-----------|--------|--------|-----------|--------|--------|
| δ_E | 0.05 | 0.1 | 0.15 | 0.05 | 0.1 | 0.15 | 0.05 | 0.1 | 0.15 |
| $\bar{\beta}, 1$ | 1.2551 | 1.5051 | 1.52 | 1.3405 | 1.6963 | 1.7545 | 1.5427 | 1.7722 | 1.8569 |
| $s_{av},$ $\mu\text{m}/\text{min}$ | 1.8136 | 1.9133 | 2.0365 | 2.5235 | 2.5972 | 2.6089 | 3.5819 | 3.4218 | 3.3074 |
| $s_{IQR},$ $\mu\text{m}/\text{min}$ | 1.7384 | 1.5461 | 1.6434 | 2.0398 | 2.1999 | 2.1180 | 2.8058 | 2.9067 | 3.0175 |
| $\beta_0,$ $\mu\text{m}^2/\text{min}^\beta$ | 1.0697 | 0.4625 | 0.6845 | 1.0312 | 0.3496 | 0.3654 | 0.8319 | 0.3412 | 0.2242 |
| $\bar{r}, 1$ | 0.0523 | 0.0607 | 0.0693 | 0.053 | 0.08 | 0.097 | 0.0726 | 0.1 | 0.1223 |

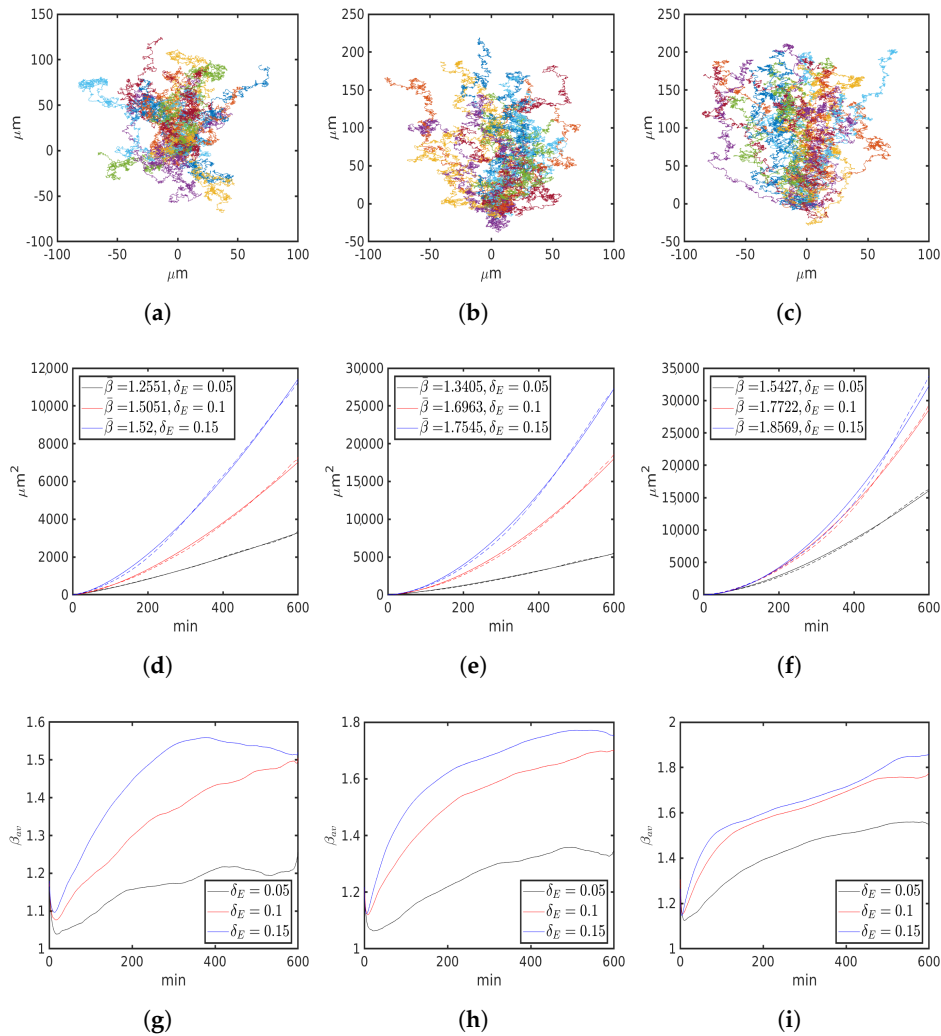


Figure 10. Simulation results with $M = 8, 16, 32$ adhesions in the first, second and third columns, respectively, and with various values of δ_E . (a–c) Trajectories of 27 cell centroids $\mathbf{x}(t)$ with $\delta_E = 0.1$. (d–f) Mean-squared displacements $msd(t)$ (solid) and fitted $\widehat{msd}(t)$ (dash) with $\delta_E = 0.05$ (black), 0.1 (red), 0.15 (blue). (g–i) Time-averaged exponents $\beta_{av}(t)$.

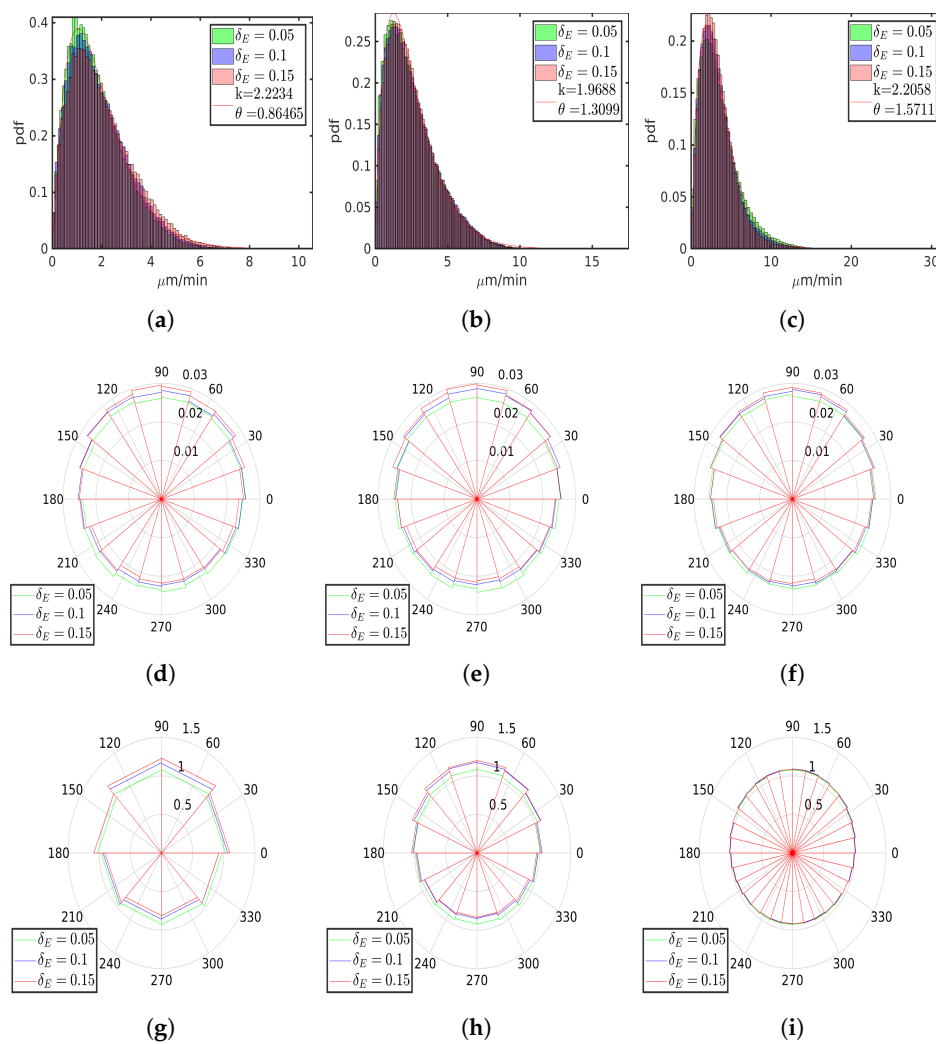


Figure 11. Superimposed histograms of speeds, velocities and adhesion events with $M = 8, 16, 32$ adhesions in the first, second and third columns, respectively, and with various values of δ_E . (a–c) Speed probability density functions and fitted density function of gamma distribution (solid red) with average parameters k and θ (see text for details). (d–f) Relative frequency of normalized velocities. (g–i) Ratio of the number of binding to unbinding events in each sector, such that any given time, only one adhesion site is in each sector.

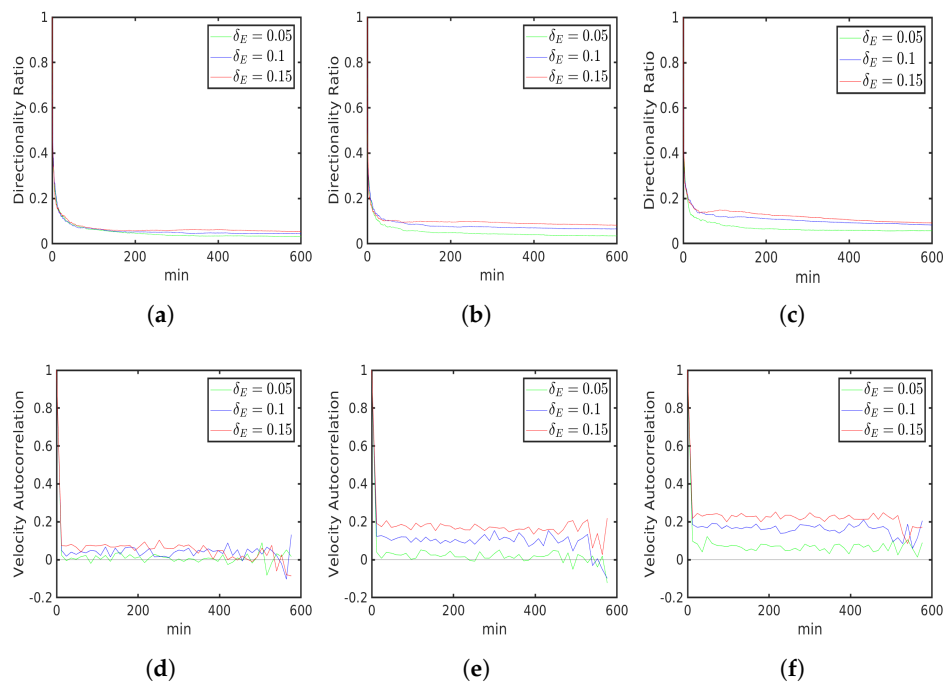


Figure 12. Persistence of motion for cells with $M = 8, 16, 32$ adhesions in the first, second and third columns, respectively, and with $\delta_E = 0.05$ (green), 0.1 (blue), 0.15 (red). (a–c) Directionality ratio. (d–f) Velocity autocorrelation.

Together with Figure 13, the simulations illustrate that directed tactic migration, resulting from biased adhesion formation, follows from the *local* information about the external cue. That is, the spatial dependence of the FA binding rate is solely due to the local concentration of an external cue (see Equation (21)) and no central mechanism for gradient determination was utilized to bias adhesion formation. Consequently, migration along the gradient of an external cue is achieved without its explicit “computation” by the cell.

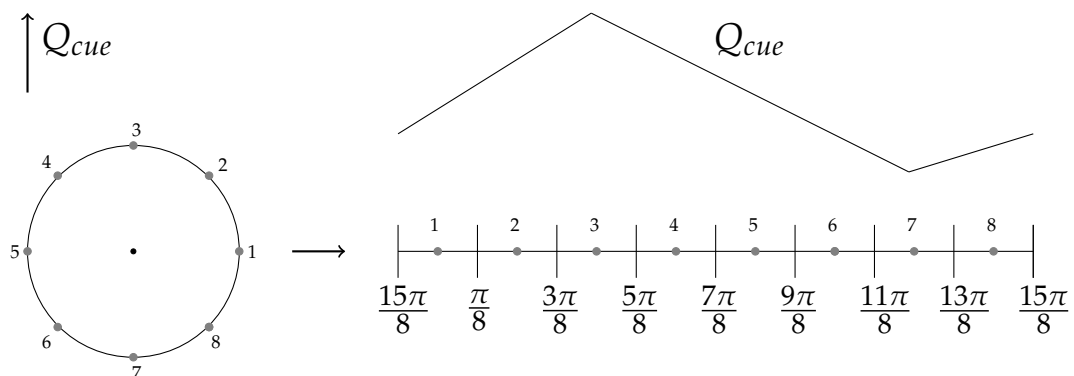


Figure 13. Concentration of an external cue projected on the cell's circumference. Gray bullets represent focal adhesion (FA) sites.

Along with external cue, force dependence of the binding rate is also important for directed migration and without it, the cells do not exhibit biased migration (data not shown). Figure 14 illustrates how the dependence fits into the migration cycle (recall Figure 1a). For the directed migration to occur, at the time of FA disassociation x_n must be preferentially in the rear (Figure 14 step 2). After FA unbinding the increased force at the rear FAs due to extended SFs promotes binding there (Figure 14 step 3). Note that since cell body translocation occurs only after an unbinding event,

formation of new FA in the prospective rear of the cell does not lead to backwards movement. In addition, due to the external signal, more FAs tend to be at the front than at the rear.

Thus, the pulling force exerted by the front on the rear tends to be larger than the opposite and hence the cell moves preferentially in the direction of the gradient. Without the signal, of course, movement becomes unbiased, as shown in the previous section. This suggests that the SF length dependence of the forces (see Equation (1)) and the force dependence of the FA binding rate (see Equation (20)) are necessary for directed migration resulting from biased adhesion formation in the presence of an external signal.

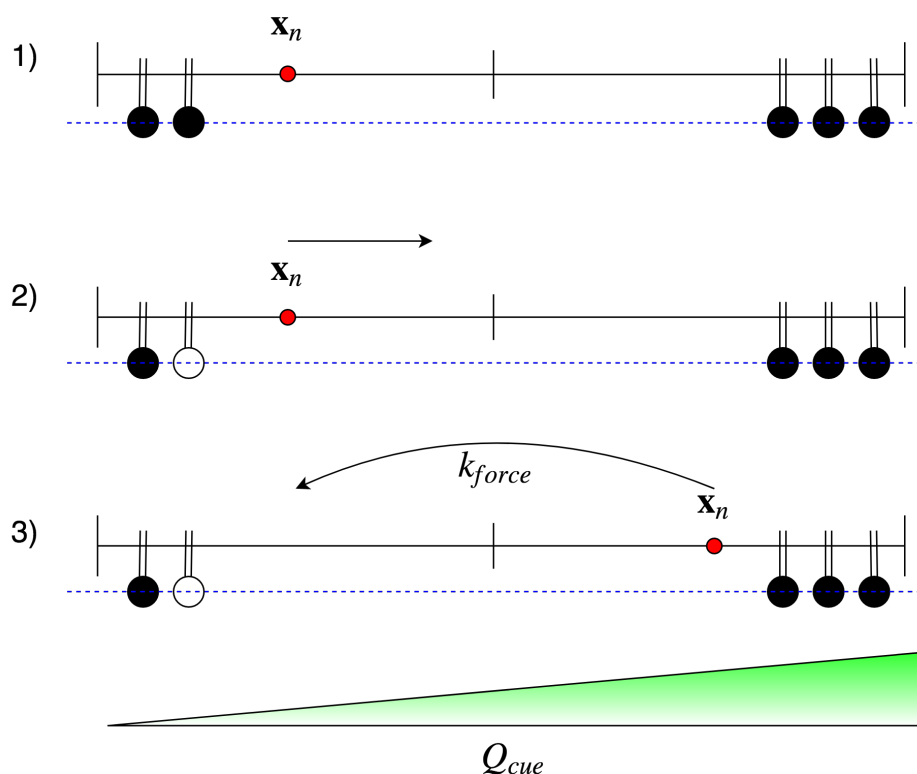


Figure 14. The force dependence of the binding rate and the biased adhesion formation during the migration cycle. Side view schematic of the cell is illustrated, where (un)bound FAs are shown as (white)black circles. (1) Initial configuration. (2) Unbinding leads to cell translocation and motion of x_n within the cell. (3) Increased force on the cell rear (due to its dependence on stress fibre (SF) extension) promotes FA association due to force dependence k_{force} of the binding rate (see Section 5.2.2), after which the cycle begins anew.

6.3. Fibrillar Architecture of ECM

The ECM topography is another important determinant of directed cell migration. In particular, the spatial distribution of the ECM fibres guides the motility by inducing cell shape alignment along the adhesive cues, resulting in characteristic directed movement along the fibre tracts [69]. Such guided migration is called contact guidance [32,69]. Ramirez-San Juan et al. [32] showed that contact guidance can be modulated by micrometer scale variations of interfibre spacing. Inspired by this study, I simulate how subcellular scale fibre spacing influences cell motility, and whether such ECM architecture yields migration patterns characteristic of contact guidance.

Similar to the case with an external cue gradient, the functions Q_{cue} and q have the following form:

$$Q_{cue}(\mathbf{x}) = \begin{cases} 1, & \text{if } \mathbf{x} \in \Omega_{\delta_G} \\ 0.01, & \text{else} \end{cases}$$

$$q(Q_{cue}(\mathbf{x})) = Q_{cue}(\mathbf{x}),$$

where Ω_{δ_G} represents the stripe pattern, $\delta_G = 0.15, 0.25, 0.35$ represents the spacing between stripes such that the distances between them is $\delta_G R_{cell}$ (Figure 15). The stripe width is taken to be $0.25 R_{cell}$. Similarly as in [32], these dimensions are chosen so that a cell is spread on multiple stripes.

The simulation results, shown in Figure 16, indicate that the cell motility has characteristics of contact guidance. Namely, the trajectories show preferential horizontal cell movement (Figure 16a–c), and the displacements are aligned with the fibre pattern (Figure 16d–f). However, increasing the spacing does not simply lead to a greater adhesion alignment along the horizontal direction, as can be observed in Figure 16g–i. Rather, it is the combination of the ECM pattern and the radial position of FAs that gives rise to, for example, definite x-shaped adhesion binding patterns (Figure 16h).

Such binding (and unbinding) pattern leads to fluctuating movement along northwest-southeast and northeast-southwest axis, with the resulting net migration pattern shown in Figure 16b. Similarly, the binding pattern shown in Figure 16i with more frequent events along the equator corresponds to a mixture of diagonal and horizontal movements (Figure 16c), as larger interfibre spacing precludes FA binding at the poles and facilitates adhesion along, as well as across the stripes in x-shaped pattern (see also Figure 15 (right) for illustration of a characteristic FA configuration). On the other hand, smaller spacing also leads to horizontal movement, but with more frequent vertical displacement across the stripes (Figure 16). These results are also in line with conclusions made by in [70], where it was found that adhesion alignment determines contact guidance. I also found that the average speeds were lower than in previous scenarios (Tables 2 and 3): $1.52 \mu\text{m}/\text{min}$, $0.94 \mu\text{m}/\text{min}$ and $0.87 \mu\text{m}/\text{min}$ corresponding to, respectively, $\delta_G = 0.15, 0.25, 0.35$. Interestingly, the average speeds reported in [32] were $\sim 0.6 \mu\text{m}/\text{min}$, although in that study the speeds were nearly constant for varying fibre pattern.

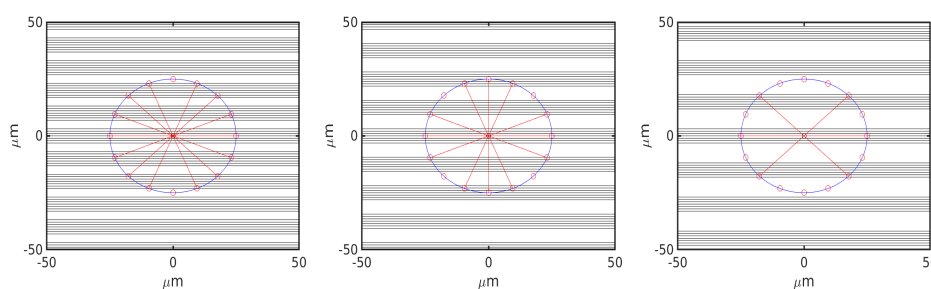


Figure 15. Stripe pattern with $\delta_G = 0.15, 0.25, 0.35$ on, respectively, left, middle and right plots. A cell is illustrated such that each FA on a stripe is bound and cell centre \mathbf{x} coincides with \mathbf{x}_i at the origin.

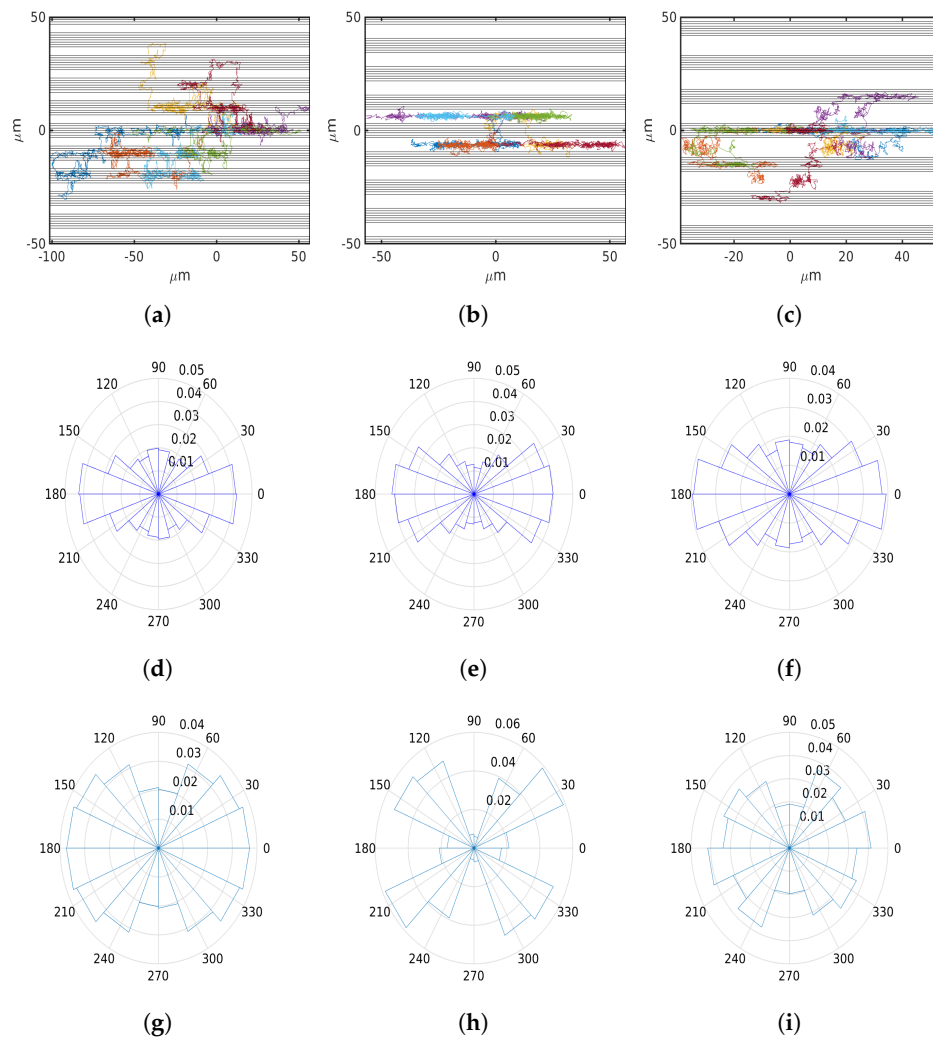


Figure 16. Simulation results with $M = 16$, and $\delta_G = 0.15, 0.25, 0.35$ in first, second and third columns, respectively. (a–c) Trajectories of 7 cells and the striped extracellular matrix (ECM) pattern. (d–f) Relative frequencies of normalized velocities. (g–i) Relative frequencies of binding events in each of the 16 cell sectors.

In Figure 17, I illustrate the characteristic adhesions pattern and the profiles of the FA binding rate corresponding to ECM architecture in Figure 15 (right). Assuming that there is a mechanical equilibrium for simplicity, we see that the adhesion pattern on the cell's periphery reflect the structure of the environment, since low values of Q_{cue} translate into low probability of focal adhesion binding. Alternatively, if the cell is positioned as in Figure 17 (bottom, left), then the adhesion pattern is modified accordingly. Thus, we see that our assumption about constant relative distance of FAs does not preclude the characteristic cell adhesion patterns to reflect environmental inhomogeneities (see also Figure 13).

Altogether, our simulations of contact guidance are, for the most part, consistent with the observations reported in the literature. In particular, I obtain the expected guidance of cell movement (Figure 16a–f) and the geometric constraint of adhesion sites (Figure 16g–i) by the fibrillar ECM pattern, in agreement with [32,69]. Nevertheless, since our model does not explicitly take into account morphological changes in cell shape (recall that in our model cell shape is normalized to a circle; see Section 2) and since cell shape control is essential to contact guidance [32,69], increasing the interfibre distance does not necessarily lead to greater alignment of cell migration along the ECM fibres in our simulations: the values of the guidance parameter G , defined as in [32] (See Appendix C

for details), were found to be 0.64, 0.70, 0.64, corresponding to, respectively, $\delta_G = 0.15, 0.25, 0.35$. Moreover, in the case when the total number of adhesion sites is very low, the stripes are too narrow, and the separation between them is large, then it might occur that all adhesion sites “miss” the stripes, although the cell is spread over multiple stripes. In this case, the probability that any adhesion binds to the substrate is low, which is not biologically consistent. To remedy these shortcomings, the model needs to be extended in order to accommodate strong changes to cell morphology.

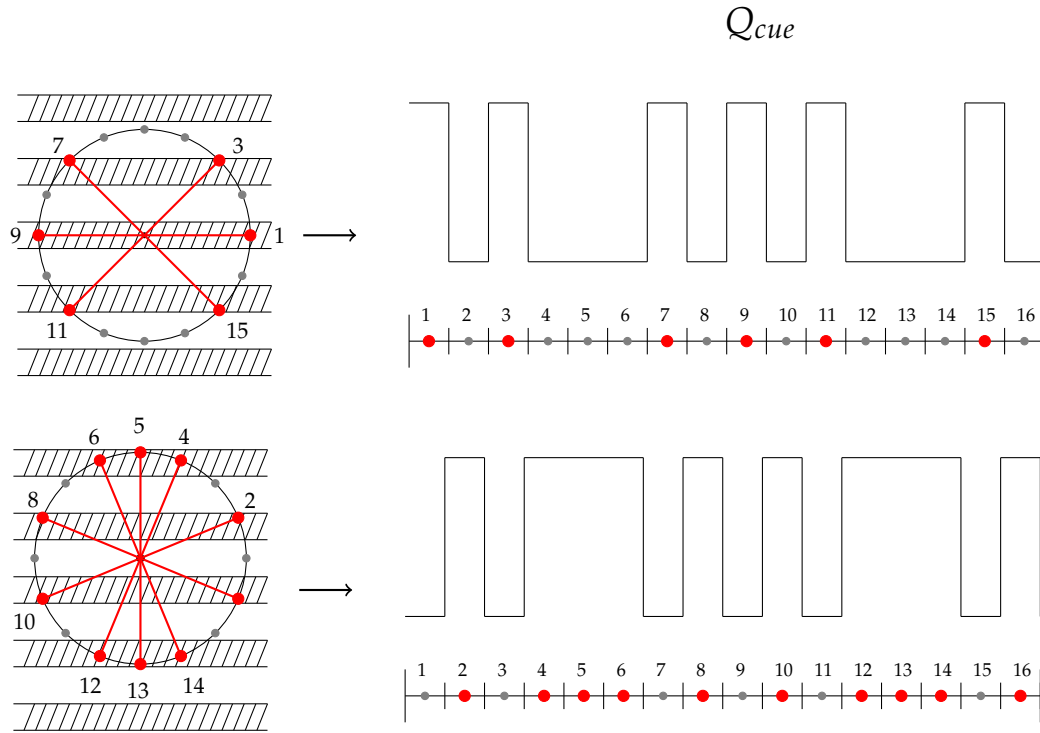


Figure 17. Profiles of an adhesion pattern and an external cue, projected on cell's circumference. Bound and unbound focal adhesions are depicted as red and grey circles, respectively. Stress fibres are also coloured in red.

6.4. Asymmetric Contractility

I now investigate how cell motility is influenced by asymmetrical contractile forces in a cell. Along with preferential adhesion formation, due to, for example, a chemotactic gradient, formation of cell rear by increased actomyosin contractile activity serves as an alternative mechanism by which a directed migration can be induced in the absence of such gradient [52]. In particular, local stimulation of contractility leads to directed motility in the direction opposite to the stimulated area, even in the absence of response to chemotactic stimuli [34]. Here, I show that our model is also capable of capturing such directed movement, triggered by breaking myosin mediated contractile symmetry.

Recall that T_i in Equation (1) denotes the force generated by myosin motors at an adhesion site i . Instead of taking it constant, it varies with the radial position of an FA. Namely, let $T_i : [0, 2\pi) \rightarrow \mathbb{R}_+$ be defined as:

$$T_i(\theta) = \begin{cases} (1 + \delta_{myo})T_{i_0}, & \text{if } \pi < \theta + (i-1)\frac{2\pi}{M} < 2\pi \\ T_{i_0}, & \text{else} \end{cases},$$

where $\delta_{myo} = 0.35, 0.40, 0.45$, T_{i_0} is the constant value used in previous simulations (see Appendix B), and $\theta + (i-1)\frac{2\pi}{M}$ is the radial position of the i^{th} FA. Thus, contractile forces south of cell equator are larger by 35%, 40%, 45% for corresponding values of δ_{myo} . I should, therefore, expect in our simulations

that the northern part of a cell becomes the front due to the imposed contractile symmetry breaking, and that cells will move accordingly (see Figure 18 for illustration).

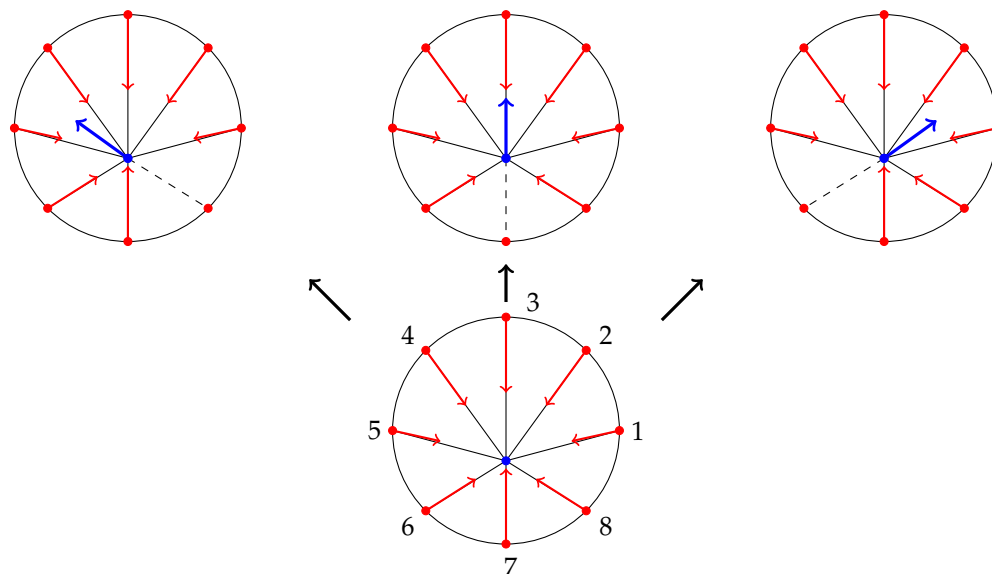


Figure 18. A schematic representation of asymmetric contractility. (Bottom row) Increased contractility causes x_n (blue circle) to shift south of the otherwise equilibrium point in the center. (Top row) Preferential unbinding of FAs south of equator leads to directed movement indicated by blue arrows. See also Figure 4 (II') for schematic representation of cell motility in case of an unbinding event.

Indeed, Figure 19a–c shows, as expected, the trajectories of cells maintaining north-south polarity corresponding to, respectively, front and rear. Since the asymmetry of myosin forces remained during the simulations, the cell's north-south polarity also persisted, resulting in the cell movement that was highly directed along this axis, consistent with [34]. Consequently, higher values of $\beta_{av}(t)$ are calculated, as shown in Figure 19d–f. In particular, for $\delta_{myo} = 0.45$, we see that the time scaling of the mean-squared displacement is close to ballistic (see Table 4 for values of $\bar{\beta}$).

Moreover, increasing the number of FAs leads to more polarized, directed migration. As in the previous cases, neither speed averages (Table 4) nor their distribution (data not shown) changed significantly for a given number of focal adhesions. Interestingly, for $\delta_{myo} = 0.35$, the binding is relatively more frequent in the rear (i.e., south of equator) than in the front, and unbinding is relatively more frequent in the front (i.e., north of equator) than in the back (Figure 19g–i). This suggests, then, that cells were preferentially moving in the southern direction. However, as can be seen in Figure 20, this is not the case. Although movements southwards are more frequent in this situation (due to the above-mentioned event frequencies), the speeds are lower than northward movements: the ratios of the average speeds directed north to the average speeds directed south were found to be 1.0165, 1.0181 and 1.0858 corresponding to, respectively, $M = 8, 16, 32$. The net effect is northward movement. For higher values of δ_{myo} , we see that the unbinding is, expectedly, more frequent in the rear, while binding is preferentially in the front.

Table 4. Parameters computed from the simulations with varying δ_{myo} .

| M | 8 | | | 16 | | | 32 | | |
|--|----------|--------|--------|-----------|--------|--------|-----------|--------|--------|
| δ_{myo} | 0.35 | 0.40 | 0.45 | 0.35 | 0.40 | 0.45 | 0.35 | 0.4 | 0.45 |
| $\bar{\beta}, 1$ | 1.3072 | 1.6325 | 1.7759 | 1.1311 | 1.7905 | 1.8524 | 1.4650 | 1.8892 | 1.9353 |
| $s_{av},$ $\mu\text{m}/\text{min}$ | 1.6230 | 1.5639 | 1.5103 | 2.3742 | 2.3798 | 2.3516 | 3.5861 | 3.7414 | 3.7701 |
| $s_{IQR},$ $\mu\text{m}/\text{min}$ | 1.3827 | 1.4534 | 1.4607 | 2.0273 | 2.0186 | 2.2693 | 3.1370 | 3.2738 | 3.1152 |
| $\beta_0,$ $\mu\text{m}^2/\text{min}^\beta$ | 0.7767 | 0.3659 | 0.2493 | 2.3088 | 0.2893 | 0.3037 | 1.0713 | 0.9894 | 1.2787 |

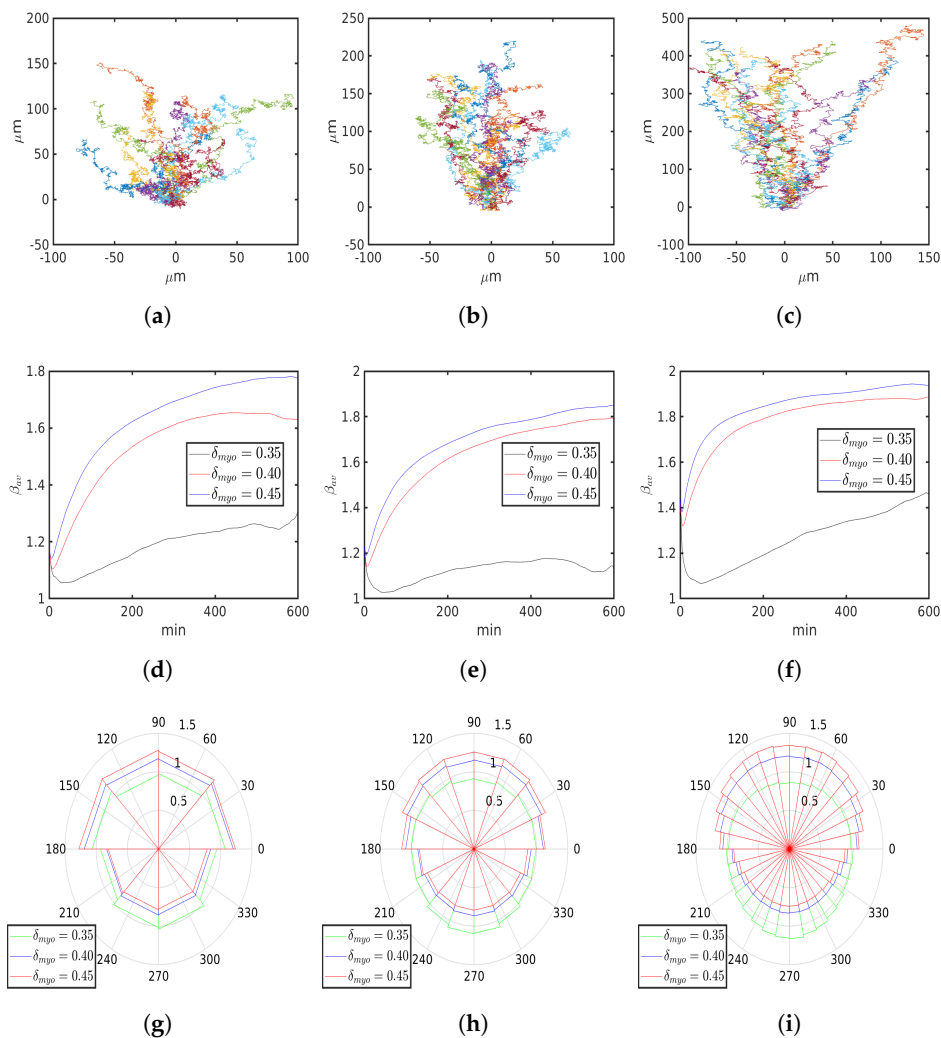


Figure 19. Simulation results with $M = 8, 16, 32$ adhesions in the first, second and third columns, respectively, and with various values of δ_{myo} . (a–c) Trajectories of 13 cells with $\delta_{myo} = 0.4$. (d–f) Time-average exponents β_{av} . (g–i) Ratio of the number of binding to unbinding events in each sector.

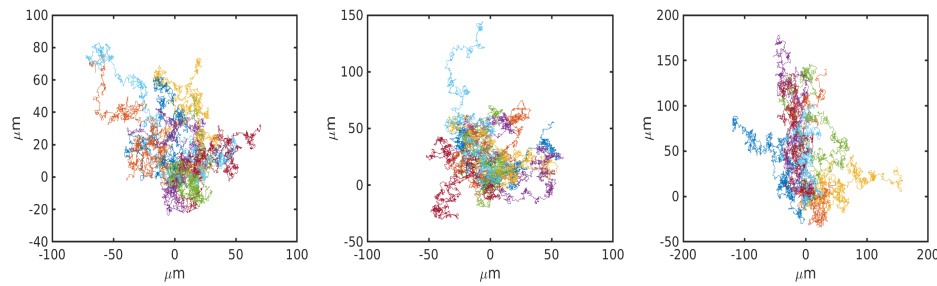


Figure 20. Simulated trajectories with $M = 8, 16, 32$ adhesions with $\delta_{myo} = 0.35$ on left, middle and right plots, respectively.

These adhesion frequency patterns also illustrate the significance of the force dependence of the FA binding rate. Recalling Figure 5, we see that, for $\delta_{myo} = 0.4, 0.45$ (corresponding to $T_i = 1.018F_b, 1.054F_b$), the binding rate dominates unbinding north of equator due to greater SF extension (see Figure 18 for an illustration) leading to increased contractile force. Since the expected adhesion pattern is reversed for $\delta_{myo} = 0.35$ (corresponding to $T_i = 0.981F_b$) and yet the cells migrate northwards, it may suggest that there is a threshold value of δ_{myo} , above which cells can migrate in a certain direction solely by asymmetric contractility, and/or below which cells must additionally bias adhesion formation to do so.

This prompted us to investigate whether varying mechanical properties of SFs can yield the expected adhesion pattern for lower degree of asymmetry, corresponding to $\delta_{myo} = 0.35$. Specifically, I varied the buckling length L_0 and stiffness EA such that $x = (1 + \delta_x)x^0$ corresponds to the modified value of the parameter $x \in \{L_0, EA\}$, where x^0 corresponds to the default value given in Appendix B. In Figure 21a, I see that reducing the buckling length L_0 by 27% leads to the expected adhesion pattern, while reducing it by 18% leaves it largely unchanged. However, decreasing and increasing stiffness when $\delta_{L_0} = -0.18, -0.27$, respectively, leads to the opposite results (Figure 21b,c). This suggests that if SFs are less prone to buckling and less stiff, lower degree of myosin induced contractile asymmetry may be required to drive directed migration.

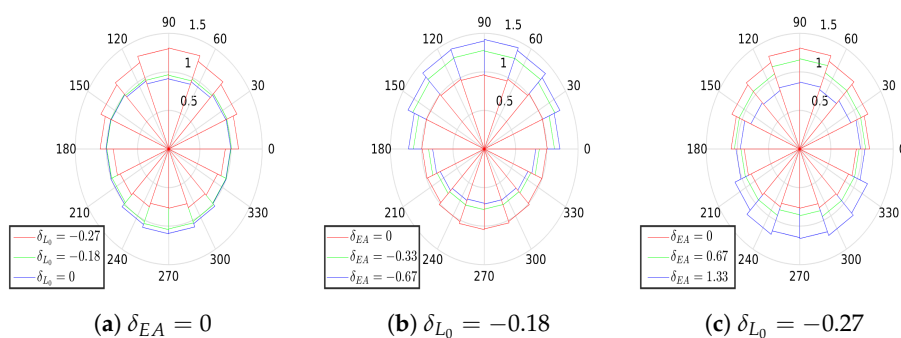


Figure 21. Ratios of the number of binding to unbinding events in each sector with varying buckling length and stiffness of SFs. (a) The effect of reducing the buckling length L_0 with fixed and stiffness value EA . (b,c) The effects of varying stiffness EA for reduced buckling length.

Remark 5. Another way to induce contractile asymmetry is, for example, to decrease the myosin force T_i north of the cell's equator. Then, again, the south of the cell equator is more contractile. However, the simulated trajectories show southward directed movement (data not shown), contrary to what we should expect. Therefore, merely inducing contractile asymmetry is not sufficient. For the expected directed migration to occur, there must be a local increase of contractile forces above some critical level in the prospective cell rear, rather than a local decrease of contractility in the prospective front. Interestingly, Yam et al. [34] were able to initiate directed

movement by increasing local actomyosin contraction, while locally decreasing the contractile activity did not lead to migration initiation. More recently, Shellard et al. [71] showed that directed collective cell migration of neural crest cells requires greater contractility at the rear of the clump.

7. Discussion and Outlook

In this paper I constructed a stochastic model of cell migration using a minimal representation of cellular structures, essential for crawling, such as stress fibres and focal adhesions. Using this representation, and observing that FA assembly and disassembly events of the migration cycle lead to different migratory outcomes, we obtained the Equations describing deterministic cell motion between the random occurrence of FA events. After introducing the rates of FA binding and unbinding, we obtained the remaining necessary objects to define a piecewise deterministic Markov process: the distribution of interarrival times and of the next FA event. Note that the forms of these distributions have been derived, rather than simply postulated. Nonetheless, several biological assumptions were imposed. The most principle of them are:

- The migration cycle is reduced to two steps: FA unbinding leads to movement and cytoskeletal reconfiguration, while binding to the latter only (Section 2).
- Cell shape is assumed to be spherical and constant (Section 2.1).
- The number of adhesion sites (occupied and unoccupied) is constant (Section 2.3).
- Adhesion binding and unbinding depend on the force applied by stress fibres and position of the cell, i.e., we omit intracellular biochemical interactions (Section 5).

We refer the reader to the referenced sections for detailed justifications.

Having specified the coupling between SFs and FAs, as well as between the cellular environment and FAs, I performed numerical simulations. I showed that our model is able to reproduce experimental observations, such as: superdiffusive scaling of the mean-squared displacement [23,24,31] (Figure 8); biased motility in the presence of external cue (Figure 10); contact guidance [32] (Figure 16). In these cases, the obtained results followed solely due to asymmetric, dynamic instability of FAs in direct response to environmental stimuli. Specifically, it is only the biased FA assembly rate that drives biased cell motility along the cue gradient or the fibre tracts (Figures 11 and 16d–i). That is, preferred velocities were not imposed or chosen in any way, but simply followed as a consequence of front-rear polarity, as the cell front is characterized by preferential FA binding and the rear by unbinding.

Another characteristic of directed migration is the asymmetric contraction of actomyosin bundles. By increasing the force generation of myosin motors in the prospective rear, I obtained directed movement in the opposite direction (Figure 20). Here, asymmetric FA dynamics (and so front-rear polarity) were also obtained, but as a consequence of locally induced contractile activity, consistent with [34].

Our simulation results in various settings suggest that the cell speeds follow a gamma distribution (Figures 6g–i, 8g–i and 11a–c). Furthermore, the number of adhesion sites seems to be a determinant of the gamma distribution, as its parameters are similar under different settings and given number of FAs. These results suggest that cell speeds are independent of biased FA formation, i.e., the bias only alters the directionality and not the speed. It is also interesting to see a correlation between the number of adhesion sites and diffusivity (Table 1), as well as average speed (Tables 1–4). Note that faster and diffusive amoeboid movement is characterized by an increased number of weaker adhesions with high turnover and contractility [66]. Thus, the aforementioned correlation is also consistent with experimental observations. I note that our model is not fit to take into account motility strongly relying on cell shape control, which is required, for example, in highly mobile cells. However, the simulations reproduce migration along fibre tracts, where cell reshaping takes place [32]. Our results suggest, then, that adhesion along the tracts is sufficient to produce such migration patterns.

Although the model of the internal contractile machinery driving cell locomotion and cytoskeletal remodelling is simple, the resulting numerical simulations reproduce some important aspects of

migrating cells observed in experiments. Moreover, the cyclical nature of cell motility is captured with our piecewise deterministic model. While migration of a crawling cell is accompanied by changes in its shape, dynamic coupling of cell–substrate adhesions and contractile machinery, i.e., focal adhesions and stress fibres, represent another side of the coin. Numerous sophisticated phase-field or free boundary models that produce realistic morphology of motile cells, often do not emphasize this coupling (and stochasticity) during the migration cycle. I attempted to remedy this issue in our model, and showed with our simulations that numerous aspects of cell migration can be explained without detailed account of cell shape changes. Nevertheless, shape control is essential for a more complete description of the phenomena. I believe this can be done with the framework provided by vertex-based models [72]: a more complex contractility apparatus can be described via active cable network model [41] and a more detailed account of mechanical forces (e.g., protrusions due to actin polymerization) can be done as in [14]. Together with models of RhoGTPases signalling pathways [5,56,73], the most significant drawbacks of our approach (including rigid rotation of the SF structure) can be overcome. The presented framework of piecewise deterministic motility process can also be extended to three-dimensional setting, as neither the event interarrival time distribution, nor the transition measure rely on the particular features of migration in a plane.

However, given the relative simplicity of the stochastic model and its ability to explain a handful of the experimental observations, it is possible to extend the model to include cell–cell collisions in the context of contact inhibition of locomotion (CIL). Here, the collisions lead to cessation of locomotion and to repolarization, such that the formation of new adhesions at the site of contact is inhibited, while contractility is stimulated [74]. Within the framework of our model this can be implemented in a straightforward manner: collisions cause a switch to a non-moving state and the FA probability rates are modified according to contact location, as was done in our work in [35]. Yet another extension is obtained by treating cells as particles and using kinetic theory, yielding Equations governing population migration. Thus, we can achieve a multiscale description of cell motility. Due to limitations in size and scope, cell–cell collisions and population migration will be treated in forthcoming works.

Funding: The research has been carried out during my stay at TU Kaiserslautern, Germany. The funding should read as DAAD (Deutscher Akademischer Austauschdienst grant 57169058).

Acknowledgments: I am very grateful to Christina Surulescu for fruitful discussions and feedback in writing this manuscript. This work has been carried out during my stay in TU Kaiserslautern, Germany.

Conflicts of Interest: The author declare no conflict of interest.

Abbreviations

The following abbreviations are used in this manuscript:

| | |
|------|--|
| FA | Focal adhesion |
| ECM | Extracellular matrix |
| SF | Stress fibre |
| PDMP | Piecewise deterministic Markov process |
| MSD | Mean-squared displacement |

Appendix A. Equations of Cell Motion

In our model, using common, lab’s reference frame will yield the same governing relations, because the involved forces are determined by relative position of cellular structures. Below, I show why this is the case and provide a more detailed explanation regarding the Equation of motions for $\mathbf{x}, \mathbf{x}_n, \theta_1$ presented in Sections 2.1 and 2.2.

Let $\mathbf{x}'_n = \mathbf{x} + \mathbf{x}_n$ and $\mathbf{x}'_i = \mathbf{x} + \mathbf{x}_i$, where primes indicate the corresponding variables in the lab's reference frame (recall that \mathbf{x}_i is the position of the i^{th} FA in cell's reference frame). Then, in this frame, the length of the i^{th} SF L'_i and the unit vector \mathbf{e}'_i along it are given by

$$L'_i = \|\mathbf{x}'_n - \mathbf{x}'_i\| = \|\mathbf{x}_n - \mathbf{x}_i\| = L_i$$

$$\mathbf{e}'_i = \frac{\mathbf{x}'_n - \mathbf{x}'_i}{L'_i} = \frac{\mathbf{x}_n - \mathbf{x}_i}{L_i} = \mathbf{e}_i,$$

respectively. Thus, $\mathbf{F}'_i(\mathbf{x}'_n, \theta_1) = \mathbf{F}_i(\mathbf{x}_n, \theta_1)$, where \mathbf{F}'_i is the force applied by the i^{th} SF at the i^{th} FA. Note that the force at \mathbf{x}'_n (or \mathbf{x}_n) due to the i^{th} SF is $-\mathbf{F}'_i(\mathbf{x}'_n, \theta_1)$ (or $-\mathbf{F}_i(\mathbf{x}_n, \theta_1)$) by action–reaction principle. Therefore, net force \mathbf{F}' at \mathbf{x}'_n is $\mathbf{F}'(\mathbf{x}'_n, \theta_1, \mathbf{Y}) = -\sum_{i=1}^M \gamma_i \mathbf{F}'_i = -\sum_{i=1}^M \gamma_i \mathbf{F}_i = \mathbf{F}(\mathbf{x}_n, \theta_1, \mathbf{Y})$. Neglecting inertia, we have

$$\beta_{\text{cell}} \dot{\mathbf{x}}_n = \mathbf{F}(\mathbf{x}_n, \theta_1, \mathbf{Y}) = \mathbf{F}'(\mathbf{x}'_n, \theta_1, \mathbf{Y}).$$

Now, let us examine the Equations of motion after FA unbinding, stated in Section 2.2.2, but in lab's reference frame. In this frame, the radial unit vector $\hat{\mathbf{r}}'(\mathbf{x}'_n)$ from the cell centre \mathbf{x} is given by (see Figure 3 in the manuscript for illustration)

$$\hat{\mathbf{r}}'(\mathbf{x}'_n) = \frac{\mathbf{x}'_n - \mathbf{x}}{\|\mathbf{x}'_n - \mathbf{x}\|} = \frac{\mathbf{x}_n}{\|\mathbf{x}_n\|} = \hat{\mathbf{r}}(\mathbf{x}_n).$$

Analogously, the tangential unit vector $\hat{\boldsymbol{\phi}}'(\mathbf{x}'_n)$ is given by

$$\hat{\boldsymbol{\phi}}'(\mathbf{x}'_n) = \left(-\frac{x'_{n,2} - x_2}{\|\mathbf{x}'_n - \mathbf{x}\|}, \frac{x'_{n,1} - x_1}{\|\mathbf{x}'_n - \mathbf{x}\|} \right)^T = \left(-\frac{x_{n,2}}{\|\mathbf{x}_n\|}, \frac{x_{n,1}}{\|\mathbf{x}_n\|} \right)^T = \hat{\boldsymbol{\phi}}(\mathbf{x}_n).$$

Note that the tangential component F'_ϕ of the force \mathbf{F}' at \mathbf{x}'_n induces rotational motion, while the radial component F'_r of the force \mathbf{F}' at \mathbf{x}'_n induces translational motion. These components are given by:

$$F'_\phi = \mathbf{F}'(\mathbf{x}'_n, \theta_1, \mathbf{Y}) \cdot \hat{\boldsymbol{\phi}}'(\mathbf{x}'_n) = \mathbf{F}(\mathbf{x}_n, \theta_1, \mathbf{Y}) \cdot \hat{\boldsymbol{\phi}}(\mathbf{x}_n) = F_\phi$$

$$F'_r = \mathbf{F}'(\mathbf{x}'_n, \theta_1, \mathbf{Y}) \cdot \hat{\mathbf{r}}'(\mathbf{x}'_n) = \mathbf{F}(\mathbf{x}_n, \theta_1, \mathbf{Y}) \cdot \hat{\mathbf{r}}(\mathbf{x}_n) = F_r.$$

Neglecting rotational inertia, we then have

$$\beta_{\text{rot}} \dot{\theta}_1 = \|\mathbf{x}'_n - \mathbf{x}\| F'_\phi(\mathbf{x}'_n, \theta_1, \mathbf{Y})$$

$$= \|\mathbf{x}_n\| F_\phi(\mathbf{x}_n, \theta_1, \mathbf{Y})$$

where the right hand side in the first (second) line is the torque due to tangential component of the force \mathbf{F}' (\mathbf{F}) at \mathbf{x}'_n (\mathbf{x}_n). As a result of low Reynolds number, we also have

$$\beta_{\text{ECM}} \dot{\mathbf{x}} = F'_r(\mathbf{x}'_n, \theta_1, \mathbf{Y}) \hat{\mathbf{r}}'(\mathbf{x}'_n)$$

$$= F_r(\mathbf{x}_n, \theta_1, \mathbf{Y}) \hat{\mathbf{r}}(\mathbf{x}_n),$$

due to translational motion induced by the radial component of the force \mathbf{F}' at \mathbf{x}'_n .

In the common reference frame, the following system of ODEs holds after unbinding (using the definition of \mathbf{x}'_n):

$$\beta_{\text{ECM}} \dot{\mathbf{x}} = F'_r(\mathbf{x}'_n, \theta_1, \mathbf{Y}) \hat{\mathbf{r}}'(\mathbf{x}'_n)$$

$$\beta_{\text{cell}} \dot{\mathbf{x}}'_n = \beta_{\text{cell}} \dot{\mathbf{x}} + \mathbf{F}'(\mathbf{x}'_n, \theta_1, \mathbf{Y})$$

$$\beta_{\text{rot}} \dot{\theta}_1 = \|\mathbf{x}'_n - \mathbf{x}\| F'_\phi(\mathbf{x}'_n, \theta_1, \mathbf{Y}),$$

which is equivalent to Equation (5). Using the common reference frame becomes even less convenient when formulating and analysing our stochastic process of cell motility. Moreover, our approach in the main text does not contradict the formulation with the single reference frame, and is equivalent to it.

Appendix B. Parameter Assessment

The values of all parameters have been summarized in Table A1. Below we provide the justification. Note that the length of myosin mini-filaments is $\sim 0.3 \mu\text{m}$ [75] and the interfilament distance is $\sim 1 \mu\text{m}$ in an uncontracted fibre [76]. Assuming vanishing interfilament distance (see Figure 2 for illustration and [40] for a review on actomyosin contraction mechanism), then the proportion of the minifilaments to the initial, uncontracted SF length is $\frac{0.3}{1+0.3} = 0.23$. Kassianidou et al. [42] showed that the retraction length scales linearly with the initial length. If the interfilament distance vanishes, the front myosin motor cannot perform a power stroke and step forward, which renders the single motor and the entire minifilament unable to apply contractile stress. Therefore, taking the initial length to be $\sim R_{\text{cell}}$, I estimate the critical length $L_c = 0.2R_{\text{cell}}$. Interestingly, Deguchi et al. [45] found that stress fibres contract, on average, to 20% of their original length. As stress fibres generally span more than half of a cell, and since it was found that there is a preexisting strain [45] in them, I estimate $L_0 = 1.1R_{\text{cell}}$.

Taking $R_{\text{cell}} = 25 \mu\text{m}$, and assuming a SF has at rest the length of R_{cell} , I can estimate the number of myosin minifilaments in a fibre to be $25 \mu\text{m} / 1.3 \mu\text{m} \approx 20$. It was estimated in [77] that there are 10–30 myosin motors in each minifilament. As each motor produces a force of $2 - 10 \text{ pN}$ [40,78,79], I then estimate $T_i = 4 \text{ nN}$. Balaban et al. [61] found that focal adhesions apply a constant stress of $\sim 5.5 \text{ nN}/\mu\text{m}^2$ over an area of $\sim 1 \mu\text{m}^2$ on an elastic substrate. Thus, I take $F_b = 5.5 \text{ nN}$. Assuming a preexisting strain was 0.1 when these measurements were taken, and since $T_i = 4 \text{ nN}$, I then estimate the one dimensional Young's modulus $EA = 15 \text{ nN}$.

Using Stokes' Law for drag in the low Reynolds number regime, the drag coefficient β_{ECM} can be estimated as:

$$\beta_{\text{ECM}} = 6\pi\eta_{\text{ECM}}R_{\text{cell}},$$

where η_{ECM} is the dynamic viscosity of the environment. Assuming that the viscosity η_{ECM} is higher than that of water, and taking into account that the contact between cell surface and the substrate increase the effective friction, I estimate $\beta_{\text{ECM}} \approx 10 - 10^3 \frac{\text{N}\cdot\text{s}}{\text{m}^2} \times R_{\text{cell}}$. Similarly, due to the low Reynolds number, the rotational drag coefficient β_{rot} is given by:

$$\beta_{\text{rot}} = 8\pi\eta_{\text{ECM}}R_{\text{cell}}^3 \approx 10 - 10^3 \frac{\text{N}\cdot\text{s}}{\text{m}^2} \times R_{\text{cell}}^3.$$

In order to obtain estimates for the drag coefficient β_{cell} one needs to have an estimate of the cytoplasm viscosity. Assessing the effective cytoplasmic viscosity of migrating cells is a challenging task, since the viscoelastic properties of the cytoskeleton (which, among other things, consists of polymer networks) are highly dynamic due to constant remodelling and spatiotemporal mediation of the rheology by various signaling pathways. Particularly, the actin network bundle size and cross-linkers influence the viscoelastic properties [80]. Furthermore, the effective viscosity experienced by an experimental probe (or a protein) in polymer solutions depends not only on the type of material properties of the fluid, but also on the size of a probe [81]. Using a small molecule as a probe, the cytoplasm viscosity was found to be $\simeq 2 - 3 \times 10^{-4} \text{ Pa}\cdot\text{s}$ [82]. With larger probes, the viscosity was found to be $\simeq 2 - 4 \times 10^{-2} \text{ Pa}\cdot\text{s}$ [81] and $\simeq 5 \times 10^{-2} \text{ Pa}\cdot\text{s}$ [83]. Assuming that the body being dragged in the cell is the nucleus with spherical, constant shape and radius R_{nucleus} , I estimate:

$$\beta_{\text{cell}} = 6\pi\eta_{\text{cell}}R_{\text{nucleus}} \approx 10 - 10^2 \frac{\text{N}\cdot\text{s}}{\text{m}^2} \times R_{\text{nucleus}},$$

where η_{cell} is the cytoplasm viscosity. The assumption that the nucleus has constant shape reflects the fact that it is significantly stiffer compared to the cytoplasm [84].

Table A1. Parameters used for simulation and their relative size with respect to spatial, temporal and force scales. See Section 2.3 for details.

| Parameter | Value | Value | Parameter | Value | Value |
|---------------|----------------------|-------|----------------|---|-------|
| T_i | 4 nN | 0.72 | R_{cell} | 25 μm | 1 |
| EA | 15 nN | 2.72 | L_0 | 27.5 μm | 1.1 |
| F_b | 5.5 nN | 1 | L_c | 5 μm | 0.2 |
| k_{off}^0 | 0.05 s^{-1} | 1 | β_{rot} | $1.56 \times 10^{-11} \text{N} \cdot \text{s} \cdot \text{m}$ | 5.68 |
| k_{on}^0 | 0.01 s^{-1} | 0.2 | β_{ECM} | $5 \times 10^{-4} \frac{\text{N} \cdot \text{s}}{\text{m}}$ | 0.11 |
| $R_{nucleus}$ | 5 μm | 0.2 | β_{cell} | $5 \times 10^{-3} \frac{\text{N} \cdot \text{s}}{\text{m}}$ | 1.14 |

Note that a focal adhesion is a cluster of transmembrane receptors (integrins) linking the substrate with the cytoskeleton, which is always under tension. The cluster also includes adapter proteins, which interlinks these receptors with the cytoskeleton (see e.g., reviews [85,86]). Thus, if there is no load on a focal adhesion, then, since the cytoskeleton is always under tension, such a focal adhesion can be treated as a complex of independent bonds to the substrate without a link to SF. In the absence of a load, the average cluster lifetime T_{life} is given by [87]:

$$T_{life} = \frac{1}{k_0^1 + k_{on}^1} \left[H_N + \sum_{n=1}^N \left(\frac{k_{on}^1}{k_0^1} \right)^n \frac{1}{n} \binom{N}{n} \right],$$

where N is the number of bonds in a cluster, H_N is the N th harmonic number, k_0^1 and k_{on}^1 are, respectively, unbinding and binding rates of integrins under no load. Note that in the absence of a load, (re-)binding of individual integrins is an independent event, which bears no relation to the FA, since tension is required for an FA to form and sustain itself. I then estimate:

$$k_{off}^0 = 1/T_{life}|_{k_{on}^1=0} = k_0^1/H_N.$$

Li et al. [88] found that $k_0^1 = 0.012 \text{ s}^{-1}$ for $\alpha_5\beta_1$ -integrin binding to fibronectin. For $N = 10^3 - 10^4$ I estimate that $k_{off}^0 = 0.05 \text{ s}^{-1} - 0.1 \text{ s}^{-1}$.

The rationale for simulating $M = 8, 16, 32$ FAs is the following. Note that the number of cell-substrate adhesions is higher than the number of focal adhesions chosen for the simulations. However, not all adhesions are directly involved in translocating the cell body, during which large traction forces are applied to the substrate through focal adhesions (which are fewer in number than immature, less stable focal complexes/points and nascent adhesions). Moreover, detachment of focal adhesions that leads to translocation, is primarily the result of contractile tension applied by ventral stress fibres, as opposed to transverse arcs and dorsal stress fibres [89]. The latter two have primarily structural role, while the former is fundamental to rear retraction [89,90]. Thus, the number of focal adhesions that are directly involved in cell body translocation is controlled by the number of the associated ventral stress fibres, which are also the most significant source of traction force applied to the substrate due to large tension within them [62,89]. Although reports of ventral stress fibre numbers are elusive, visual inspection of the fluorescence images in, for example, [62,91,92] (or any other appropriate study) suggests that simulations with the chosen number of (ventral) fibres (and focal adhesions) are realistic. Moreover, diameter of focal adhesions $d \sim 1 - 5 \mu\text{m}$ [39]. Assuming that the separation between focal adhesions is comparable to their size, and taking the cell radius to be $R_{cell} = 25 \mu\text{m}$ (as in our simulations), we see that the upper range of possible number of adhesions on the cell circumference is $2\pi R_{cell}/2d \approx 16 - 80$. I reiterate that this number is an estimate of focal

adhesions attached to ventral stress fibres, and it underestimates the total number of focal adhesions that a cell employs, since significant number of them are attached to other types of stress fibres and may also be present within the cell body and not on its periphery. I performed simulations with $M = 64$ focal adhesions and did not find any added insight.

The values of γ_1, γ_2 and ϵ , mentioned in Section 5.2.2, can be found as follows:

Suppose $F \leq F_b$. Then,

$$\gamma_1 = -\frac{F_b}{F - F_1^*} \log \left(\frac{k_{off}^0 e + k_{on}^0}{k_{force}(F) - k_{on}^0 + \epsilon} - 1 \right).$$

Since $k_{force}(0) = k_{on}^0$ and $k_{force}(F_b) = k_{off}^0 e$, then:

$$\begin{aligned} \gamma_1 &= \frac{F_b}{F_1^*} \log \left(\frac{k_{off}^0 e + k_{on}^0}{\epsilon} - 1 \right) \\ \gamma_1 &= -\frac{F_b}{F_b - F_1^*} \log \left(\frac{k_{off}^0 e + k_{on}^0}{k_{off}^0 e - k_{on}^0 + \epsilon} - 1 \right). \end{aligned}$$

It follows that ϵ is given as the solution of the following Equation:

$$\frac{F_b}{F_1^*} \log \left(\frac{k_{off}^0 e + k_{on}^0}{\epsilon} - 1 \right) + \frac{F_b}{F_b - F_1^*} \log \left(\frac{k_{off}^0 e + k_{on}^0}{k_{off}^0 e - k_{on}^0 + \epsilon} - 1 \right) = 0.$$

Similarly, since $k_{force}(F_b) = k_{off}^0 e$, I find:

$$\gamma_2 = \frac{F_b}{F_b - F_2^*} \log \left(\frac{k_{off}^0 e + k_{on}^0}{k_{off}^0 e - k_{on}^0} - 1 \right).$$

The values of γ_1, γ_2 , and ϵ are fixed for a value of F_b .

Appendix C. Data Analysis

Given that the time interval $[0, t_{end}]$ is divided into n_{time} subintervals of equal length Δt and given the positions $\mathbf{x}^i(t_j)$ of cell i at the time points $t_j := j\Delta t, j = 0, \dots, n_{time}$, the mean-squared displacement $msd_i(t_j)$ of cell $i \in \{1, \dots, n_{cells}\}$ over a time interval of length t_j is given by:

$$msd_i(t_j) := \frac{1}{n_{time} - j} \sum_{k=1}^{n_{time}-j} \|\mathbf{x}^i(t_{j+k}) - \mathbf{x}^i(t_k)\|^2, \quad (A1)$$

where $j = 1, \dots, n_{time} - 1$ and n_{cells} is the total number of cells. Then, the mean-squared displacement $msd(t)$ of an ensemble of cells over time interval of length t_j is defined by:

$$msd(t) := \frac{1}{n_{cells}} \sum_{i=1}^{n_{cells}} msd_i(t_j). \quad (A2)$$

Remark A1. In general, the (time-averaged) mean-squared displacement $\langle d^2(t, T) \rangle$ of a particle trajectory $\mathbf{x}(t)$ at the time t , time endpoint T is formally defined as:

$$\langle d^2(t, T) \rangle = \frac{1}{T - t} \int_0^{T-t} \|\mathbf{x}(s + t) - \mathbf{x}(t)\|^2 ds. \quad (A3)$$

For an ergodic process, we have:

$$\lim_{T \rightarrow \infty} \langle d^2(t, T) \rangle = \langle \mathbf{x}^2(t) \rangle,$$

where $\langle \mathbf{x}^2(t) \rangle$ is formally defined as:

$$\langle \mathbf{x}^2(t) \rangle = \int \mathbf{x}^2 P_t(d\mathbf{x}),$$

and $P_t(d\mathbf{x})$ is the probability measure of the underlying stochastic process at time t . That is, for an ergodic process, and for sufficiently long times, the time average equals the phase space average. However, our cell motility process need not be ergodic and hence, using a quadrature to evaluate the integral in Equation (A3), I obtain time average displacement in Equation (A1). To smooth out trajectory-to-trajectory fluctuations, I then average the displacements over all trajectories in Equation (A2).

For a diffusive motion one expects that $msd(t) \sim t^{\beta(t)}$ with $\beta(t) \approx 1$, while for a ballistic motion $\beta(t) \approx 2$. Since $msd(0) = 0$, I can estimate the exponent $\beta(t)$ for $t \in [\Delta t, t_{end} - \Delta t]$ from the simulated data as:

$$\beta(t) = \frac{d \ln msd(t)}{d \ln t}.$$

Although averaging reduces fluctuations, it does not eliminate them completely. Thus, computing the derivative above will yield a result that may oscillate wildly, which we want to avoid. Then, in order to investigate how β varies with time, I define the time average $\beta_{av}(t)$ over the interval $[\Delta t, t]$ as:

$$\beta_{av}(t) := \frac{1}{t - \Delta t} \int_{\Delta t}^t \beta(s) ds = \frac{1}{t - \Delta t} \left(s \ln msd(s) \Big|_{\Delta t}^t - \int_{\Delta t}^t \ln msd(s) ds \right),$$

where $t \in [2\Delta t, t_{end} - \Delta t]$, and I used integration by substitution and by parts. Then, $\bar{\beta} := \beta_{av}(t_{end} - \Delta t)$ estimates the time scaling of msd over the whole time interval. To assess how well $\bar{\beta}$ reflects the scaling of msd , I define the following function $\widehat{msd}(t) := \beta_0 t^{\bar{\beta}}$, where β_0 is found by minimizing the square error:

$$\min_{\beta_0} \frac{1}{2} \sum_{j=1}^{n_{time}-1} \left(\beta_0 t_j^{\bar{\beta}} - msd(t_j) \right)^2 \Rightarrow$$

$$\beta_0 = \frac{\sum_{j=1}^{n_{time}-1} msd(t_j) t_j^{\bar{\beta}}}{\sum_{j=1}^{n_{time}-1} t_j^{2\bar{\beta}}}.$$

Letting $\bar{\beta} = \beta_{av}(t - \Delta t)$ to assess time scaling of $msd \sim t^{\beta(t)}$ is more accurate than the standard methods used for Brownian motion, since it also takes into account time dependence of the exponent. In addition, our stochastic model has no Gaussian component. I refer to Section 6 for comparisons between msd and \widehat{msd} , which show that the former well approximates the latter. The sample size used to compute β_{av} and β_0 in Section 6 was $n_{cell} n_{time} = 2.8 \times 10^5$.

Note that because binding events can occur, a cell need not to have moved between the two time points t_j and t_{j+1} . Thus, the speed between the consecutive time points may be zero for many time points, which would give an inaccurate statistical assessment of cell speeds. In order to estimate the speeds of a cell i I use the following procedure:

First, I find l_i , given by:

$$l_i := \min \left\{ l \in \mathbb{N} : \mathbf{x}^i(t_{l+k}) \neq \mathbf{x}^i(t_k), 0 \leq k < n_{time}, l+k \leq n_{time} \right\}.$$

Then I find the set of speeds S_i as:

$$S_i := \left\{ s \in \mathbb{R}^+ : s = \frac{\|\mathbf{x}^i(t_{(k+1)l_i}) - \mathbf{x}^i(t_{kl_i})\|}{l_i \Delta t}, k \in \mathbb{N}, (k+1)l_i \leq n_{time} \right\}.$$

This simply means that to compute speeds I only use a (minimal) time interval, such that a cell i is guaranteed to change its position. The total set of speeds for n_{cells} is $S := \cup_{i=1}^{n_{cells}} S_i$. The average speed s_{av} is then defined as arithmetic average:

$$s_{av} := \frac{1}{|S|} \sum_{s \in S} s.$$

The sample sizes used to compute s_{av} in Section 6 were on the order of 2×10^5 . It is less than $n_{cells}n_{time}$, since non-zero speeds have been excluded.

The set of normalized velocities V_i (or, alternatively, displacements) of cell i is given by:

$$V_i := \left\{ \mathbf{v} \in \mathbb{R}^2 : \mathbf{v} = \frac{\mathbf{x}^i(t_{(k+1)l_i}) - \mathbf{x}^i(t_{kl_i})}{\|\mathbf{x}^i(t_{(k+1)l_i}) - \mathbf{x}^i(t_{kl_i})\|}, k \in \mathbb{N}, (k+1)l_i \leq n_{time} \right\},$$

and the total set of normalized velocities V is given by $V := \cup_{i=1}^{n_{cells}} V_i$.

The directionality ratio $r_i(t_j)$ of cell i over a time interval of length t_j is given by:

$$r_i(t_j) := \frac{\sum_{k=1}^j \|\mathbf{x}^i(t_k) - \mathbf{x}^i(t_{k-1})\|}{\|\mathbf{x}^i(t_j) - \mathbf{x}^i(t_0)\|}.$$

The population and the time averages of the directionality ratio are given by, respectively:

$$r(t_j) = \frac{1}{n_{cell}} \sum_{i=1}^{n_{cell}} r_i(t_j)$$

$$\bar{r} = \frac{1}{n_{time}} \sum_{j=1}^{n_{time}} r(t_j).$$

The sample size used to compute \bar{r} in Section 6 was $n_{cell}n_{time} = 2.8 \times 10^5$.

Velocity autocorrelation $v_{ac}^i(t_j)$ of cell i over a time interval of length t_j is given by:

$$v_{ac}^i(t_j) := \frac{1}{n_{time} - j} \sum_{k=1}^{n_{time}-j} \frac{\mathbf{v}^i(t_{j+k}) \cdot \mathbf{v}^i(t_k)}{\|\mathbf{v}^i(t_{j+k})\| \|\mathbf{v}^i(t_k)\|},$$

where $j = 1, \dots, n_{time} - 1$ and $\mathbf{v}^i(t_k) = (\mathbf{x}^i(t_k) - \mathbf{x}^i(t_{k-1})) / \Delta t$. Velocity autocorrelation of the population $v_{ac}(t)$ is simply the arithmetic average of each cell's velocity autocorrelation. To compute v_{ac} I used the time step of 12 min, whereas for all other quantities involving time dependence (e.g., *msd*) I used the time step of 0.12 min.

Defining the guidance parameter $G \in [0, 1]$ similarly as in [32]:

$$G := \frac{1}{|\Theta|} \sum_{\theta \in \Theta} g(\theta),$$

where $\Theta := \cup_{i=1}^{n_{cells}} \Theta_i$. The set Θ_i of angles between a displacement vector of cell i and the ECM fibres is defined by

$$\Theta_i := \left\{ \theta \in \left[-\frac{\pi}{2}, \frac{\pi}{2}\right] : \theta = \arcsin \left(\frac{x_2^i(t_{(k+1)l_i}) - x_2^i(t_{kl_i})}{\|\mathbf{x}^i(t_{(k+1)l_i}) - \mathbf{x}^i(t_{kl_i})\|} \right), k \in \mathbb{N}, (k+1)l_i \leq n_{time} \right\},$$

where x_2^i is the y -component of \mathbf{x}^i . The function $g : [-\frac{\pi}{2}, \frac{\pi}{2}] \rightarrow \{0, 1\}$ is given by

$$g(\theta) = \begin{cases} 1, & \text{if } |\theta| \leq \pi/4 \\ 0, & \text{else} \end{cases}.$$

Thus, G increases when displacements are aligned with the horizontal axis.

Data Variability

To assess the variability of speeds, the interquartile ranges have been reported along with average speeds (see Tables 1–4). We see that the ranges are similar to the means. Together with histogram plots of speeds, we can conclude that most of the values fall in the middle 50% of data set. That is, very high or low speeds are relatively rare.

Other parameters computed from the data depend on time and in order to assess their variability one can observe the corresponding plots:

- Figures 7, 9a–c and 12a–c show plots of directionality ratio r , where we can see the variations (i.e., oscillations) are rather small.
- Figures 10g–i and 19d–f show variations of the exponent β_{av} in time, where we also observe relatively smooth graphs.

In both of these cases, the plots are smooth due to abundance of sample size and in part due to their definitions (see above), which smooths out oscillations. As a result of how well the time averaged parameters fit the simulated mean-squared displacement data (Figures 6d–f, 8d–f and 10d–f), lack of oscillations in parameter values in time, abundance of sample size, I deemed that further statistical investigations of time-series to be unnecessary.

Appendix D. Simulation of the PDMP

In order to compute the trajectories of the cell motility process, the following Algorithm A1 is used:

Algorithm A1 Simulation of the PDMP.

1. Set $(v_0, \mathbf{X}_0) \in A \times \Gamma$ and $t = T_0 = 0$
2. For $k = 0, 1, \dots$
Generate interarrival time $\Delta_k = T_{k+1} - T_k$, whose distribution function is given by:

$$\mathbb{P}(\Delta_k \leq \tau) = 1 - \exp \left(- \int_t^{t+\tau} a_0(v_t, \phi_v(s, \mathbf{X}_t)) ds \right) \quad (\text{A4})$$

Compute $\mathbf{X}_{t+s^-} := \phi_v(s, \mathbf{X}_t)$

Set $t = T_{k+1} = T_k + \Delta_k$

Generate $(v_t, \mathbf{X}_t) \sim Q(\cdot; (v_{t^-}, \mathbf{X}_{t^-}))$

To generate the interarrival time Δ_k , we need to solve for τ in the following Equation:

$$f(\tau) := \int_t^{t+\tau} a_0(v_t, \phi_v(s, \mathbf{X}_t)) ds + \ln(1 - u) = 0, \quad (\text{A5})$$

where u is uniformly distributed on the interval $(0, 1)$.

Notice that the evaluation of the integral by a quadrature rule requires computing the solution $\mathbf{X}_{t+s} = \phi_{v_t}(s, \mathbf{X}_t)$ up to time s , where s is a quadrature point. Moreover, using an iterative method to solve Equation (A5) requires computing the integral at each iteration. Therefore, it is imperative to devise an efficient method to sample from distribution Equation (A4). In the following, I propose a general method to generate the next event time.

Appendix D.1. Simulation of the Next Event Time

Let $T_k \leq t < T_{k+1}$ and let $\mathbf{G}(\cdot; h) : \Gamma \rightarrow \Gamma$ represent a numerical method to solve the ODE system

$$\frac{d}{dt}\mathbf{X}_t = \mathbf{H}_{v_t}(\mathbf{X}_t)$$

for one time step h . That is, $\mathbf{X}_{t+h} = \mathbf{G}(\mathbf{X}_t; h)$ is the numerical solution of the above ODE system at time $t + h$.

Let $[T_k, T_{k+1})^2 \ni (s', t') \mapsto A_0(t', s') := \int_{s'}^{t'} a_0(v_t, \phi_{v_t}(u, \mathbf{X}_t)) du$ denote the integrated rate function.

The method to find the root τ of Equation (A5) is given in Algorithm A2. First, in steps (1–22), I find the upper bound τ_{max} by solving the ODE system for n steps with step size h and store the solution, the computed rate a_0 and the integrated rate A_0 at these time steps. Then, for any $\tau \leq \tau_{max}$ one can compute $A_0(t + \tau, t)$ upon using the stored value of A_0 at time $t + \tau_i$, where $i = \lfloor \frac{\tau}{h} \rfloor$ and $\tau_i = ih$:

$$\begin{aligned} A_0(t + \tau, t) &= \int_t^{t+\tau} a_0(v_t, \phi_{v_t}(s, \mathbf{X}_t)) ds \\ &= \int_t^{t+\tau_i} a_0(v_t, \mathbf{X}_{t+s}) ds + \int_{t+\tau_i}^{t+\tau_i+\tau-\tau_i} a_0(v_t, \phi_{v_t}(s, \mathbf{X}_t)) ds \\ &= A_0(t + \tau_i, t) + \int_{t+\tau_i}^{t+\tau_i+h_i} a_0(v_t, \phi_{v_t}(s, \mathbf{X}_t)) ds. \end{aligned}$$

To compute the last integral in the expression above, we interpolate the integrand using the stored values $a_0(v_t, \mathbf{X}_{t+\tau_i})$ and $a_0(v_t, \mathbf{X}_{t+\tau_{i+1}})$. Let

$$I(a_0(v_t, \mathbf{X}_{t+\tau_i}), a_0(v_t, \mathbf{X}_{t+\tau_{i+1}}); h_i, h) := \int_{t+\tau_i}^{t+\tau_i+h_i} a_0(v_t, \phi_{v_t}(s, \mathbf{X}_t))$$

denote the approximation of the integral using interpolated integrand. We can use the following interpolation methods for $t + \tau_i < s < t + \tau_{i+1}$:

1. Piecewise constant

Forward: $a_0(v_t, \phi_{v_t}(s, \mathbf{X}_t)) = a_0(v_t, \phi_{v_t}(\tau_i, \mathbf{X}_t)) = a_0(v_t, \mathbf{X}_{t+\tau_i})$.

$$I(a_0(v_t, \mathbf{X}_{t+\tau_i}), a_0(v_t, \mathbf{X}_{t+\tau_{i+1}}); h_i, h) = h_i a_0(v_t, \mathbf{X}_{t+\tau_i}). \quad (\text{A6})$$

Backward: $a_0(v_t, \phi_{v_t}(s, \mathbf{X}_t)) = a_0(v_t, \phi_{v_t}(\tau_{i+1}, \mathbf{X}_t)) = a_0(v_t, \mathbf{X}_{t+\tau_{i+1}})$

$$I(a_0(v_t, \mathbf{X}_{t+\tau_i}), a_0(v_t, \mathbf{X}_{t+\tau_{i+1}}); h_i, h) = h_i a_0(v_t, \mathbf{X}_{t+\tau_{i+1}}). \quad (\text{A7})$$

2. Average: $a_0(v_t, \phi_{v_t}(s, \mathbf{X}_t)) = \frac{1}{2} (a_0(v_t, \mathbf{X}_{t+\tau_i}) + a_0(v_t, \mathbf{X}_{t+\tau_{i+1}}))$.

$$I(a_0(v_t, \mathbf{X}_{t+\tau_i}), a_0(v_t, \mathbf{X}_{t+\tau_{i+1}}); h_i, h) = \frac{1}{2} h_i (a_0(v_t, \mathbf{X}_{t+\tau_i}) + a_0(v_t, \mathbf{X}_{t+\tau_{i+1}})). \quad (\text{A8})$$

3. Piecewise linear:

$$\begin{aligned}
 a_0(v_t, \phi_{v_t}(s, \mathbf{X}_t)) &= (s - t - \tau_i) \frac{a_0(v_t, \mathbf{X}_{t+\tau_{i+1}}) - a_0(v_t, \mathbf{X}_{t+\tau_i})}{h} + a_0(v_t, \mathbf{X}_{t+\tau_i}). \\
 I(a_0(v_t, \mathbf{X}_{t+\tau_i}), a_0(v_t, \mathbf{X}_{t+\tau_{i+1}}); h_i, h) &= h_i a_0(v_t, \mathbf{X}_{t+\tau_i}) \left(1 - \frac{h_i}{h}\right) + \frac{h_i^2}{2h} a_0(v_t, \mathbf{X}_{t+\tau_{i+1}}). \quad (\text{A9})
 \end{aligned}$$

Thus, $f(\tau)$ can be evaluated using Equations (A6)–(A9):

$$f(\tau) = A_0(t + \tau_i, t) + I(a_0(v_t, \mathbf{X}_{t+\tau_i}), a_0(v_t, \mathbf{X}_{t+\tau_{i+1}}); h_i, h) + \ln(1 - u).$$

Algorithm A2 Event time computation.

```

1: procedure INITIALIZATION
2:   Input: Time  $t = T_k$ ;  $(v_t, \mathbf{X}_t)$ ; time step  $h$  and ODE method  $\mathbf{G}$ ;  $n, m \in \mathbb{N}$ .
3:   Set  $s_0 := 0, n_0 := 0$ , create  $List_{a_0}$ ,  $List_{A_0}$ , and  $List_{\mathbf{X}}$ .
4:   Append  $List_{a_0} \leftarrow a_0(v_t, \mathbf{X}_t)$ ,  $List_{A_0} \leftarrow 0$ ,  $List_{\mathbf{X}} \leftarrow \mathbf{X}_t$ .
5:   Set  $\tau_{max} := nh$ ,  $s_0 := n_0h$ .
6:   Set initial condition  $\mathbf{X}_s \leftarrow List_{\mathbf{X}}[last]$ .
7:   Set  $A_0^0 := List_{A_0}[last]$ .
8:   for  $i = 1$  to  $n$  do
9:      $s_i := t + s_0 + ih$ .
10:    Compute  $\mathbf{X}_{s_i} := \mathbf{G}(\mathbf{X}_s; h)$  and  $a_0(v_t, \mathbf{X}_{s_i})$ .
11:    Compute  $A_0(s_i; t + s_0)$  with quadrature points  $s_j, j = 0, \dots, i$ .
12:     $A_0(s_i; t) := A_0^0 + A_0(s_i; t + s_0)$ .
13:    Append  $List_{a_0} \leftarrow a_0(v_t, \mathbf{X}_{s_i})$ ,  $List_{A_0} \leftarrow A_0(s_i; t)$ ,  $List_{\mathbf{X}} \leftarrow \mathbf{X}_{s_i}$ .
14:  end for
15:  Generate  $u \sim U(0, 1)$ .
16:  if  $List_{A_0}[last] < -\ln(1 - u)$  then
17:     $n := n + m$ .
18:     $n_0 = n_0 + m$ .
19:    go to 5.
20:  end if
21:  Output:  $\tau_{max}$ ,  $List_{a_0}$ ,  $List_{A_0}$ , and  $List_{\mathbf{X}}$ .
22: end procedure
23: procedure EVALUATION OF  $f$ 
24:   Input:  $\tau$ ; time step  $h$ ;  $List_{a_0}$ ,  $List_{A_0}$ ; Integrated interpolation method  $I$ .
25:   Set  $i := \lfloor \frac{\tau}{h} \rfloor$  and  $h_i = \tau - ih$ .
26:   Output:  $f(\tau) = List_{A_0}[i] + I(List_{a_0}[i], List_{a_0}[i + 1]; h_i, h) + \ln(1 - u)$ 
27: end procedure
28: procedure EVENT TIME
29:   Find the root  $\tau$  of  $f(\tau) = 0$  using 23 and a root finding method.
30:    $i := \lfloor \frac{\tau}{h} \rfloor$ .
31:   Compute  $\mathbf{X}_{t+\tau} := \mathbf{G}(List_{\mathbf{X}}[i]; \tau - ih)$ .
32:   Output:  $\tau, \mathbf{X}_{t+\tau}$ 
33: end procedure

```

Using the interpolations above, one can now employ, for example, Newton's method to find the root of Equation (A5):

$$\tau_{l+1} = \tau_l - \frac{f(\tau_l)}{a_0(v_t, \phi_{v_t}(\tau_l, \mathbf{X}_t))},$$

or any other root-finding method (note that $a_0 > 0$).

Once the root is found, one simply advances the ODE system for one time step as described in Steps (28–33) of the Algorithm A2.

Note that one solves the ODE system for $n + 1 = \tau_{max}/h + 1$ steps and also solves for the interarrival time τ primarily by using a look-up table. Moreover, obtaining a relatively sharp upper bound τ_{max} does not yield a large computational overhead, since one simply can start the Algorithm A2 with a small n, m . Consequently, choosing an initial guess close to the sharp upper bound for Newton's method results in a faster convergence. In case of thinning methods (see [93] or [94] for adaptive method), after each rejection one needs to solve the ODE system for time period that is, on average, approximately the same as τ_{max} (in the best case scenarios for both methods, i.e., when the bound τ_{max} and the bound for the rate function in thinning methods are sharp). Of course, these arguments hold when the computational cost of solving the ODE system is relatively large.

Appendix D.2. Sampling from the Transition Measure

Given the time t of the next event and \mathbf{X}_t one needs to sample from the transition distribution $Q(\cdot, (v_{t-}, \mathbf{X}_{t-}))$. Recalling Section 3.2 and the proof of Proposition 5, in order to sample from the transition measure it is sufficient to simulate the index $j \in \{1, \dots, 2M\}$ of the next reaction, since the continuous component of the process does not jump. The discrete distribution of the next reaction index is given by Equation (18):

$$\mathbb{P}(j|\alpha_2(v_{t-}, \mathbf{X}_{t-})) = \frac{a_j(\alpha_2(v_{t-}, \mathbf{X}_{t-}))}{a_0(\alpha_2(v_{t-}, \mathbf{X}_{t-}))}.$$

To simulate from the discrete distribution one can use the fairly efficient Vose Alias Method [95].

References

1. Lauffenburger, D.A.; Horwitz, A.F. Cell migration: A physically integrated molecular process. *Cell* **1996**, *84*, 359–369. [\[CrossRef\]](#)
2. Abercrombie, M. The Croonian Lecture, 1978—The crawling movement of metazoan cells. *Proc. R. Soc. Lond. B Biol. Sci.* **1980**, *207*, 129–147.
3. Raftopoulou, M.; Hall, A. Cell migration: Rho GTPases lead the way. *Dev. Biol.* **2004**, *265*, 23–32. [\[CrossRef\]](#) [\[PubMed\]](#)
4. Ridley, A.J.; Schwartz, M.A.; Burridge, K.; Firtel, R.A.; Ginsberg, M.H.; Borisy, G.; Parsons, J.T.; Horwitz, A.R. Cell migration: Integrating signals from front to back. *Science* **2003**, *302*, 1704–1709. [\[CrossRef\]](#)
5. Holmes, W.R.; Edelstein-Keshet, L. A comparison of computational models for eukaryotic cell shape and motility. *PLoS Comput. Biol.* **2012**, *8*, e1002793. [\[CrossRef\]](#) [\[PubMed\]](#)
6. Ziebert, F.; Aranson, I.S. Computational approaches to substrate-based cell motility. *Npj Comput. Mater.* **2016**, *2*, 16019. [\[CrossRef\]](#)
7. Mogilner, A. Mathematics of cell motility: Have we got its number? *J. Math. Biol.* **2009**, *58*, 105. [\[CrossRef\]](#)
8. Camley, B.A.; Zhao, Y.; Li, B.; Levine, H.; Rappel, W.J. Crawling and turning in a minimal reaction-diffusion cell motility model: Coupling cell shape and biochemistry. *Phys. Rev. E* **2017**, *95*, 012401. [\[CrossRef\]](#)
9. Oelz, D.; Schmeiser, C. *How Do Cells Move? Mathematical Modeling of Cytoskeleton Dynamics and Cell Migration. Cell Mechanics: From Single Scale-Based Models to Multiscale Modeling*; Chapman and Hall: New York, NY, USA, 2010.
10. Manhart, A.; Oelz, D.; Schmeiser, C.; Sfakianakis, N. An extended Filament Based Lamellipodium Model produces various moving cell shapes in the presence of chemotactic signals. *J. Theor. Biol.* **2015**, *382*, 244–258. [\[CrossRef\]](#)
11. Preziosi, L.; Vitale, G. A multiphase model of tumor and tissue growth including cell adhesion and plastic reorganization. *Math. Model. Methods Appl. Sci.* **2011**, *21*, 1901–1932. [\[CrossRef\]](#)
12. Rubinstein, B.; Jacobson, K.; Mogilner, A. Multiscale Two-Dimensional Modeling of a Motile Simple-Shaped Cell. *Multiscale Model. Simul.* **2005**, *3*, 413–439. [\[CrossRef\]](#) [\[PubMed\]](#)

13. Shao, D.; Rappel, W.J.; Levine, H. Computational model for cell morphodynamics. *Phys. Rev. Lett.* **2010**, *105*, 108104. [[CrossRef](#)] [[PubMed](#)]
14. Copos, C.A.; Walcott, S.; del Álamo, J.C.; Bastounis, E.; Mogilner, A.; Guy, R.D. Mechanosensitive Adhesion Explains Stepping Motility in Amoeboid Cells. *Biophys. J.* **2017**, *112*, 2672–2682. [[CrossRef](#)] [[PubMed](#)]
15. Zhu, J.; Mogilner, A. Comparison of cell migration mechanical strategies in three-dimensional matrices: A computational study. *Interface Focus* **2016**, *6*, 20160040. [[CrossRef](#)]
16. Marée, A.F.; Jilkin, A.; Dawes, A.; Grieneisen, V.A.; Edelstein-Keshet, L. Polarization and movement of keratocytes: A multiscale modelling approach. *Bull. Math. Biol.* **2006**, *68*, 1169–1211. [[CrossRef](#)]
17. Marée, A.F.M.; Grieneisen, V.A.; Edelstein-Keshet, L. How Cells Integrate Complex Stimuli: The Effect of Feedback from Phosphoinositides and Cell Shape on Cell Polarization and Motility. *PLoS Comput. Biol.* **2012**, *8*, 1–20. [[CrossRef](#)]
18. Arriumerlou, C.; Meyer, T. A local coupling model and compass parameter for eukaryotic chemotaxis. *Dev. Cell* **2005**, *8*, 215–227. [[CrossRef](#)]
19. Dickinson, R.B.; Tranquillo, R.T. A stochastic model for adhesion-mediated cell random motility and haptotaxis. *J. Math. Biol.* **1993**, *31*, 563–600. [[CrossRef](#)]
20. Groh, A.; Louis, A.K. Stochastic modelling of biased cell migration and collagen matrix modification. *J. Math. Biol.* **2010**, *61*, 617–647. [[CrossRef](#)]
21. Satulovsky, J.; Lui, R.; Wang, Y.I. Exploring the control circuit of cell migration by mathematical modeling. *Biophys. J.* **2008**, *94*, 3671–3683. [[CrossRef](#)]
22. Tranquillo, R.T.; Lauffenburger, D.A.; Zigmond, S. A stochastic model for leukocyte random motility and chemotaxis based on receptor binding fluctuations. *J. Cell Biol.* **1988**, *106*, 303–309. [[CrossRef](#)] [[PubMed](#)]
23. Dieterich, P.; Klages, R.; Preuss, R.; Schwab, A. Anomalous dynamics of cell migration. *Proc. Natl. Acad. Sci. USA* **2008**, *105*, 459–463. [[CrossRef](#)] [[PubMed](#)]
24. Li, L.; Nørrelykke, S.F.; Cox, E.C. Persistent Cell Motion in the Absence of External Signals: A Search Strategy for Eukaryotic Cells. *PLoS ONE* **2008**, *3*, e2093. [[CrossRef](#)] [[PubMed](#)]
25. Selmecki, D.; Mosler, S.; Hagedorn, P.H.; Larsen, N.B.; Flyvbjerg, H. Cell Motility as Persistent Random Motion: Theories from Experiments. *Biophys. J.* **2005**, *89*, 912–931. [[CrossRef](#)] [[PubMed](#)]
26. Othmer, H.G.; Dunbar, S.R.; Alt, W. Models of dispersal in biological systems. *J. Math. Biol.* **1988**, *26*, 263–298. [[CrossRef](#)]
27. Engwer, C.; Hillen, T.; Knappitsch, M.; Surulescu, C. Glioma follow white matter tracts: A multiscale DTI-based model. *J. Math. Biol.* **2015**, *71*, 551–582. [[CrossRef](#)]
28. Kelkel, J.; Surulescu, C. A multiscale approach to cell migration in tissue networks. *Math. Model. Methods Appl. Sci.* **2012**, *22*, 1150017. [[CrossRef](#)]
29. Davis, M.H. Piecewise-deterministic Markov processes: A general class of non-diffusion stochastic models. *J. R. Stat. Soc. Ser. B Methodol.* **1984**, *46*, 353–388. [[CrossRef](#)]
30. Davis, M.H.A. *Markov Models and Optimization*; Chapman and Hall: New York, NY, USA, 1993.
31. Liu, Y.J.; Le Berre, M.; Lautenschlaeger, F.; Maiuri, P.; Callan-Jones, A.; Heuzé, M.; Takaki, T.; Voituriez, R.; Piel, M. Confinement and low adhesion induce fast amoeboid migration of slow mesenchymal cells. *Cell* **2015**, *160*, 659–672. [[CrossRef](#)]
32. Ramirez-San Juan, G.R.; Oakes, P.W.; Gardel, M.L. Contact guidance requires spatial control of leading-edge protrusion. *Mol. Biol. Cell* **2017**, *28*, 1043–1053. [[CrossRef](#)]
33. Verkhovsky, A.B.; Svitkina, T.M.; Borisy, G.G. Self-polarization and directional motility of cytoplasm. *Curr. Biol.* **1999**, *9*, 11–S1. [[CrossRef](#)]
34. Yam, P.T.; Wilson, C.A.; Ji, L.; Hebert, B.; Barnhart, E.L.; Dye, N.A.; Wiseman, P.W.; Danuser, G.; Theriot, J.A. Actin-myosin network reorganization breaks symmetry at the cell rear to spontaneously initiate polarized cell motility. *J. Cell Biol.* **2007**, *178*, 1207–1221. [[CrossRef](#)] [[PubMed](#)]
35. Uatay, A. A mathematical model of contact inhibition of locomotion: Coupling contractility and focal adhesions. *arXiv* **2019**, arXiv:1901.02386.
36. Uatay, A. Multiscale Mathematical Modeling of Cell Migration: From Single Cells to Populations. Ph.D. Thesis, Technische Universität Kaiserslautern, Kaiserslautern, Germany, 2019.
37. Bellomo, N.; Knopoff, D.; Soler, J. On the difficult interplay between life, “complexity”, and mathematical sciences. *Math. Model. Methods Appl. Sci.* **2013**, *23*, 1861–1913. [[CrossRef](#)]

38. Knopoff, D.A.; Nieto, J.; Urrutia, L. Numerical simulation of a multiscale cell motility model based on the kinetic theory of active particles. *Symmetry* **2019**, *11*, 1003. [[CrossRef](#)]
39. Gardel, M.L.; Schneider, I.C.; Aratyn-Schaus, Y.; Waterman, C.M. Mechanical integration of actin and adhesion dynamics in cell migration. *Annu. Rev. Cell Dev. Biol.* **2010**, *26*, 315–333. [[CrossRef](#)]
40. Murrell, M.; Oakes, P.W.; Lenz, M.; Gardel, M.L. Forcing cells into shape: The mechanics of actomyosin contractility. *Nat. Rev. Mol. Cell Biol.* **2015**, *16*, 486–498. [[CrossRef](#)]
41. Guthardt Torres, P.; Bischofs, I.B.; Schwarz, U.S. Contractile network models for adherent cells. *Phys. Rev. Lett. E* **2012**, *85*, 011913. [[CrossRef](#)]
42. Kassianidou, E.; Brand, A.C.; Schwarz, U.S.; Kumar, S. Geometry and network connectivity govern the mechanics of stress fibers. *Proc. Natl. Acad. Sci. USA* **2017**, *114*, 2622–2627. [[CrossRef](#)]
43. Kumar, S.; Maxwell, I.Z.; Heisterkamp, A.; Polte, T.R.; Lele, T.P.; Salanga, M.; Mazur, E.; Ingber, D.E. Viscoelastic Retraction of Single Living Stress Fibers and Its Impact on Cell Shape, Cytoskeletal Organization, and Extracellular Matrix Mechanics. *Biophys. J.* **2006**, *90*, 3762–3773. [[CrossRef](#)]
44. Russell, R.J.; Xia, S.L.; Dickinson, R.B.; Lele, T.P. Sarcomere mechanics in capillary endothelial cells. *Biophys. J.* **2009**, *97*, 1578–1585. [[CrossRef](#)] [[PubMed](#)]
45. Deguchi, S.; Ohashi, T.; Sato, M. Tensile properties of single stress fiber isolated from cultured vascular smooth muscle cells. *J. Biomech.* **2006**, *39*, 2603–2610. [[CrossRef](#)] [[PubMed](#)]
46. Möhl, C.; Kirchgessner, N.; Schäfer, C.; Hoffmann, B.; Merkel, R. Quantitative mapping of averaged focal adhesion dynamics in migrating cells by shape normalization. *J. Cell Sci.* **2012**, *125*, 155–165. [[CrossRef](#)] [[PubMed](#)]
47. Schwarz, U.S.; Gardel, M.L. United we stand integrating the actin cytoskeleton and cell matrix adhesions in cellular mechanotransduction. *J. Cell Sci.* **2012**, *125*, 3051–3060. [[CrossRef](#)] [[PubMed](#)]
48. Paul, R.; Heil, P.; Spatz, J.P.; Schwarz, U.S. Propagation of mechanical stress through the actin cytoskeleton toward focal adhesions: Model and experiment. *Biophys. J.* **2008**, *94*, 1470–1482. [[CrossRef](#)]
49. Oakes, P.W.; Wagner, E.; Brand, C.A.; Probst, D.; Linke, M.; Schwarz, U.S.; Glotzer, M.; Gardel, M.L. Optogenetic Control of RhoA Reveals Zyxin-mediated Elasticity of Stress Fibers. *Nat. Commun.* **2017**, *8*, 15817. [[CrossRef](#)]
50. Gillespie, D.T. A rigorous derivation of the chemical master Equation. *Phys. A Stat. Mech. Its Appl.* **1992**, *188*, 404–425. [[CrossRef](#)]
51. Ananthakrishnan, R.; Ehrlicher, A. The Forces Behind Cell Movement. *Int. J. Biol. Sci.* **2007**, *3*, 303–317. [[CrossRef](#)]
52. Cramer, L.P. Forming the cell rear first: Breaking cell symmetry to trigger directed cell migration. *Nat. Cell Biol.* **2010**, *12*, 628–632. [[CrossRef](#)]
53. Bell, G.I. Models for the specific adhesion of cells to cells. *Science* **1978**, *200*, 618–627. [[CrossRef](#)]
54. Ridley, A.J. Rho GTPases and cell migration. *J. Cell Sci.* **2001**, *114*, 2713–2722. [[PubMed](#)]
55. Giverso, C.; Preziosi, L. Mechanical perspective on chemotaxis. *Phys. Rev. E* **2018**, *98*, 062402. [[CrossRef](#)]
56. Holmes, W.R.; Lin, B.; Levchenko, A.; Edelstein-Keshet, L. Modelling cell polarization driven by synthetic spatially graded Rac activation. *PLoS Comput. Biol.* **2012**, *8*, e1002366. [[CrossRef](#)] [[PubMed](#)]
57. Narang, A. Spontaneous polarization in eukaryotic gradient sensing: A mathematical model based on mutual inhibition of frontness and backness pathways. *J. Theor. Biol.* **2006**, *240*, 538–553. [[CrossRef](#)]
58. Choi, C.K.; Vicente-Manzanares, M.; Zareno, J.; Whitmore, L.A.; Mogilner, A.; Horwitz, A.R. Actin and α -actinin orchestrate the assembly and maturation of nascent adhesions in a myosin II motor-independent manner. *Nat. Cell Biol.* **2008**, *10*, 1039–1050. [[CrossRef](#)]
59. Stricker, J.; Aratyn-Schaus, Y.; Oakes, P.W.; Gardel, M.L. Spatiotemporal constraints on the force-dependent growth of focal adhesions. *Biophys. J.* **2011**, *100*, 2883–2893. [[CrossRef](#)]
60. Zaidel-Bar, R.; Cohen, M.; Addadi, L.; Geiger, B. Hierarchical assembly of cell–matrix adhesion complexes. *Biochem. Soc. Trans.* **2004**, *32*, 416–420. [[CrossRef](#)]
61. Balaban, N.Q.; Schwarz, U.S.; Riveline, D.; Goichberg, P.; Tzur, G.; Sabanay, I.; Mahalu, D.; Safran, S.; Bershadsky, A.; Addadi, L.; et al. Force and focal adhesion assembly: A close relationship studied using elastic micropatterned substrates. *Nat. Cell Biol.* **2001**, *3*, 466–472. [[CrossRef](#)]
62. Soiné, J.R.D.; Brand, C.A.; Stricker, J.; Oakes, P.W.; Gardel, M.L.; Schwarz, U.S. Model-based Traction Force Microscopy Reveals Differential Tension in Cellular Actin Bundles. *PLoS Comput. Biol.* **2015**, *11*, e1004076. [[CrossRef](#)]

63. Alexandrova, A.Y.; Arnold, K.; Schaub, S.; Vasiliev, J.M.; Meister, J.J.; Bershadsky, A.D.; Verkhovsky, A.B. Comparative dynamics of retrograde actin flow and focal adhesions: formation of nascent adhesions triggers transition from fast to slow flow. *PLoS ONE* **2008**, *3*, e3234. [\[CrossRef\]](#)
64. Vicente-Manzanares, M.; Zareno, J.; Whitmore, L.; Choi, C.K.; Horwitz, A.F. Regulation of protrusion, adhesion dynamics, and polarity by myosins IIA and IIB in migrating cells. *J. Cell Biol.* **2007**, *176*, 573–580. [\[CrossRef\]](#) [\[PubMed\]](#)
65. Chan, C.E.; Odde, D.J. Traction Dynamics of Filopodia on Compliant Substrates. *Science* **2008**, *322*, 1687–1691. [\[CrossRef\]](#) [\[PubMed\]](#)
66. Paňková, K.; Rösel, D.; Novotný, M.; Brábek, J. The molecular mechanisms of transition between mesenchymal and amoeboid invasiveness in tumor cells. *Cell. Mol. Life Sci.* **2010**, *67*, 63–71. [\[CrossRef\]](#) [\[PubMed\]](#)
67. Friedl, P.; Noble, P.; Shields, E.; Zanker, K. Locomotor phenotypes of unstimulated CD45RA^{high} and CD45RO^{high} CD4⁺ and CD8⁺ lymphocytes in three-dimensional collagen lattices. *Immunology* **1994**, *82*, 617.
68. Gorelik, R.; Gautreau, A. Quantitative and unbiased analysis of directional persistence in cell migration. *Nat. Protoc.* **2014**, *9*, 1931. [\[CrossRef\]](#)
69. Petrie, R.J.; Doyle, A.D.; Yamada, K.M. Random versus directionally persistent cell migration. *Nat. Rev. Mol. Cell Biol.* **2009**, *10*, 538–549. [\[CrossRef\]](#)
70. Kubow, K.E.; Shuklis, V.D.; Sales, D.J.; Horwitz, A.R. Contact guidance persists under myosin inhibition due to the local alignment of adhesions and individual protrusions. *Sci. Rep.* **2017**, *7*, 14380. [\[CrossRef\]](#)
71. Shellard, A.; Szabó, A.; Trepát, X.; Mayor, R. Supracellular contraction at the rear of neural crest cell groups drives collective chemotaxis. *Science* **2018**, *362*, 339–343. [\[CrossRef\]](#)
72. Fletcher, A.; Osterfield, M.; Baker, R.; Shvartsman, S. Vertex Models of Epithelial Morphogenesis. *Biophys. J.* **2014**, *106*, 2291–2304. [\[CrossRef\]](#)
73. Mori, Y.; Jilkine, A.; Edelstein-Keshet, L. Wave-pinning and cell polarity from a bistable reaction-diffusion system. *Biophys. J.* **2008**, *94*, 3684–3697. [\[CrossRef\]](#)
74. Roycroft, A.; Mayor, R. Molecular basis of contact inhibition of locomotion. *Cell. Mol. Life Sci.* **2016**, *73*, 1119–1130. [\[CrossRef\]](#) [\[PubMed\]](#)
75. Svitkina, T.M.; Surguchova, I.G.; Verkhovsky, A.B.; Gelfand, V.I.; Moeremans, M.; De Mey, J. Direct visualization of bipolar myosin filaments in stress fibers of cultured fibroblasts. *Cell Motil. Cytoskelet.* **1989**, *12*, 150–156. [\[CrossRef\]](#) [\[PubMed\]](#)
76. Aratyn-Schaus, Y.; Oakes, P.W.; Gardel, M.L. Dynamic and structural signatures of lamellar actomyosin force generation. *Mol. Biol. Cell* **2011**, *22*, 1330–1339. [\[CrossRef\]](#) [\[PubMed\]](#)
77. Verkhovsky, A.B.; Borisy, G.G. Non-sarcomeric mode of myosin II organization in the fibroblast lamellum. *J. Cell Biol.* **1993**, *123*, 637–652. [\[CrossRef\]](#) [\[PubMed\]](#)
78. Finer, J.T.; Simmons, R.M.; Spudich, J.A. Single myosin molecule mechanics: Piconewton forces and nanometre steps. *Nature* **1994**, *368*, 113–119. [\[CrossRef\]](#)
79. Molloy, J.E.; Burns, J.E.; Kendrick-Jones, J.; Tregear, R.T.; White, D.C. Movement and force produced by a single myosin head. *Nature* **1995**, *378*, 209–212. [\[CrossRef\]](#)
80. Gardel, M.L.; Valentine, M.T.; Crocker, J.C.; Bausch, A.R.; Weitz, D.A. Microrheology of Entangled F-Actin Solutions. *Phys. Rev. Lett.* **2003**, *91*, 158302. [\[CrossRef\]](#)
81. Kalwarczyk, T.; Ziębacz, N.; Bielejewska, A.; Zaboklicka, E.; Koynov, K.; Szymański, J.; Wilk, A.; Patkowski, A.; Gapiński, J.; Butt, H.J.; et al. Comparative analysis of viscosity of complex liquids and cytoplasm of mammalian cells at the nanoscale. *Nano Lett.* **2011**, *11*, 2157–2163. [\[CrossRef\]](#)
82. Mastro, A.M.; Babich, M.A.; Taylor, W.D.; Keith, A.D. Diffusion of a small molecule in the cytoplasm of mammalian cells. *Proc. Natl. Acad. Sci. USA* **1984**, *81*, 3414–3418. [\[CrossRef\]](#)
83. Arcizet, D.; Meier, B.; Sackmann, E.; Rädler, J.O.; Heinrich, D. Temporal Analysis of Active and Passive Transport in Living Cells. *Phys. Rev. Lett.* **2008**, *101*, 248103. [\[CrossRef\]](#)
84. Lammerding, J. Mechanics of the Nucleus. In *Comprehensive Physiology*; American Cancer Society: Atlanta, GA, USA, 2011; pp. 783–807.
85. Burridge, K.; Chrzanowska-Wodnicka, M. Focal adhesions, contractility, and signaling. *Annu. Rev. Cell Dev. Biol.* **1996**, *12*, 463–519. [\[CrossRef\]](#)
86. Geiger, B.; Spatz, J.P.; Bershadsky, A.D. Environmental sensing through focal adhesions. *Nat. Rev. Mol. Cell Biol.* **2009**, *10*, 21. [\[CrossRef\]](#)

87. Erdmann, T.; Schwarz, U.S. Stability of Adhesion Clusters under Constant Force. *Phys. Rev. Lett.* **2004**, *92*, 108102. [[CrossRef](#)] [[PubMed](#)]
88. Li, F.; Redick, S.D.; Erickson, H.P.; Moy, V.T. Force measurements of the $\alpha 5 \beta 1$ integrin–fibronectin interaction. *Biophys. J.* **2003**, *84*, 1252–1262. [[CrossRef](#)]
89. Kassianidou, E.; Kumar, S. A biomechanical perspective on stress fiber structure and function. *Biochim. Biophys. Acta BBA Mol. Cell Res.* **2015**, *1853*, 3065–3074. [[CrossRef](#)] [[PubMed](#)]
90. Chen, W.T. Mechanism of retraction of the trailing edge during fibroblast movement. *J. Cell Biol.* **1981**, *90*, 187–200. [[CrossRef](#)] [[PubMed](#)]
91. Hotulainen, P.; Lappalainen, P. Stress fibers are generated by two distinct actin assembly mechanisms in motile cells. *J. Cell Biol.* **2006**, *173*, 383–394. [[CrossRef](#)]
92. Kuragano, M.; Uyeda, T.Q.; Kamijo, K.; Murakami, Y.; Takahashi, M. Different contributions of nonmuscle myosin IIA and IIB to the organization of stress fiber subtypes in fibroblasts. *Mol. Biol. Cell* **2018**, *29*, 911–922. [[CrossRef](#)]
93. Lewis, P.A.; Shedler, G.S. Simulation of nonhomogeneous Poisson processes by thinning. *Nav. Res. Logist.* **1979**, *26*, 403–413. [[CrossRef](#)]
94. Bouchard-Côté, A.; Vollmer, S.J.; Doucet, A. The bouncy particle sampler: A non-reversible rejection-free Markov chain Monte Carlo method. *arXiv* **2015**, arXiv:1510.02451.
95. Vose, M.D. A linear algorithm for generating random numbers with a given distribution. *IEEE Trans. Softw. Eng.* **1991**, *17*, 972–975. [[CrossRef](#)]



© 2020 by the author. Licensee MDPI, Basel, Switzerland. This article is an open access article distributed under the terms and conditions of the Creative Commons Attribution (CC BY) license (<http://creativecommons.org/licenses/by/4.0/>).